UNIVERSITY OF LONDON THESIS

Degree	Year	Name of Author
PhD	2005	GOONASEKERA , MALIKA

Symmetry Breaking and Directed Transport of Cold Atoms in Optical Lattices

Malika Goonasekera

A thesis submitted in partial fulfilment of
the requirements for the degree of
Doctor of Philosophy at the University of London

University College London

University of London

November 2004

UMI Number: U591720

UMI U591720

"Science is a wonderful thing if one does not have to earn one's living at it."

Albert Einstein

ABSTRACT

Symmetry Breaking and Directed Transport of Cold Atoms in Optical Lattices

Malika Goonasekera, University College London

Ph.D. Thesis, November 2004

The central theme of this thesis is the directed transport of cold atoms in optical lattices. Several methods for producing such an outcome are proposed, experimentally realised and characterised, in both dissipative and non-dissipative regimes. Accordingly, this thesis may be thought to be composed of two parts.

The first section reports results of directed transport in non-dissipative optical lattices, where we used the atom optics realisation of the delta-kicked rotor (DKR) as a model system. Initial experiments performed on this system showed evidence of dynamical localisation, the signature of quantum chaos, and we exploited the presence of the momentum boundary (a barrier to diffusion arising from the approximation of delta-kicks with finite width impulses) to produce asymmetric momentum diffusion.

Breaking the DKR system symmetries produced directed diffusion due to chaotic dynamics alone. We observed directed transport in a spatially symmetric system whenever temporal symmetry was broken, and also when the spatial and temporal symmetry of the DKR were simultaneously broken.

We also report the first experimental evidence for a 'double-DKR', where experiments performed using a kick sequence composed of closely spaced pairs of kicks instead of single kicks caused significant alterations in the observed behaviour of the kicked rotor system. The origin of this new behaviour was explained in the framework of kick-to-kick correlations and our results were

found to be in excellent agreement with numerical simulations.

The second part of this thesis describes the realisation of a Brownian ratchet in a 3D dissipative lattice, where fluctuations between different potential surfaces acted as the source of noise. These fluctuations were rectified by the application of a periodic, bi-harmonic driving force, which broke the temporal symmetry of the system. Both current reversal and stochastic resonance behaviour characteristic of a Brownian ratchet were observed.

ACKNOWLEDGEMENTS

First and foremost, my deepest thanks go to our group's post-doc, Dr Philip Jones, for his forbearance, perseverance and sarcasm. Without Phil, there would be no thesis.

Profuse thanks also to my two supervisors: to Dr David Meacher, for taking me on as a member of the Laser Cooling group, and to Dr Ferruccio Renzoni, who stepped into the breach after his predecessor ran away (I didn't think I was that bad a student).

A big 'Thank you' also to the original members of the UCL Laser Cooling Group, Silvia Bergamini and Stephan Winklbauer (especially for the fried chicken) but most especially to Harry 'Basil' Saunders-Singer for making the lab a very colourful and flowery place. Some labs have mice, others have cats, we had the Lizard.

Honourable mentions to Matt Isherwood, Nic Hutchings and the UCL Theory group for their pictures, to Ted and Rafid for making all things electrical work properly, and to UCL and EPSRC for their financial support.

CONTENTS

LIST OF FIGURES

Introduction

The manipulation of atoms with laser light is a highly active research area currently, with its significance recognised by Nobel prizes in 1997 and 2001 for the techniques of laser cooling and Bose-Einstein condensation respectively. Of particular relevance to this thesis are cold atoms in optical lattices. These ordered samples of atoms in periodic potentials created by light form a versatile experimental test-ground for many phenomena, ranging from Bragg scattering studies in (defect-free) optical lattices similar to the investigations of crystalline structures in solid state physics to Mott-insulator transitions in Bose-Einstein condensates similar to those occurring in superconducting materials in condensed matter physics. Directed transport studies in particular are useful in modelling molecular motors and, as electronics continue to shrink in size, may have future applications in studies of electron transport in nanoscale circuitry.

The subject of this thesis is the directed motion of laser-cooled caesium (Cs) atoms in optical lattices, a regular array of potential wells formed by the interference pattern of several laser beams. This presents a highly tunable environment for experiments since most parameters can be easily adjusted by changing the properties of the laser fields involved. For instance, the amount of noise in the system can be varied by changing the detuning from resonance of the laser beams comprising the lattice. In all cases, preferential motion of

the atoms is derived in the absence of any external bias by simply breaking the spatial and temporal symmetries of the system.

This thesis can be roughly divided into two sections according to the amount of noise present in the system. In the first part, the laser beams are detuned far from resonance such that the momentum diffusion of atoms may be studied in a system with a very low decoherence rate and where the forces involved are deterministic. It is now possible to realise a delta-kicked rotor, the paradigm model for studying quantum chaotic behaviour. Secondly, the lasers are brought much closer to resonance to increase the photon scattering rate and directed motion is generated in a dissipative regime where a Brownian motor may be actualised.

The structure of this thesis is as follows. Chapter 2 introduces the laser cooling techniques used in preparing cold Cs atoms and the methods used for data collection and analysis. A brief introduction to quantum chaos, the delta-kicked rotor (DKR) and some experimental results confirming the presence of quantum chaotic behaviour are given in Chapter 3. The approximation of delta-kicks by pulses of finite temporal width causes a modulation of the diffusion constant describing atomic energy growth. Chapter 4 demonstrates how this can be used to produce asymmetric momentum diffusion when used in conjunction with our moving lattice technique to vary the initial atomic momentum. This chapter also includes an investigation of directed transport in a mixed phase space, where asymmetric momentum diffusion can be achieved by engineering stable structures in the DKR phase space.

Chapter 5 reports the results of two ways in which directed diffusion may be generated in a non-dissipative system. Firstly, the optical potential is pulsed according to a two-period kick sequence to break the temporal symmetry of the system. This introduces a cosinusoidal momentum dependence into the diffusion constant that can be exploited to produce asymmetric diffusion. The addition of a linear potential gradient that alternates sign with successive kicks to this system breaks the spatial symmetry of the lattice and provides a second mechanism for directed transport. In Chapter 6, asymmetric momentum diffusion is

made possible by non-negligible kick-to-kick correlation terms in the diffusion constant that arise when a sequence of closely spaced kick pairs is used to pulse the optical lattice.

Chapter 7 contains the results of an experimental realisation of a Brownian ratchet, where directed diffusion results from the rectification of noise in the optical lattice. This system is unusual because the source of fluctuations in the system is optical pumping between potential surfaces of the different ground state sub-levels. Finally, Chapter 8 concludes this thesis with a brief summary of the salient results and a discussion of experiments planned for the future.

Cold atom preparation

This section presents an introduction to magneto-optical trapping, the techniques used to trap and cool atoms that underlie all the experiments described in this thesis and describes the experimental setup at UCL. As ways of cooling atoms were historically developed before they were trapped, discussion begins with laser cooling, methods designed to produce a narrow velocity distribution centred near zero velocity and increase atomic phase space density, before outlining trapping schemes.

Once the atoms are trapped and cooled, they are localised in an optical lattice created by the interference pattern between several laser beams. The lattices involved differ in type depending on the nature of the experiment. Experiments investigating quantum chaos and transport in non-dissipative regimes use a simple far-detuned, 1D lattice formed by overlapping two beams whilst the realisation of a Brownian ratchet requires a near-resonant, 3D optical potential (covered in greater detail in Chapter 7).

The final section in this Chapter describes the how the preceding theory is realised experimentally using our magneto-optical trap. As all experiments described herein are conducted using caesium (Cs) atoms, all numerical values refer to Cs unless otherwise stated.

2.1 Laser cooling and trapping

Laser cooling and trapping techniques has opened up new avenues in physics research by allowing unprecedented control over atoms and atomic motion. Atom trapping experiments regularly cool up to 10^9 atoms down to micro-Kelvin temperatures, thus enabling precision measurements of the spectroscopic properties such as atomic transition frequencies and lifetimes for use in atomic clocks. Magneto-optical traps are also used to cool atoms to low enough temperatures where it is possible to form optically bound lattices. Magneto-optical trapping is also the first stage *en route* to a Bose-Einstein condensate after which evaporative cooling is used to increase the phase space density of the trapped atoms to reach the quantum degenerate regime.

The importance of these developments has been recognised by Nobel Prizes awarded to proponents of this field from Claude Cohen-Tannoudji, William Phillips and Steven Chu for the development of cooling and trapping techniques in 1997 and the 2001 Nobel to Wolfgang Ketterle, Carl Wieman and Eric Cornell for the achievement and early experiments on a Bose-Einstein condensate [1].

2.1.1 Doppler Cooling and optical molasses

Letokhov (as cited in [2]) first suggested the use of radiation pressure to trap atoms in 1968. This was later followed by proposals for trapping ions from Wineland and Dehmelt [3] and for cooling neutral atoms from Hänsch and Schawlow [4] in 1975. The basic mechanism in laser cooling is the conservation of energy and momentum in a cycle of photon absorption and emission.

Consider the simple example of a two-level atom moving in a light field created by two counter-propagating laser beams tuned slightly below atomic resonance (i.e. red detuned). A beam propagating in the opposite direction to the atom is Doppler-shifted closer to resonance, whilst the beam propagating in the same direction as the atom is red-shifted further away from resonance. Absorbing a photon causes an atom to recoil in the direction of incident light but the Doppler shift causes a difference in the number of photons scattered
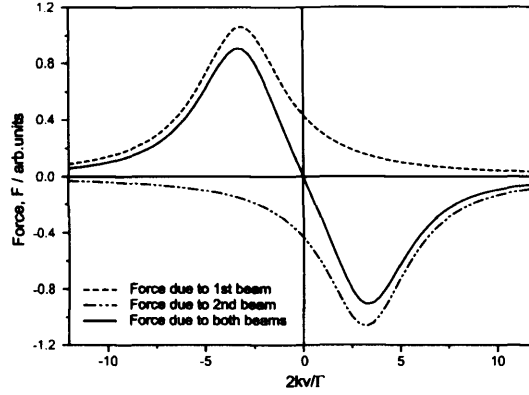
Figure 2.1: The force as a function of atomic velocity for an atom illuminated by two counter-propagating beams. The horizontal axis shows the dimensionless parameter $2kv/\Gamma$, where $k = 2\pi/\lambda$ is the laser wavevector and Γ is the natural linewidth. The force due to a single beam is shown by the dotted lines, whilst the solid line gives the total force of the two beams combined.

from each beam, resulting in a net velocity-dependent force that opposes the motion of the atom. Due to the involvement of the Doppler shift in this process, it is known as *Doppler cooling*.

An analytical form for the force is difficult to find but it can be shown that each laser beam exerts a force with a Lorentzian velocity dependence [5], the form of which is sketched in figure 2.1. At low intensities and for small velocities $|v|$, the total force on the atom (solid line) can be found by summing the contributions from each beam (dotted lines). For laser excitation with light of frequency ω_L that is tuned below the atomic transition frequency ω_A by an amount $\Delta = \omega_L - \omega_A$ (called the detuning), the total force F is:

$$F = -\beta v \tag{2.1}$$

where β is the damping coefficient.

The velocity dependence in equation 2.1 is important because it allows for compression of the atomic velocity distribution. Atomic velocities are damped towards $v = 0$ provided that they initially fall inside the velocity capture range, corresponding to the linear region of figure 2.1.

This situation can easily be extended to three dimensions by using six laser beams to form three orthogonal standing waves such that the atom is illuminated from all directions and will everywhere see a viscous damping force opposing its motion. As similar equations govern the motion of a particle in viscous medium, the cooled atoms are referred to as an *optical molasses*.

At low intensities the excited atoms decay via spontaneous emission, which is a stochastic process. Because the direction of the emitted photon is uncorrelated with the direction of absorption, spontaneous emission causes no net change in the atomic momentum when averaged over a large number of absorption-emission cycles.

The change in the atomic momentum caused by the recoil due to a single spontaneous emission event is analogous to a step in a random walk characterised by a diffusion constant D. This can be used to quantify the final kinetic energy of the atoms (similar to the analysis of Brownian motion) using $k_B T = \frac{D}{\beta}$.

A more detailed, three-dimensional analysis taking into account the fluctuating number of photons absorbed (as cited in [6]) yields the Doppler temperature, T_D, defined as the Doppler cooling limit that occurs when the mean atomic kinetic energy is equal to the energy width of the cooling transition:

$$k_B T_D = \frac{\hbar \gamma}{2} \tag{2.2}$$

where γ is the natural linewidth of the excited state. The radiative lifetime of this state $\frac{1}{\gamma} = 30$ ns for the $6P_{\frac{3}{2}}$ state of Cs. This corresponds to a Doppler temperature of $T_D = 125$ μK and a 1D velocity of $v_D = \sqrt{\frac{k_B T_D}{M_a}} \approx 9$ cms^{-1}.

2.1.2 Sub-Doppler cooling

The first experiments on an optical molasses of sodium atoms, conducted by Lett *et al*, reported surprisingly low temperatures of 40 μK [7], far below the predicted Doppler temperature of 240 μK. To explain their results it was necessary to drop the simplified model of a two-level atom and consider the field polarisation and the effects of optical pumping between hyperfine states [8, 9, 10].

In the one-dimensional case of two counter-propagating beams with orthogonal, linear polarisations, called the lin⊥lin configuration, the polarisation of the resultant standing wave varies rapidly over the one wavelength. It changes from being linear to circularly polarised after an eighth of a wavelength, to orthogonal linear at $\frac{\lambda}{4}$ through to opposite circular polarisation over half an optical wavelength, as drawn in figure 2.3.

The lin⊥lin scheme is most simply explained using a fictitious atom with a $J_g = 1/2 \rightarrow J_e = 3/2$ transition, for which the squared Clebsch-Gordan (C_{ge}^2) coefficients and necessary polarisations are shown in figure 2.2. The magnitude of the a.c. Stark shift or *light* shift depends on the C_{ge}^2 coefficients, which in turn depend on the magnetic quantum number and polarisation of the light field, so the light shift is different for different magnetic sub-levels.

By comparing the C_{ge}^2 coefficients, we can see that for pure σ^+ light the $M_g = +\frac{1}{2}$ sub-level experiences a shift that is three times larger than that of the $M_g = -\frac{1}{2}$ state and vice versa at sites of σ^- polarisation. Polarisation gradients therefore lead to a periodic spatial modulation of the light shift of the energy levels [11]:

$$U_\pm(z) = \frac{U_0}{2}[-2 \pm cos(2k_L z)] \qquad (2.3)$$

for the ground (plus) and excited (minus) states where k_L is the laser wavevector and where

$$U_0 = -\frac{\hbar\Delta}{3}\frac{\Omega^2}{\Delta^2 + \Gamma^2/4} \qquad (2.4)$$

where Γ is the natural linewidth of the transition and $\Omega = \frac{-eE_0}{\hbar}\langle e|r|g\rangle$ is the definition of the on-resonance Rabi frequency for a transition with Clebsch-Gordan coefficient $C_{ge} \approx 1$ for an atom at position coordinate r.

The cooling mechanism relies on optically pumping an atom nearing the top of one potential hill into the lower lying state, figure 2.4. Each optical pumping event emits a photon of higher energy than that absorbed, thereby dissipating energy into the radiation field.
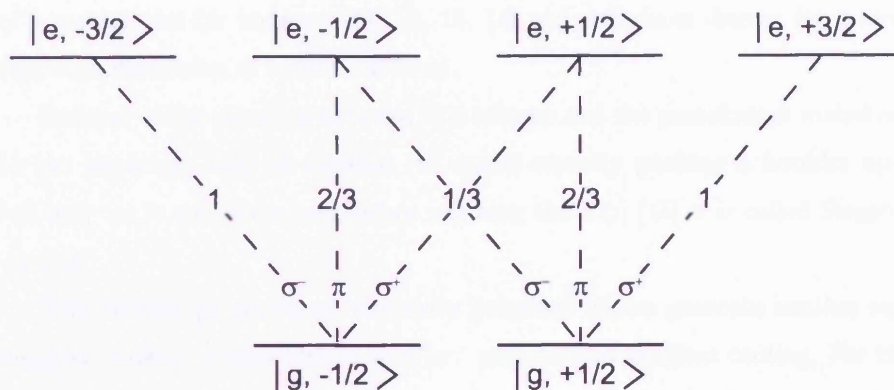
Figure 2.2: The C_{ge}^2 coefficients and required polarisations for a $J_g = 1/2 \rightarrow J_e = 3/2$ transition.
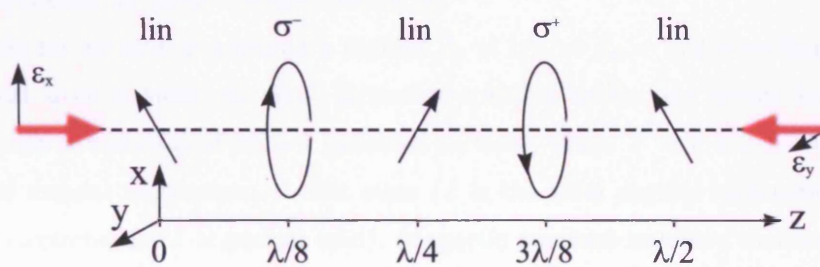
Figure 2.3: The variation in the polarisation of the standing wave formed by two counter-propagating laser beams with orthogonal, linear polarisations ϵ_x and ϵ_y in the lin $\perp$ lin configuration.

This process continues until the atom no longer has enough kinetic energy to climb another hill. The atoms become localised in the potential wells and form an optical lattice with long range order and a regular structure reminiscent of a crystal (see for instance [11, 12, 13, 14] and references therein for a more thorough discussion of optical lattices).

Because of the parallels between this scheme and the punishment meted out to the legendary king of Corinth (to spend eternity pushing a boulder up a hill only for it roll down just before reaching the top) [15] it is called *Sisyphus cooling*.

Two counter-propagating, circularly polarised beams generate another sub-Doppler cooling process known as $\sigma^+\sigma^-$ polarisation gradient cooling. For this configuration, the amplitude of the polarisation remains uniform everywhere but the direction of the polarisation vector changes by 2π over one wavelength and is discussed in [8].

Sisyphus cooling has maximum efficiency when the atomic velocity is such that an atom moves one quarter of a wavelength between optical pumping events. It can be shown that the friction coefficient in this case is larger than that of Doppler cooling by a factor of $2\frac{|\Delta|}{\Gamma}$ but the momentum diffusion constant is of the same order so the final temperature is lower than the Doppler temperature by about the same factor [5].

So far we have considered a fictious $J_g = 1/2 \rightarrow J_e = 3/2$ transition but a real atom is more complex. Hyperfine splitting means any energy level is actually a manifold of $2F + 1$ potential surfaces, where $F = I + J$ labels the total angular momentum of that state (J is the total angular momentum of the electrons and I is nuclear spin). Magnetic quantum numbers therefore do not adequately describe the system because the eigenstates of the light shift operator are no longer pure Zeeman states but rather different superpositions of the magnetic sub-levels, except at sites of pure circular polarisation. The description of Sisyphus cooling outlined above, however, remains applicable in the case of a $F \rightarrow F' = F + 1$ transition, as in our cooling scheme [11].

The Sisyphus cooling phase can be considered to be at an end once the atoms
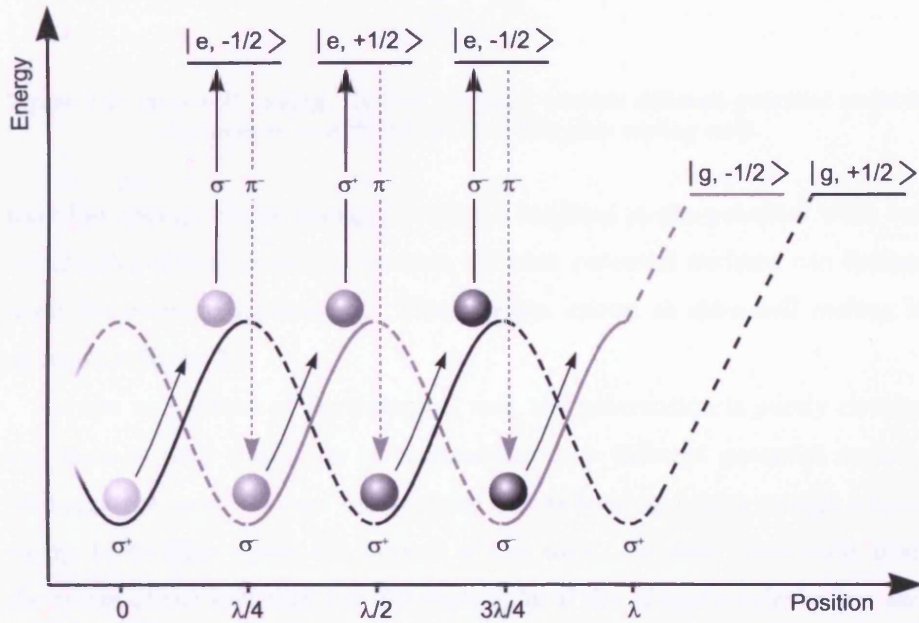
Figure 2.4: Schematic representation of Sisyphus cooling for a $J_g = \frac{1}{2} \rightarrow J_e = \frac{3}{2}$ transition. An atom climbing up a potential hill is preferentially pumped into the lower lying magnetic ground state. As the photon absorbed has a lower frequency than the emitted photon some of the atomic energy is lost with each optical pumping event and this process continues until the atoms do not have enough kinetic energy to climb any more hills and become localised in the potential wells.
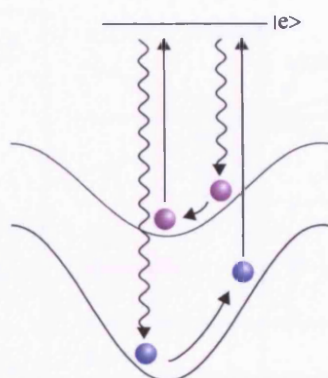
Figure 2.5: Intra-well cooling. Optical pumping between different potential surfaces continues to cool the atoms once Sisyphus cooling ends.

have lost enough kinetic energy to become localised in the potential wells but (stochastic) optical pumping between different potential surfaces can further lower the atomic temperatures. This process, known as *intra-well cooling*, is pictured in figure 2.5.

At the very centre of the potential well, the polarisation is purely circular and there is little possibility of a transition to a different potential surface. Although the atoms cannot escape from the wells, they retain enough kinetic energy to oscillate about the bottom of the wells. As they move away from the centre of the well they can see some light of the opposite polarisation and experience a non-zero probability of a transition into a different sub-level. The atoms lose energy when they are pumped into a lower lying potential surface, which further reduces the temperature of the ensemble.

2.1.3 Magneto-optical trapping

Optical molasses itself is not a trap. As the optical Earnshaw theorem implies, a scattering force proportional to light intensity will have zero divergence and form an unstable trap as the atoms are free to diffuse until they reach the surface of the interaction region and escape. Trapping and cooling ions had been experimentally achieved by 1985 [16] but trapping neutral atoms proved a more difficult task until Jean Dalibard suggested adding an external magnetic
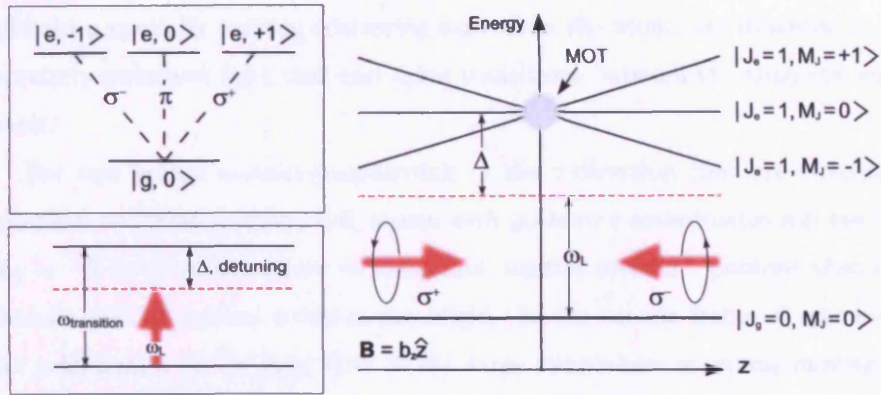
Figure 2.6: A 2D representation of the principles behind a MOT, showing the Zeeman splitting of the energy levels for a $J_g = 0 \rightarrow J_e = 1$ transition. The excited level J_e is split into three sublevels, with transitions to each state driven by different polarisations (top left box). If illuminated by two counter-propagating beams tuned below the resonance frequency (bottom left box) and of the appropriate polarisation, the atoms experience a position-dependent restoring force and are pushed towards the origin $z = 0$ (right box).

field to alter the linear dependence of force on intensity such that the optical Earnshaw theorem no longer applied. The first magneto-optical trap based on this principle was successfully demonstrated by Raab *et al* in 1987 [17]. A stable trap is produced by using a weak external magnetic field gradient to introduce a position-dependent force on the atoms. The interaction between the atom and the magnetic field, called the Zeeman effect, causes a small, position-dependent shift in the atomic energy levels. The magnitude of the splitting is proportional to the magnetic field strength,B:

$$\Delta E = M_J g_J \mu_B B \tag{2.5}$$

where μ_B is the magnetic dipole moment of the atom, g_J is the Landè g-factor and M_J is the magnetic quantum number.

Figure 2.6 depicts the Zeeman splitting for a two-level atom with a fictional $J_g = 0 \rightarrow J_e = 1$ transition. A weak magnetic field $\mathbf{B} = b_Z \hat{z}$ with a linear field gradient splits the first excited state of the atom into three sub-levels, $M_J = 0, \pm 1$. The spatially varying shift in the energy of the excited state

leads to a spatially varying scattering rate when the atoms are illuminated by circularly polarised light that can drive transitions between the magnetic sub-levels.

For two beams counter-propagating in the z-direction that are circularly polarised as shown in figure 2.6, atoms with positive z co-ordinates will see the $M_J = -1$ level shifted closer to resonance, scatter more σ^- photons than σ^+ photons and be pushed towards the origin. In the atomic frame of reference, the polarisation of the light field is the same everywhere so atoms moving in the negative z direction will also be pushed towards $z = 0$. Thus in addition to the viscous damping force on their velocity, the atoms also experience a position-dependent restoring force, $F \approx kz$ for small z. The only requirement for confinement is that the atomic velocity is sufficiently low for the atomic magnetic moment to adiabatically follow changes in the field direction, which generally holds for laser cooled atoms.

Both types of Sisyphus cooling mechanisms mentioned in the previous section are present in a real 3D molasses due to its complex polarisation topography [18], so sub-Doppler temperatures are possible to attain in MOTs. That the final temperature in a MOT is proportional to the light shift and below the Doppler limit has been shown many time in literature, for example [19, 20, 21].

The cooling transition in caesium is $6^2S_{1/2}(F = 4) \rightarrow 6^2P_{3/2}(F = 5)$ D2 line but occasional off-resonant optical pumping into the $6^2S_{1/2}(F = 3)$ ground state is possible because the hyperfine splitting between the $F_e = 4$ and $F_e = 5$ hyperfine states is small. This ends the cooling cycle as this sub-level is too far from resonance for further excitation. Hence a second *repumper* laser is required to introduce a small amount of light resonant with the $6^2S_{1/2}(F = 3) \rightarrow 6^2P_{3/2}(F = 4)$ transition to close the cooling cycle. A schematic of the energy levels structure of Cs (showing the magnitude of the hyperfine splitting) is given in figure 2.7.

The very first experimental MOTs were loaded from chirp-cooled atomic beams but Carl Wieman's group showed it was possible to load a MOT from just background vapour [22]. This experimentally easier method is the one we
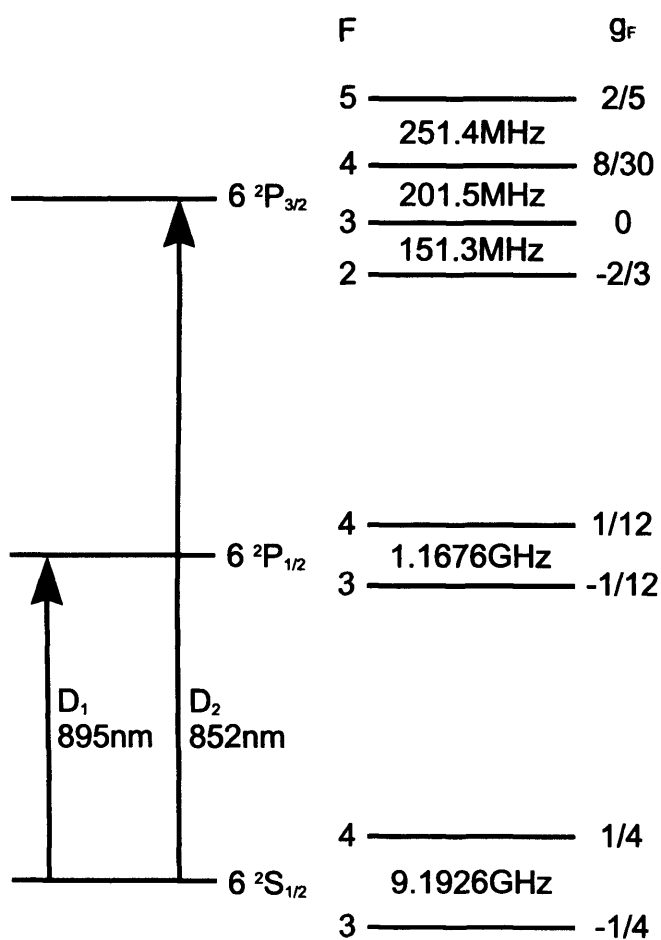
Figure 2.7: The hyperfine energy level structure of caesium. The cooling transition is the $6^2S_{1/2}(F = 4) \rightarrow 6^2P_{3/2}(F = 5)$ D2 line and the repumper is $6^2S_{1/2}(F = 3) \rightarrow 6^2P_{3/2}(F = 4)$.

adopt, using a standard six beam MOT with a vacuum cell filled with dilute Cs vapour. The cell is surrounded by anti-Helmholtz coils and three circularly-polarised standing waves, one in each orthogonal direction, that intersect in the region of zero magnetic field.

The trap density is limited by fluorescence from some atoms being absorbed by others and also by collisions but there are various methods of increasing trap density should it be necessary, including 'dark MOTs' [23]. Several other configurations for MOTs are also possible, for example mirror-MOTs that trap atoms near the surface of a current carrying conductor [24] and pyramid MOTs [25].

In addition, there are two other basic types of trap: optical dipole traps and magnetic traps. Optical dipole traps use the force exerted on the induced electric dipole of an atom when it is in a radiation field whereas magnetic traps utilise the splitting of energy levels in the presence of a magnetic field but neither of these traps cool. A detailed discussion of such traps can be found in [5, 2].

The MOT, however, remains by far the most popular choice for the experimentalist for reasons of practicality, ease and low cost of assembly and robustness. We use a MOT because it combines cooling and trapping; it is possible to switch from one process to the other by simply changing the detuning of the laser fields and switching off the magnetic coils. A MOT can tolerate some intensity mismatch and beam misalignment, as well as not requiring pure polarisations to operate.

2.2 A note on recoil units

Recoil units provide a useful way of quantifying the dynamics of cold atoms in optical lattices. The recoil energy, $E_r = \frac{\hbar^2 k^2}{2M_a}$ is defined as the kinetic energy an atom gains by absorbing a photon and the corresponding recoil frequency, $\omega_r = \frac{E_r}{\hbar} = 2\pi \times 2.1$ kHz for caesium (Cs).

The absorption of a single photon causes the atom to recoil in the direction of incident light and change its velocity by an amount called the recoil velocity

$v_r = \frac{\hbar k}{M_a}$, where M_a is the mass of the atom, k is the laser wavevector, $\hbar = \frac{h}{2\pi} = 1.054 \times 10^{-34}$ Js rad^{-1} and h is Planck's constant.

2.3 Experimental Setup

The setup of the quantum chaos experiments differs significantly from that of the Brownian ratchet experiments but there are large parts of the apparatus that remain unchanged and do not need to be reviewed twice. This section will therefore provide an account of the experimental set-up designed to achieve a MOT, which is common to both, and leave more detailed discussion of the experimental method to the relevant sections.

MOT configuration

A schematic of our experimental setup is presented in figure 2.8. The MOT beams are derived from a single 'trap' laser that is seeded by a 100 mW grating-stabilised 'master' diode laser. The linewidth of the master laser is narrowed using a reflection grating to feed back the first order into the laser, known as the Littrow configuration, and results in a marked narrowing of the laser linewidth but also a considerable loss of output power which is why a master-slave setup is used. The 150 mW slave diode lasers take on the spectral characteristics of the master laser by preferentially amplifying the frequency mode seeded by the master laser with no significant loss of output power.

The output of the trap laser is passed thorough an acousto-optic modulator (AOM) that shifts the frequency of the beam down by 80 MHz. The zero order from the trap AOM is passed through yet another 80 MHz AOM and the emerging -1 order used as the imaging beams. The -1 order of the trap AOM is split into three beams of approximately equal intensity using a combination of beam-splitting cubes and halfwave-plates for use as the trap beams.

They are manipulated such that they are incident on a vacuum chamber in all three orthogonal directions and retro-reflected to form the three standing waves required for trapping and cooling. Quarterwave-plates in front of the
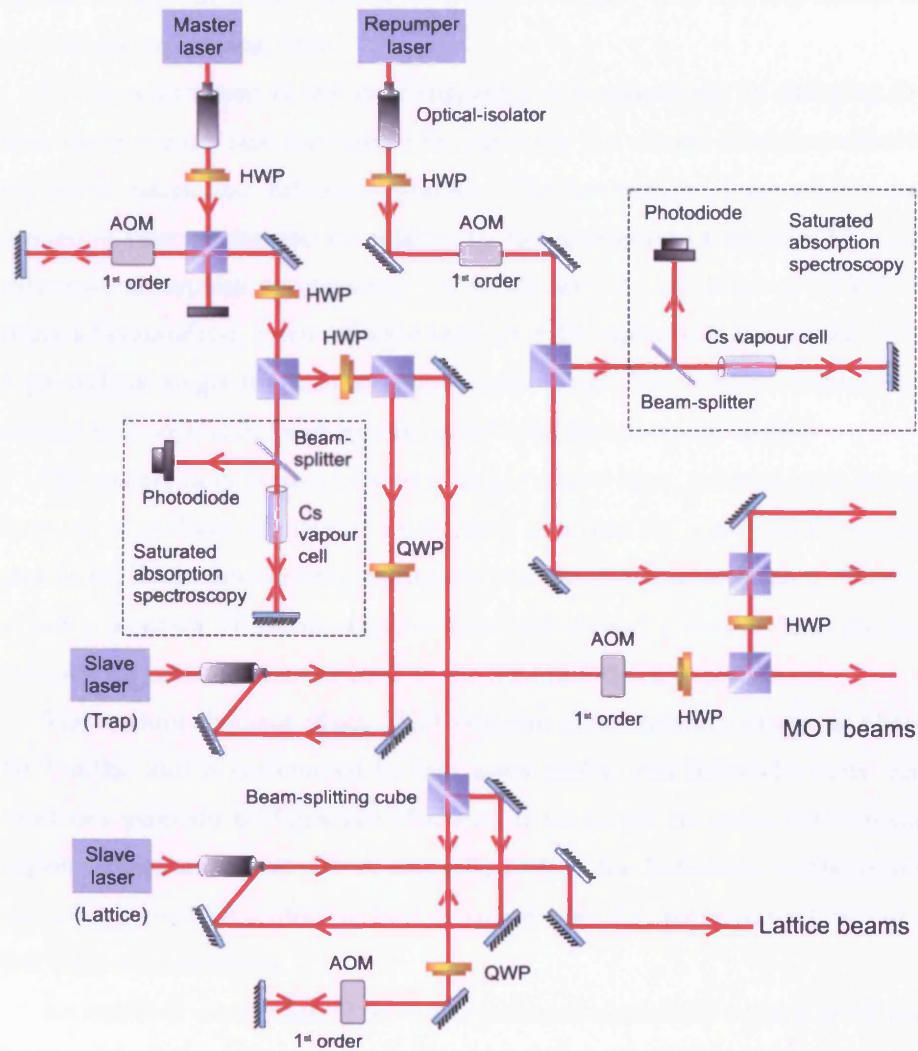
Figure 2.8: A schematic of experimental apparatus required for the magneto-optical trap.

vacuum chamber ensure that the polarisations are as described in section 2.1.3 and correct for trapping.

A few mW of another 100 mW, grating-stabilised 'repumper' diode laser is passed through an AOM and the -1 order overlapped with the trap beams to provide the repumping light.

Coarse adjustment of the laser frequency is accomplished by changing the laser diode current and fine tuning by adjusting the voltage to a piezo-electric crystal to rotate the diffraction grating. The frequencies of the master and repumper laser beams are set relative to the appropriate transition by using saturated absorption spectroscopy. A small part of each beam is picked off using a beamsplitter, retro-reflected through a Cs vapour cell and passed on to a photodiode to get the saturated absorption signal. The principle behind this scheme is described in much greater detail (but for rubidium) in [26].

The master laser is used to seed a second 'slave' laser, referred to as lattice laser, that produces the lattice beams used to create the near-resonant lattice used in the Brownian ratchet experiments (discussed in greater detail in Chapter 7) and a separate Titanium:Sapphire laser (not shown) is used to form the far-detuned 1D optical potential used in the quantum chaos experiments.

The vacuum chamber of our MOT contains dilute caesium vapour at about 10^{-9} mBar and is surrounded by two water-cooled anti-Helmholtz coils that produce a magnetic field gradient of around 10 Gauss per cm across the trapping region. Three additional sets of magnetic coils in the Helmholtz configuration are used to produce a uniform field to compensate for the terrestrial field of a few hundred milliGauss.

An excellent description of the construction of a standard 6-beam MOT can be found in [27], whilst specific details about how the MOT used at UCL was built may be found in [28].

Experimental cycle

The atoms are first trapped and cooled in the MOT for around 2 seconds before the anti-Helmholtz coils are switched off and they are cooled in an optical

molasses for a further 25-30ms. The temperature of the atoms at this point
is about 6μK. The next stage depends on the nature of the experiment: the
atoms are loaded into a far-detuned 1D optical lattice for quantum chaos ex-
periments or into a 3D near-resonant lattice for directed motion experiments in
the dissipative regime.

The lattice beams are then switched off and atoms are allowed to ballistically
expand for 10-20 ms before being exposed to near resonant light and imaging
the fluorescence on a cooled CCD camera. The images are recorded in 8-bit
tiff format using a WinView program that averages five frames (therefore five
experimental cycles) per photo and are analysed using Matlab. The momentum
distribution can be directly inferred from the spatial distribution of the scattered
light. A Matlab program calculates the background-corrected first and second
moments of the atomic momentum distribution:

$$\langle \rho \rangle = \frac{\int \rho N(\rho) d\rho}{\int N(\rho) d\rho} \tag{2.6}$$

$$\langle \rho^2 \rangle = \frac{\int \rho^2 N(\rho) d\rho}{\int N(\rho) d\rho} \tag{2.7}$$

In the case of our chaos experiments, equation 2.6 is directly equivalent to
the mean momentum and $\frac{1}{2}\langle \rho^2 \rangle$ to the mean energy of the atomic distribution.
In the Brownian ratchet experiments, equation 2.6 may be used to calculate the
centre of mass velocity. These assumptions remain valid so long as the initial
distribution remains narrow $N(x,0) \ll N(x,t)$.

A second program calculates the normalised momentum distributions for
each measurement and in both programs the error in each data point is cal-
culated using the standard deviation of the five frames averaged to give the
intensity distribution $N(\rho)$.

The whole experimental sequence takes around three seconds and is con-
trolled by a LabView program that can be used to alter most experimental
parameters. It governs the timing of the experiment (how long the atoms are
held in the MOT and molasses, for example) and also controls the rf frequency

to the AOMs and the current to anti-Helmholtz coils, as well as switching all the laser beams, the magnetic field gradient and the camera shutter.

2.4 Summary

Laser-cooling caesium atoms is the starting point for all the experiments performed in this thesis. These are well established techniques, discussed many times in literature, so this chapter has presented only a basic introduction to the theoretical concepts involved in preparing cold atoms and how they are implemented experimentally. A detailed description of the construction and early characterisation of the MOT used in all our experiments can be found in [28].

The crucial part of the experiments lie in what is done to the cold atoms after they are cooled and before they are imaged. The various techniques involved in this phase differ significantly between experiments so are dealt with in the relevant sections, beginning with some introductory experiments on quantum chaos in the next chapter and concluding with the realisation of a Brownian ratchet (Chapter 7).

CHAPTER 3

Quantum chaos

This chapter begins with a brief history of chaos and introduces classically chaotic behaviour using the concept of a delta-kicked rotor, a freely rotating rotor that is subjected to a series of instantaneous impulses. This model system is then extended to provide a phenomenological description of quantum chaos. This chapter concludes with experimental results showing dynamical localisation, a quantum interference effect that results in the suppression of diffusive energy growth and characterises the presence of quantum chaos in the delta-kicked rotor.

3.1   Introduction to chaos

The study of dynamical chaos originated from Henri Poincaré's solution to a problem posed at a contest in honour of King Oscar II of Sweden and Norway in the late nineteenth century. The apparent descriptive completeness of Newtonian mechanics had prompted a question regarding the future stability of the universe to which Poincaré submitted the winning response. He showed that this generalisation of the three body problem did indeed have a stable solution.

Published to much acclaim, all copies were later withdrawn when it was pointed out his proof contained a serious error. Poincaré reworked his solution and republished his findings as the prize-winning entry but, contrary to his

previous attempt, now concluded that the stability of the solar system could not be guaranteed.

This prompted further study leading to his most famous conclusion: 'small differences in initial conditions produce very great ones in the final phenomena' [29] and was the beginning of a new branch of mechanics now called classical chaos. In 1917 Einstein published a paper questioning how chaos manifested itself in the quantum regime [29] but interest in quantum mechanics and a lack of available computing power shifted focus away from non-linear dynamics.

Progress stagnated until the mid-twentieth century when Edward Lorenz, a meteorologist, rediscovered chaos in weather patterns when he re-ran a computer simulation with very slightly different starting conditions and found widely diverging outcomes. Mathematicians Steven Smale and Philip Yorke revived interest in studying non-linear oscillators in the 1970s whilst Robert May, a biologist with a background in theoretical physics, discovered period-doubling in animal population growth and decline.

The key concept of universality, developed by Mitchell Feigenbaum, allows all non-linear systems to be analysed using the same general method of discrete mappings. Another important work to emerge was the Kolmogorov-Arnold-Moser (KAM) theorem for calculating the effect of small perturbations on the regular structure of systems and identify those perturbations causing the system to exhibit chaotic behaviour.

No real world system can be described by linear dynamical equations but by neglecting noise and other dissipative effects we can construct simplified, deterministic model systems that yield useful results and proven predictions - the most successful of which is quantum mechanics, linked to classical physics by Bohr's Correspondence Principle that states the results of classical mechanics should be recovered in the macroscopic limit.

The advances made in the field of atomic physics, some of which are catalogued in Chapter 2, has made it possible to create systems with high enough quantum numbers that enable physicists to test the Correspondence Principle and thus investigate if classically chaotic behaviour has a quantum analogue in

the semiclassical regime. The study of such systems is generally called quantum chaos.

Classical studies of chaos depend on the precise knowledge of initial conditions but such measurements are constrained by the Uncertainty Principle in quantum systems. At first glance, therefore, it would appear that it is not possible to observe chaos on the quantum scale. This apparent contradiction of the Correspondence Principle was later explained by Feynman's path integral formulation of quantum mechanics, which states that a quantum system will display the complexities of the underlying classical system. The quantum dynamics of classically chaotic systems can exhibit signatures of chaos such as 'quantum scars' (regions of enhanced probability in the wavefunction that correspond to classical periodic orbits) [30, 31] but also purely quantum effects like tunnelling [32].

Chaos can be found in surprisingly simple systems like the driven pendulum [33], the double pendulum [34] and in hydrogen atoms in magnetic [35] or microwave [36] fields. Many experimental studies have modelled quantum billiards using microwaves in cavities [37] or looked at chaotic transport in semiconductor superlattices [38] but the most utilised model is possibly the delta-kicked rotor (DKR). First proposed by Graham *et al* in 1992 [39], it has been thoroughly studied by many other groups since [40, 41, 42, 43]. Its popularity with experimentalists stems from the high degree of control available over experimental parameters and its ease of implementation.

The DKR was first realised using cold atoms in an optical lattice by Mark Raizen's group at the University of Texas [44] and this is the model system we adopt for our investigations into directed motion. To date, it has been used to investigate dynamical localisation (the quantum suppression of classical diffusion)[45]; chaos-assisted tunnelling [46]; and quantum resonances, where the effect of successive kicks accumulate constructively and the energy growth is described by anomalous diffusion [47].

3.2 The delta-kicked rotor

The classical delta-kicked rotor (DKR) is a freely rotating rotor, suspended in space and subjected to instantaneous pulses or kicks. In this instance consider a molecule (simplified to a dipole) kicked by a pulsed electric field of amplitude ϵ_0. For this planar rotor disturbed by a series of delta-function pulses according to $\sum (t - nT)$ for time t and kick period T, the Hamiltonian is a function of angular momentum, angle and time:

$$H(L, \theta, t) = \frac{L^2}{2I} + \mu\epsilon_0 cos(\theta) \sum \delta(t - nT) \qquad (3.1)$$

where I is the moment of inertia, θ is the angle the rotor makes with the vertical axis, μ is the dipole moment and L here represents angular momentum. The rotor evolves freely in time until a kick abruptly changes its angular momentum to value dependent on the angle of the rotor to the electric field at the moment it receives the kick. This free evolution is described by the first term in the Hamiltonian and the effects of the kick by the second term in equation 3.1. Hamilton's equations of motion are given by the first derivative of equation 3.1:

$$\dot{L} = -\frac{\partial H}{\partial \theta} = \mu\epsilon_0 sin\theta \sum \delta(t - nT) \qquad (3.2)$$

$$\dot{\theta} = \frac{\partial H}{\partial L} = \frac{L}{I} \qquad (3.3)$$

This deceptively simple system has no analytical solution. If L_n, θ_n label the angular momentum and angle immediately prior to kick number n and L_{n+1}, θ_{n+1} are their values preceding kick number $n + 1$, the solution to the above equation can be described by a *standard mapping* [48] that is found by integrating the equations of motion with respect to time:

$$
\begin{aligned}
l_{n+1} &= l_n - K sin(\theta_n) \\
\theta_{n+1} &= \theta_n + l_{n+1}
\end{aligned}
\qquad (3.4)
$$

where $l_n = L_n \frac{T}{I}$ is the scaled angular momentum and the stochasticity parameter, $K = \mu\epsilon_0 T^2/I$, describes the strength of the kick. Iterations of the standard
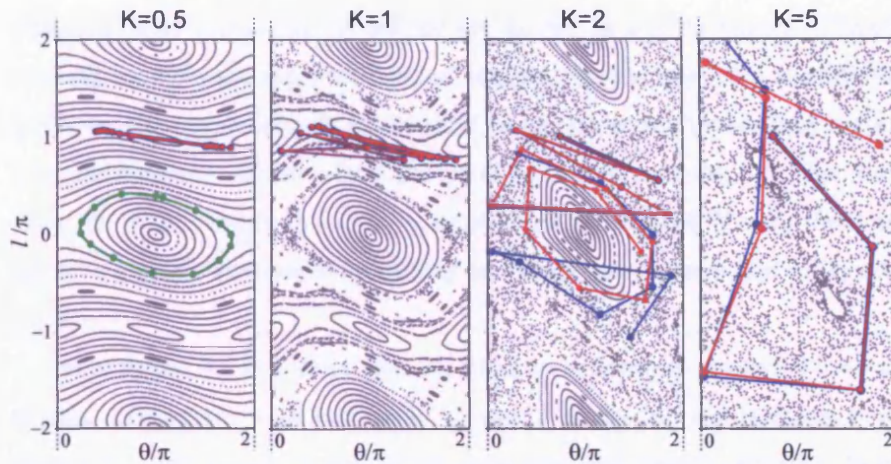
Figure 3.1: Poincaŕe surfaces of section for several values of the stochasticity parameter, $K = 0.5, 1.0, 2.0$ and 5.0. The red and blue lines join up successive iterations of the standard map, thereby plotting changes in the rotor energy over time. When $K = 0.5$ (below the critical value $K_{crit} = 0.96$), the phase space mainly comprises of stable islands and invariant curves that keep the rotor bounded in momentum. A trajectory started on stable island remains confined on it (green line). As the kick strength increases, phase space becomes more chaotic with fewer regions of integrable motion remaining. Correspondingly, the trajectories explore a larger part of the DKR phase space and the energy of the classical DKR grows diffusively.

mapping for a given set of initial conditions can be plotted as points on a two-dimensional stroboscopic plot called a Poincaŕe *surface of section*. Figure 3.1 shows four such sections of cylindrically symmetric phase space for K = 0.5, 1, 2 and 5 and two possible trajectories in each. The plots show 300 iterates of initial conditions $\theta_0 = \pi, l_0 = -2\pi + m\pi/20$ for $m = 0, 1, ..., 80$. The coloured lines illustrate the divergent behaviour of two trajectories started very close together by joining the points denoting successive iterations for two closely spaced initial conditions $(\theta, l) = (0.75\pi, \pi)$ and $(\theta, l) = (0.7505\pi, \pi)$.

The phase space predominantly shows stable trajectories or *tori* (solid black lines in figure 3.1) for small values of K that break up to form chaotic regions as the kick strength increases. The stable trajectories corresponding to regular motion are called KAM surfaces or *invariant curves* since all iterations beginning on the curve will be mapped back on to it.

The quasi-elliptical contours form what are called 'stable islands' and the

unbroken lines stretching across the are known as sealing curves. These correspond to different types of regular motion. In the case of a pendulum, for example, the stable islands correspond to libration but the sealing curves denote continuous rotation where the pendulum goes over the top. The number of stable islands depends on the magnitude of K. Beyond $K \approx 5$, there are no significant stable structures remaining and the phase space is said to be globally chaotic.

From figure 3.1 it is clear that sealing curves must be crossed if the rotor is to gain momentum with each kick. However, if any tori did intersect it would mean two distinct futures shared the same past and violate causality. In effect, the KAM surfaces restrict the rotor energy growth by separating non-integrable regions of phase space. Correspondingly, the trajectories shown by the red and blue lines for $K = 0.5$ in figure 3.1 are restricted to a very small region of phase space by KAM tori and any trajectory started on or joining a stable island remains confined to it, as shown by the green line on figure 3.1.

As the stochasticity parameter is increased, the separatrix (the demarcation between chaotic and regular regions) breaks up and chaotic regions begin to appear. At the critical value of the stochasticity parameter numerically determined by Greene [49] and estimated by Chirikov [48], $K_{crit} = 0.96$, the final invariant curve (the so-called Golden Torus [50]) is destroyed and the rotor is able to absorb energy from the external driving field.

The mean energy of an ensemble of rotors can be written:

$$E_n = \frac{\langle l_n^2 \rangle}{2} = \frac{1}{2} \sum_{m,m'=0}^{n-1} C_{m-m'} \qquad (3.5)$$

where the correlation function $C_{m-m'}$ is given by an ensemble average over all phase space:

$$C_{m-m'} = \langle K sin\theta_m sin\theta_{m'} \rangle . \qquad (3.6)$$

These kick-to-kick correlations are short-time correlations because they only depend on the time difference $(m - m')$. In the limit of large K, θ_n is assumed to

be fully randomised such that the trajectories of equation 3.4 perform a random walk in phase space and the rotor energy grows diffusively and without limit. The growth rate is described by $E = D_{ql}t$, where the *quasi-linear* diffusion constant D_{ql} is given by:

$$D_{ql} \approx \frac{K^2}{4} \tag{3.7}$$

The diffusion constant $D(K)$ deviates from its quasi-linear value because of non-zero kick-to-kick correlations at small K. A more thorough analysis by Rechester *et al* [51] that takes into account of higher order correlations shows that the diffusion constant now has an oscillatory dependence on K that varies about its quasi-linear value D_{ql}:

$$D(K) = K^2[\frac{1}{2} - J_2(K) - J_1^2(K) + J_2^2(K) + ...] \tag{3.8}$$

to the second order in Bessel functions $J_{1,2}(K)$ of K. These higher order kick-to-kick correction terms become very important later, in the case of directed motion (Chapter 5).

3.2.1 The quantum delta-kicked rotor

The quantum delta-kicked rotor (QDKR) can be treated with analogy to the classical case by replacing the angular momentum and angle variables by their respective operators, $L \to \hat{L} = -i\hbar\partial/\partial\theta$ and $\theta \to \hat{\theta}$, and iterating the rotor wavefunction Ψ using a mapping operator that is the time evolution operator of the rotor over one period τ of the driving force:

$$\Psi[(n+1)\tau] = \hat{U}\Psi(t = n\tau) \tag{3.9}$$

The system Hamiltonian comprises a kick operator and a free evolution operator that governs the system between kicks, $\hat{U}(\tau, 0) = \hat{U}_{free}\hat{U}_{kick}$, where the free evolution operator is given by:

$$\hat{U}_{free} = e^{-i\tau\hat{L}^2/2} \tag{3.10}$$

and the kick operator can be written:

$$\hat{U}_{kick} = e^{i\kappa cos(\theta)} \tag{3.11}$$

Whereas K completely specifies the classical kicked rotor, the quantum case is described by two independent control parameters (τ describing the free evolution operator, κ the kick operator) that multiply to give the stochasticity parameter $K = \tau\kappa$ and an effective Planck's constant $\hbar_{eff}$ (where $\left[\hat{L}, \hat{\theta}\right] = i\hbar_{eff}$) the unit of system action that governs how classical or quantum a system is.

The quantum case diverges from the classically predicted diffusive energy growth and saturates because of a quantum interference effect known as *dynamical localisation*. This is discussed in more detail in section 3.3.

Another purely quantum effect found in a delta-kicked rotor system is a quantum resonance. Whenever τ is an integer multiple of π, the kick evolution operator is unity and the phase of the momentum eigenstates is not randomised between consecutive kicks. The momentum imparted by each kick accumulates constructively and leads to enhanced transport such that ballistic (quadratic) energy growth may be observed instead of dynamical localisation. Quantum resonances have been thoroughly studied experimentally by Oberthaler *et al* [52] and by others in [53, 54, 55].

The presence of stable islands also cause deviations from quasi-linear diffusion. Structures that influence the system dynamics exist at any value of K, even when $K > 4$ and phase space is considered globally chaotic. In particular, stable structures dubbed *accelerator modes* result whenever K is a rational multiple of 2π because of the periodicity of phase space in momentum [47]. The position of these stable accelerator modes coincide with the maxima of the diffusion constant, which has an oscillatory dependence on K as shown by equation 3.8. Trajectories are attracted towards the accelerator modes and 'stick' to their boundaries for a large but finite number of kicks, thereby reducing transport. The introduction of this correlated behaviour (called Lévy flights) modifies the random-walk nature of diffusive energy growth (from $E = Dt$ to $E = Dt^{\mu}, \mu \neq 1$). This is known as anomalous diffusion and has been experi-

mentally demonstrated by Klappauf *et al* [47].

3.2.2 Cold atom realisation of the delta-kicked rotor

The cold atom realisation of the delta-kicked rotor (DKR) is one of the most commonly used models to study chaotic dynamics as its simplicity makes it easy to implement experimentally. Consider the behaviour of an atom in a one-dimensional standing wave of laser light: if the detuning of laser beam is much larger than the natural linewidth, the internal structure of the atom can be neglected and it can be treated as a point particle in a sinusoidal optical potential arising from the spatial variation of the AC Stark shift. Pulsing this 1-D optical lattice on for very short times simulates the delta-kicking. The Hamiltonian H describing the motion of the atom in this potential is analogous to that of a driven rotor with the exception that H is now a function of position, momentum and time $H = H(x, p; t)$ rather than angular momentum and angle:

$$H = \frac{p^2}{2M} + V_0 cos(2k_L x) \sum_n f(t - nT) \qquad (3.12)$$

where V_0 is the potential depth, M is the atomic mass, k_L is the laser wavevector and the last term describes a train of integer n square pulses of width t_p separated by a period T (where $t_p \ll T$). The equivalence of this model to the DKR can be seen if position, momentum and time are scaled to get to the dimensionless form of the Hamiltonian:

$$\mathcal{H} = \frac{\rho^2}{2} + K cos(\phi) \sum_n f(\tau - n) \qquad (3.13)$$

where scaled position $\phi = 2k_L x$, scaled momentum is given by $\rho = (4\pi T/M\lambda) \cdot p$ and scaled time $\tau = t/T$. The scaled Hamiltoninan is therefore $\mathcal{H} = \frac{\hbar_{eff} T}{\hbar} H$.

The commutation relation $[\phi, \rho] = i8\omega_r T$ defines the scaled unit of system action or effective Planck's constant $\hbar_{eff} = 8\omega_r T$ where $\omega_r = 2\pi \times 2.1$ kHz is the recoil frequency for the Cs D2 line. The stochasticity parameter is now given by:

$$K = \frac{V_0}{\hbar} \hbar_{eff} t_p \tag{3.14}$$

and the potential depth V_0:

$$\frac{V_0}{\hbar} = \frac{\pi \Gamma}{3} \times \frac{I/I_{sat}}{\Delta/\Gamma} \tag{3.15}$$

for intensity I and saturation intensity $I_{sat} = 1.12$ mWcm^{-2} for the Cs D2 cooling transition. The natural linewidth of the cooling transition is $\Gamma = 2\pi \times 5.22$ MHz and Δ is the detuning from resonance.

The stochasticity parameter can be experimentally controlled in three separate ways: by changing the potential depth, the pulse duration t_p and by the effective Planck constant $\hbar_{eff}$ via the kick period T. Due to the high degree of control available over experimental parameters, the cold atom realisation of the DKR is often used to investigate quantum chaos.

3.2.3 Experimental setup

The caesium atoms are first trapped and cooled to around 6 μK, as described in Chapter 2. These atoms are then transferred into a far-detuned optical lattice that is pulsed to simulate the delta-kicks. The lattice beams are derived from a single Coherent[1] MBR-110 Titanium:Sapphire (Ti:S) ring laser pumped by an 8W frequency-doubled neodymium-doped yttrium orthovanadate (Nd:YVO$_4$) Verdi laser. The laser output is passed through an acousto-optic modulator (AOM) and retro-reflected through the MOT vacuum cell to form a 1D intensity lattice. A halfwave-plate ensures the correct, linear polarisation of the lattice beams. The schematic of the experimental setup is shown in figure 3.2.

The Ti:S has a maximum output power of 1W at 852 nm, the Cs D2 line. Such large power is required because the potential depth $V_0 \propto I/\Delta$ but the scattering rate $\Gamma_s' \propto I/\Delta^2$, so the lattice beams must be detuned by several thousand linewidths for coherent momentum transfer. If the scattering rate is too high,

---

[1]Coherent Inc. S100 Patrick Henry Drive, Santa Clara, CA 95054, USA, www.cohr.com.
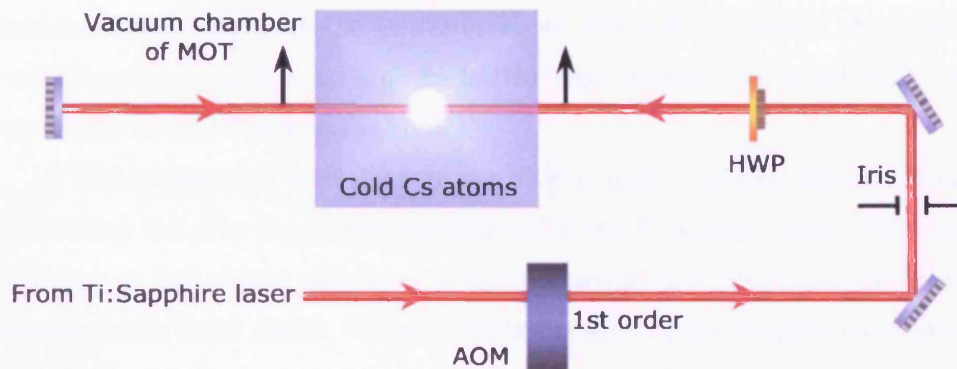
Figure 3.2: A schematic of the experimental setup used to study dynamical locali-sation. The laser beam is retro-reflected through the Cs vapour chamber to form a 1D lattice. Fast-switching of the acousto-optic modulator(AOM) pulses the lattice to simulate delta-kicking.

decoherence destroys dynamical localisation by making atomic diffusion possible once more [56] and the signal-to-noise (SNR) ratio becomes unacceptably low.

Coarse tuning of the Ti:S is achieved by micrometer adjustment of an intra-cavity birefringent plate whilst monitoring the wavelength on a wavemeter. The frequency can then be scanned over a 40 GHz range using the control panel that fine tunes a pair of intra-cavity Brewster plates. It is set at resonance with the Cs D2 line by using a beam splitter to send a small part of the beam through a Cs vapour cell and scanning for fluorescence. We do not lock the frequency using a reference cavity since the Ti:S frequency output is stable (less than 1% change) over about 15 minutes, and any drift is compensated for by resetting the frequency periodically.

A Crystal Technology[2] 3080-112 AOM controls the frequency of each beam and enables fast switching of the beam when triggered by a fast rf switch from Mini-circuits[3]. It is driven by a Rohde & Schwarz[4] SMY01 rf generator at a frequency $f = 80$ MHz. The maximum diffraction efficiency into the first order of the AOM is around 70% at 852 nm and there are slight losses at optical

[2]Crystal Technology Inc. 1040 East Meadow Circle, Paulo Alto, CA 94303, USA.

[3]Mini-circuits Europe, Dale House, Wharf Road, Frimley Green, Camberly, Surrey, GU16 6LF, www.minicircuits.com.

[4]Rohde & Schwarz GmbH & Co. KG Mühldorfstrasse 15, D-91671, München, www.rohde-schwarz.com.

interfaces that attenuate the power to about 680 mW per beam. A variable voltage source is used to control the lattice beam intensity by attentuating the amplitude of the rf sent to the AOM.

A kick sequence of fixed duty cycle $\eta = \frac{t_p}{T}$ is used to trigger fast rf switches controlling the rf to the AOMs through which the Ti:S beams pass. The pulse sequence is first drawn out using a CAD program that breaks up the whole sequence into 1024 pixels. This limits the possible pulse lengths for a given duty cycle $\eta = \frac{t_p}{T}$ as they must be a whole number of pixels. These sequences are uploaded to a Thurlby Thandar[5] TGA1230 arbitrary waveform generator where the duration of each pixel is specified. The minimum it is possible to assign is 33.33 ns per pixel but in practice the minimum pulse time is restricted by the rise time of the AOM to about 100ns. The generator is also used to set the number of kicks by looping the sequence (or part sequence) the required number of times.

A combination of changes to the beam intensity and detuning is used to set the stochastcity parameter. The error in K is estimated at around ten per cent, largely attributed to inaccuracies in measuring the Ti:S beam diameter and intensity. The diameter of the Ti:S beam must be sufficiently greater than that of the atomic cloud if we are to infer that all atoms are subject to the same value of K. If the beam is of a comparative or smaller size, the intensity variation in the beam profile suggests atoms towards the edge of the cloud will be subject to lower intensities and thus experience a smaller K.

In this case the e^{-1} beam diameter is 1.38 ± 0.05 mm and is larger than the width of the atomic cloud, estimated to be ≈ 1 mm. The likelihood of any variation in K affecting the results is further reduced by only processing a narrow strip of around 40 pixels taken through the centre of the cloud.

---

[5]Thurlby Thandar Instruments Ltd., Glebe Road, Huntingdon, Cambridgeshire, PE29 7DR, www.tti-test.com.
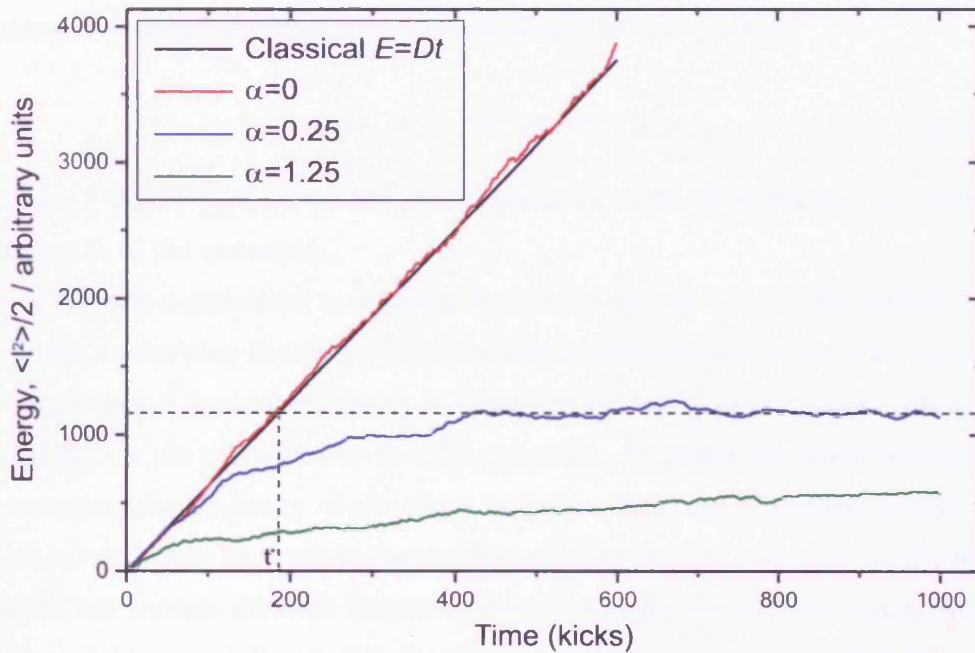
Figure 3.3: Numerical simulations of classical and quantum energy growth for various values of the effective Planck's constant is here denoted by $\alpha \equiv \hbar_{eff} = 0, 0.25, 1.25$, courtesy of [59]. The quantum case deviates from the classically predicted energy growth and instead saturates after the break time t^* (dotted lines).

3.3 Dynamical localisation

Numerical simulations have shown that contrary to the diffusive energy growth seen in the classical case when phase space is chaotic the quantum kicked rotor follows the classical energy growth for only a short time before it deviates and the energy saturates, see figure 3.3. This quantum suppression of classical diffusion is known as dynamical localisation and has been experimentally observed in many different systems. It is seen in Rydberg atoms in a microwave field where the relative probability of ionisation is suppressed compared to classical predictions [57, 58], in the dissociation of molecules by a strong monochromatic field [48] and in atom optics realisations of the kicked rotor [45, 44].

Dynamical localisation has been formally explained by analogy with Anderson localisation of electron transport in disordered solids in [60] but a simpler explanation can be given in terms of a destructive interference effect by consid-

ering the evolution of the atomic wavefunction following a kick:

$$\mid \Psi_{n+1} \rangle = e^{\frac{-ip^2}{2}} e^{iK\cos\phi} \mid \Psi_n \rangle \qquad (3.16)$$

where $\mid \Psi_n \rangle = \sum_i C_i \mid \phi_i \rangle$ can be expanded in terms of its momentum eigenstates ϕ_i of the potential.

The first exponential in equation 3.16 is the free drift term, the part of the operator governing the time evolution of the system between kicks. The second term specifies the kick operator, K. Note the frequency of the phase evolution depends on the momentum p of each eigenstate. As atoms are kicked to higher momenta, the frequency of the phase evolution increases. The wavefunction is projected over an increasingly larger number of momentum states and eventually there are enough different frequency components for destructive interference. The system can no longer absorb energy and the momentum growth is 'frozen out'.

Thus the quantum case follows the classically expected diffusive energy growth only for a short *break time*, t^*, before saturating, as shown in figure 3.3. The break time, and hence the level at which the quantum DKR energy growth saturates, depends on the effective Planck's constant:

$$t^* \approx \frac{D}{\hbar^2_{eff}} \qquad (3.17)$$

The break time is defined by the time taken to reach the saturation energy value of the quantum DKR should the energy growth follow the classical growth rate, illustrated by the dotted lines in figure 3.3.

Experimentally, dynamical localisation manifests itself with a characteristic exponential momentum profile [60, 48]. Figure 3.4 presents a series of normalised momentum distributions plotted on a natural log scale where dynamical localisation is evidenced by the straight lines forming the wings of the distribution.

For this experiment, the Ti:S output is passed through an acousto-optic modulator (AOM) and retro-reflected through the cell to form a 1D intensity lattice that is pulsed by fast switching of the AOM to simulate the delta-kicks.
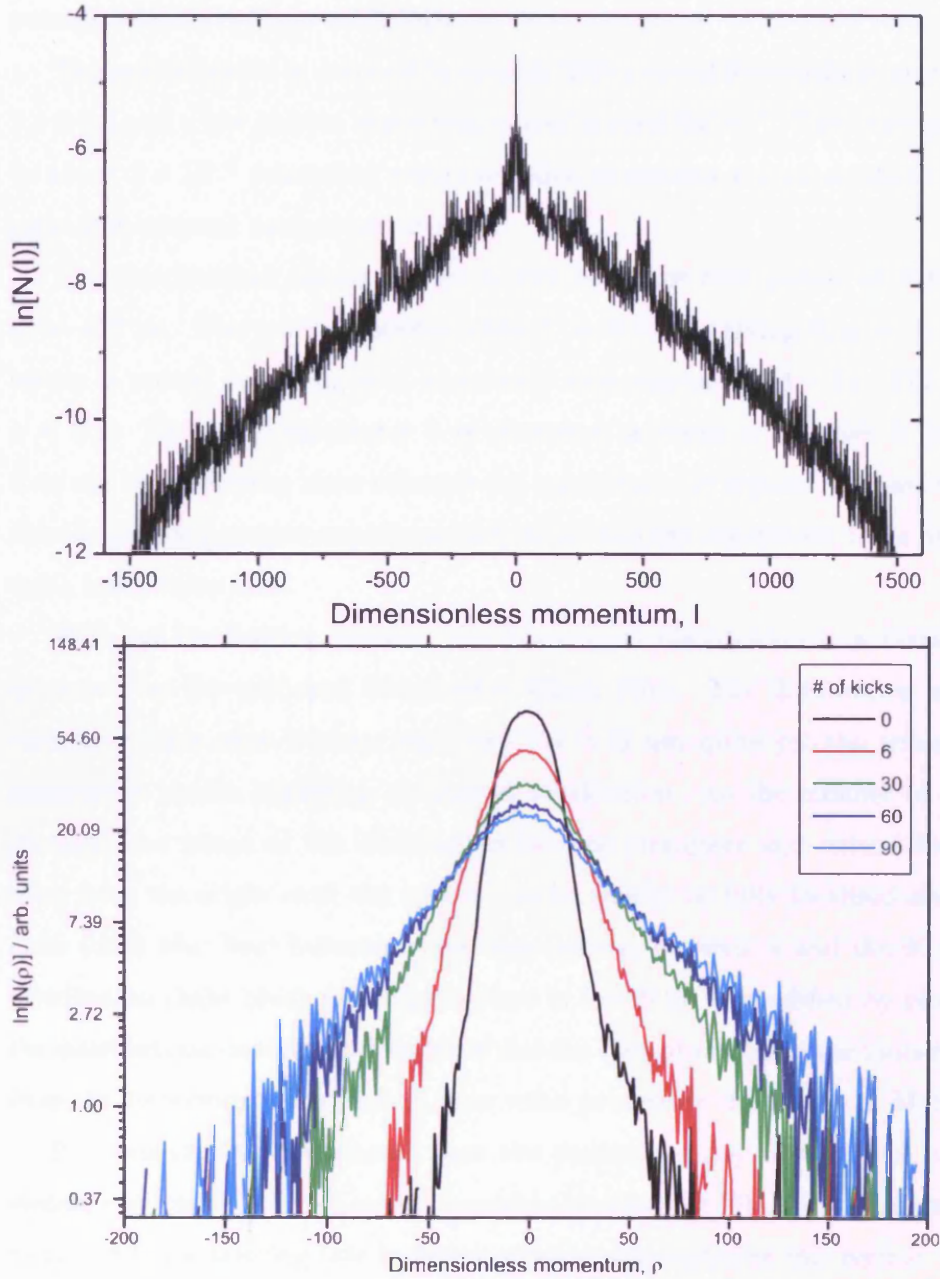
Figure 3.4: Numerical simulation (top) and experimental results (bottom) of dynamical localisation $\hbar_{eff}$ for various numbers of kicks. The simulation is for $K = 5$, 2000 kicks with momentum labelled l and the experimental results for $K = 3.4, \hbar_{eff} = 1$ (momentum labelled $\rho \equiv l$). As the number of kicks increase, the energy saturates and the distribution becomes dynamically localised.

The intensity of the Ti:S beam is approximately $I = 3000 I_{sat}$, which gives a potential depth $V_0/\hbar_{eff} = 8.2$ MHz.

The optical lattice is detuned by roughly 2000 natural linewidths to give $K = 3.4 \pm 0.3$ and a low photon scattering rate of around $500 \ \text{s}^{-1}$. This corresponds to about 2×10^{-4} scattering events per kick so ensures a good signal-to-noise ratio and coherent momentum transfer.

The distributions shown are for a kick sequence with pulses of duration $t_p = 417$ ns. The period between kicks $T = 9.47 \ \mu\text{s}$, giving $\hbar_{eff} = 1$. The lattice is pulsed according to a bi-periodic kick sequence $T(1 - b) : T(1 + b)$, $b = 0.2$. The chirp parameter b is discussed in detail in Chapter 5, suffice it to say that chirping kicks enlarges the non-integrable regions in phase space thereby allowing greater experimental freedom and the experiment to be carried out a lower value of K.

With no localisation present, the momentum distribution is a Gaussian, as shown by the unkicked distribution (black line). The distribution shows straighter sides after 6 kicks (red line) but it is not quite yet the triangular momentum profile signifying dynamical localisation. As the number of kicks increase, the wings of the distribution become straighter and extend further away from the origin until the system can be said to be fully localised after 60 kicks (dark blue line) because of the near overlap between it and the 90 kicks distribution (light blue). The signal noise at low $N(\rho)$ is amplified by plotting the distributions on a natural log scale and the discontinuities in the plots result from the background subtraction done when processing the results in Matlab.

Previous studies have shown that the presence of any decoherence in the system can destroy the effects of dynamical localisation [61], so it is important to have a low scattering rate in future experiments exploring this regime.

The localised momentum distributions can be expressed using the form $N(\rho) = exp(-\rho/L)$, where L is the localisation length and can be used to characterise dynamical localisation. The localisation length is given by [62]:

$$L \approx \frac{K^2}{4\hbar_{eff}} \tag{3.18}$$

The factor of 1/4 was determined numerically by Shepelyansky [63] and is specific to the case where the rotor evolution is described by the Standard Map (i.e. periodic kick sequences). The localisation length is related to the break time by:

$$t^* \approx \frac{L}{\hbar_{eff}} \tag{3.19}$$

In a plot of $\ln[N(\rho)]$ vs ρ, the localisation length is given by $\frac{d[ln(N(\rho))]}{d\rho} = -\frac{1}{L}$. A linear fit to to the wings of the momentum distribution can therefore be used to estimate L. Figure 3.5 presents our results for the average localisation length L as a function of the square of the stochasticity parameter K^2. This experiment is conducted similarly to the previous one, with the exception that the kick sequence employed here is periodic such that equation 3.18 remains valid. The gradient given by a linear fit (red line) to this plot is $\frac{1}{4*\hbar_{eff}}$ according to equation 3.18 so can be used to estimate the effective Planck's constant of the system.

In calculating L here, the gradient of a wing is measured from only the middle portion of the dataset; the data near the peak is unreliable because the spatial and velocity distributions are not deconvolved from each other and we also neglect the very noisy data at the edge of the distribution. Note that the vertical scale on the plot of experimental data in figure 3.4 is regardless labelled $N(\rho)$, since at no point in this thesis do we deconvolve the two distributions.

The value of K is varied by adjusting the rf level to the acousto-optic modulator controlling the lattice beams. The minimum value of K used is 3.4, so that phase space is predominantly chaotic, and the maximum possible value ($K = 12.8$) is limited by noise. In each case the beams are 3000Γ detuned from resonance and the kick sequence used has 30 pulses of $t_p = 307$ ns at intervals of $T = 20.4\mu s$, which corresponds to an effective Planck's constant of $\hbar_{eff} = 2.2$. A quick calculation of the standard map break time for the largest value of K used, $\frac{t^*}{T} = 5$, suggests 30 kicks is ample to guarantee dynamical localisation.
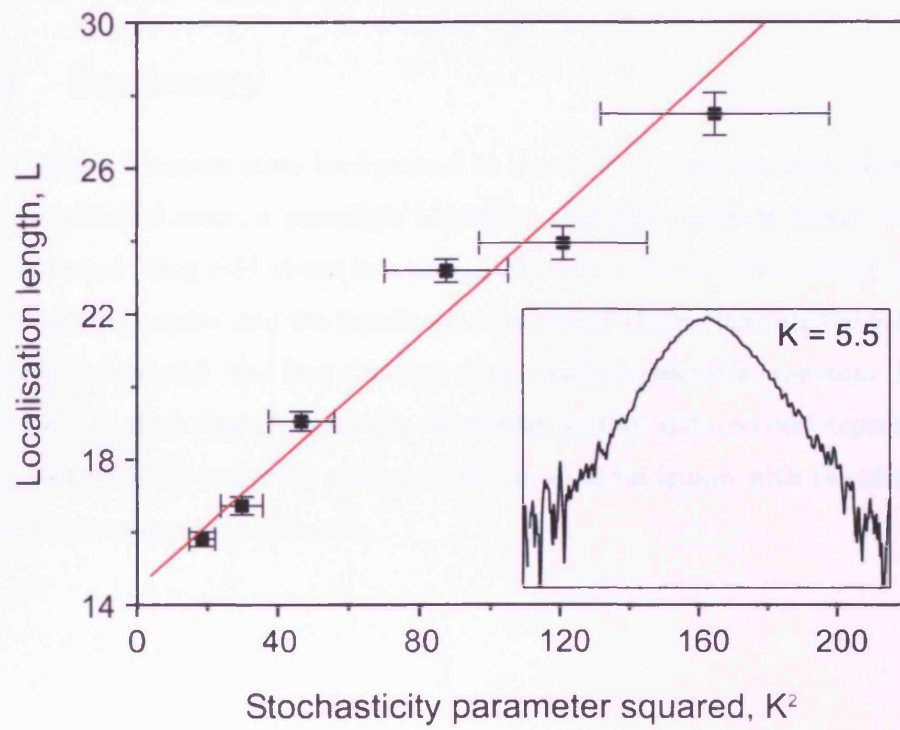
Figure 3.5: A plot of localisation length L against the stochasticity parameter squared K^2. The red line is a linear fit to the data. *Inset:* A typical dynamically localised momentum profile that has been smoothed using five point adjacent averaging, from the $K = 5.5$ data point.

The localisation lengths are calculated as before but the distributions are first smoothed by five point adjacent averaging. A momentum distribution is shown for one of the data points, specifically $K = 5.5$, in the inset of figure 3.5. The data gives a value of $\hbar_{eff} = 2.9 \pm 0.3$, in close agreement with what is expected. Any deviation at large K is most likely due to a high scattering rate (over 900 scattering events per second) that resulted in decoherence, whilst the presence of stable islands affects diffusion (hence L) at small K.

3.4 Summary

This chapter presents some background to the topic of chaos and describes how the delta-kicked rotor, a paradigm model for studying quantum chaos, can be implemented using cold atoms in a pulsed 1D optical lattice. The results of two simple investigations into the signatures of quantum chaos illustrate the validity of using this model: the first showing dynamically localised momentum distributions with their characteristically triangular profiles and a second experiment demonstrating the expected scaling of the localisation length with the effective Planck's constant of the system.

Pulse shape effects in the delta-kicked rotor

The closest experimental approximation to delta-kicks we can achieve is a train of square pulses of narrow but finite temporal width t_p. This approximation causes deviations from the expected behaviour of the DKR by modulating the kick strength such that it falls to zero at certain momenta. This 'momentum boundary' limits the phase space available for atomic diffusion to within the confines of a certain range of momenta, the width of which depends on the pulse duration t_p.

This chapter presents experimental evidence for the presence of the momentum boundary and describes how it may be used in conjunction with the moving lattice technique to achieve asymmetric momentum diffusion. The moving lattice method (detailed in section 4.2) may also be used to explore the regions of phase space beyond the boundary.

4.1 The momentum boundary

The momentum boundary is a barrier to diffusion arising from the approximation of delta-kicks by finite width pulses. Initially studied by Blümel *et al* in the context of molecular rotation excitation [48] and later for cold atoms in a pulsed optical potential by Mark Raizen's group at the University of Texas [62], the

presence of the momentum boundary in the cold atom realisation of the DKR is most easily explained in terms of the semiclassical picture of an atom moving in a 1D potential.

As the atom moves a finite distance over the duration of a kick, the overall value of the kick strength must be averaged over t_p. If the atom travels a whole lattice period during one kick, the kick strength averages to zero and the atom is said to have reached the momentum boundary. This occurs when $p = p_b = \pm M\lambda/2t_p$, or in dimensionless units:

$$\rho_b = \pm \frac{M\lambda^2}{8\pi\hbar t_p}\hbar_{eff} = \pm 2\pi \frac{T}{t_p} \tag{4.1}$$

A more detailed analysis by Klappauf *et al* [64] has shown that the stochasticty parameter is related to the pulse shape through its Fourier transform which, for a square pulse, leads to a momentum-dependence in K of the form:

$$K_{eff} = \frac{K\sin(\pi\rho/\rho_b)}{\pi\rho/\rho_b} \tag{4.2}$$

The positions of the momentum boundaries correspond to the zeroes of the equation 4.2, with the first boundary given by equation 4.1.

Figure 4.1 depicts the rotor phase space for finite width kicks and for 120 iterations of the standard map when $K = 5.3$. The momentum boundary is at $\rho_b = 42.5 = 13.5\pi$ and all trajectories are started within $\rho = \pm\rho_b$ (left panel). The rotor phase space is predominantly chaotic but restricted to a strip $\rho = 2\rho_b$ wide. That is to say, diffusion is limited to the region encompassed by momentum boundary for atomic trajectories started within $\pm\rho_b$.

An enlargement of the region around the momentum boundary with trajectories started either side of ρ_b (right panel) reveals a narrow, integrable band parallel to the position (ϕ) axis. There is no energy growth in this area but chaotic regions in which diffusive energy growth is possible can be found either side of ρ_b.

Figure 4.2 presents results showing the effect of the momentum boundary on an atomic distribution prepared around $\rho = 0$. The experimental procedure
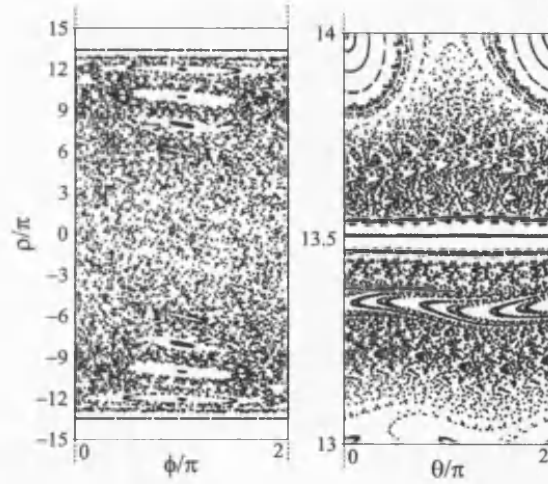
Figure 4.1: The rotor phase space for $K = 5.3$, 120 kicks with the momentum boundary at $\rho_b = 13.5\pi$ (left). The right panel is an enlargement of the region around the momentum boundary, showing the region of regular motion at $\rho = \rho_b$.

and setup are similar to that of the investigations into dynamical localisation (see figure 3.2 in Chapter 3 for a schematic of this setup). Caesium atoms are laser cooled to around 6 μK then loaded into a 1D lattice formed by retro-reflecting a single laser beam through the vacuum chamber of the MOT. The lattice is pulsed to give 120 kicks for each experimental cycle by fast switching of the acousto-optic modulator controlling the laser beam. The beam intensity is roughly $I/I_{sat} = 2900$ and the laser is 4000Γ detuned from resonance to give a potential depth of approximately $V_0/\hbar = 3.9$ MHz. The kick period in all cases is $T = 18.9\mu$s, which gives an effective Planck's constant value of $\hbar_{eff} = 2$.

The black line shows a typical dynamically localised distribution for $K = 3.0, t_p = 379ns$. The momentum boundary is located at $\rho_b = 319$, too far away for it to have any effect on the momentum profile. As the pulse time is increased to $t_p = 947$ ns ($K = 7.4$, red line) and the momentum boundary is reached, there is a sharp drop in the momentum profile at a point $\rho \approx \rho_b = 128$.

The blue line shows how a further increase in the pulse time to $t_p = 1894$ ns ($K = 14.8, \rho_b = 63.8$) brings the momentum boundary even closer to the origin. The cut-off is not as pronounced as before and the distribution looks rounded due to the closeness of the boundary. The noise recorded in this experiment is
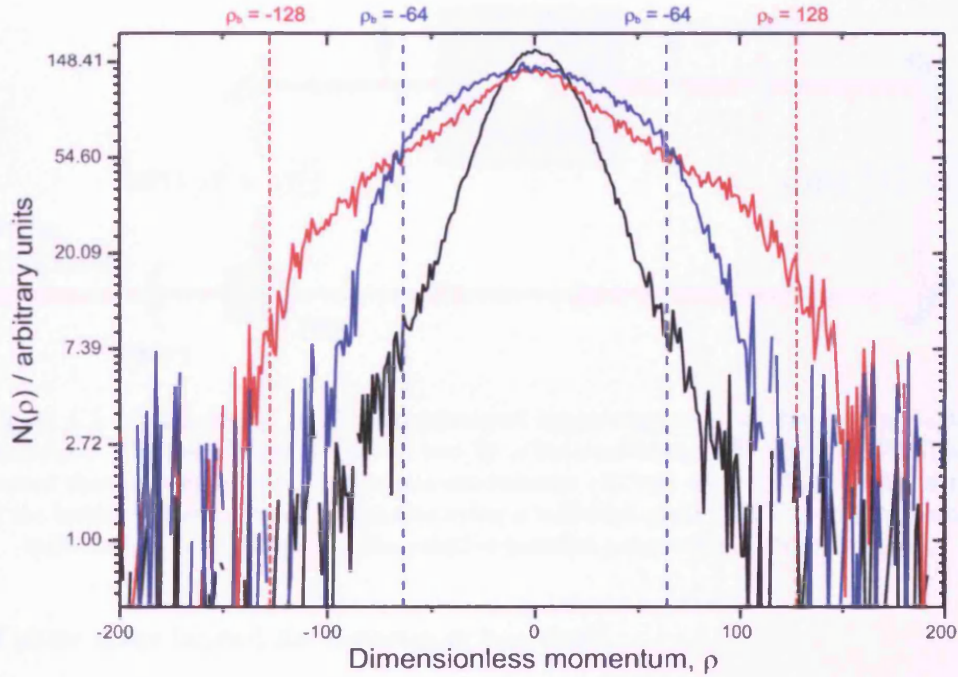
Figure 4.2: Experimental results showing the sharp fall-off in the momentum profile associated with the momentum boundary for $\rho_b = 63.8, 128$ (vertical dotted lines).

amplified for small intensities by plotting the results on a natural log scale.

Recall that the diffusion constant $D \propto K^2$ and that using square pulses instead of delta kicks means D now has sinc-squared dependence on momentum with $D(K_{eff}, \rho)$ falling to zero at the momentum boundary. The break time t^* is proportional to the diffusion constant so undergoes a similar modulation. The finite-width kick approximation, therefore, affects both how long and how fast the atoms absorb energy from the driving field and has a significant effect on momentum diffusion.

The atoms in the part of the distribution positioned closer to the boundary will only have a short time over which they can absorb energy from the driving field and their kinetic energy growth ($E \propto Dt$) will be zero at $\rho = \rho_b$. Our moving lattice technique, detailed in the next section, provides an easy way of changing the initial atomic momentum to investigate what effects the boundary may have on diffusion and also to position the atomic distribution in the region
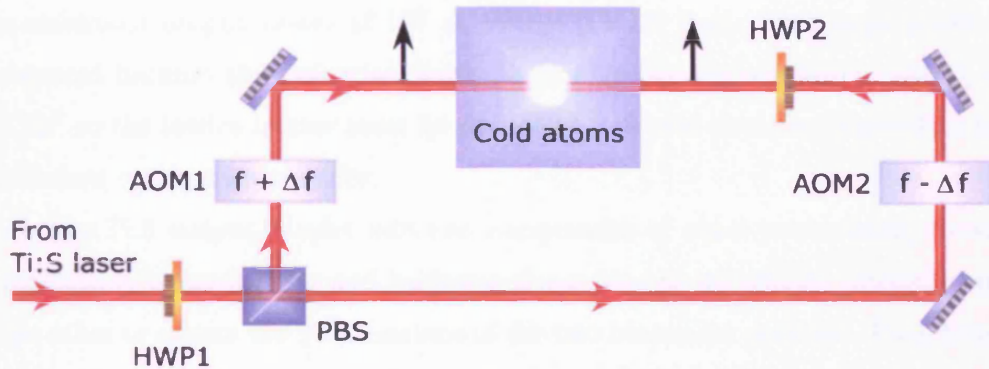
Figure 4.3: A schematic of the experimental apparatus used in the moving lattice technique. The laser beam is split in two by a beamsplitting cube (labelled PBS) and passed through separate acousto-optic modulators (AOM1 and AOM2). Both 'arms' of the lattice are set at equal intensities using a halfwave-plate (HWP1) and the second halfwave-plate (HWP2) sets the relative parallel polarisations (black arrows).

of phase space beyond the momentum boundary.

4.2 The moving lattice technique

The ability to control the initial atomic momentum allows access to all of the rotor phase space. One method of controlling the initial atomic momentum ρ_0 by cooling to a non-zero velocity by the addition of a uniform magnetic field [65, 66]. Here, however, we introduce a small frequency difference between the lattice beams to form a 1D travelling interference pattern in the laboratory frame. The atoms remain stationary but have a non-zero initial atomic momentum ρ_{L0} in the frame of the moving lattice. A schematic of the experimental setup used to produce the moving lattice is shown in figure 4.3.

The caesium atoms are first trapped and cooled to around 6 μK, as described in Chapter 2. These atoms are then loaded into a far-detuned optical lattice that is pulsed to simulate the delta-kicks. Unlike the setup used to investigate dynamical localisation and the momentum boundary, where the lattice was formed by a single retro-reflected beam, two counter-propagating beams with parallel linear polarisations are overlapped to form the 1D potential.

These beams are derived from a single Titanium-Sapphire (Ti:S) laser with

a maximum output power of 1W at 852nm (Cs D2 line). Such large power is required because the potential depth $V_0 \propto I/\Delta$ but the scattering rate $\Gamma'_s \propto I/\Delta^2$ so the lattice beams must be detuned by several thousand linewidths for coherent momentum transfer.

The Ti:S output is split into two components of equal power using a combination of beam-splitter and halfwave-plates (one to set relative intensity and the other to ensure the polarizations of the two beams are parallel). Each beam is then passed through a separate acousto-optical modulator (AOM) driven by two phase-locked Rohde & Schwartz SMY01 rf generators at a frequency $f = 80$ MHz. The two first order beams counter-propagate through the vacuum chamber of the MOT to form the kicking potential.

The maximum diffraction efficiency into the first order of the AOM is around 70% at 852 nm and there are slight losses at optical interfaces that attenuate the power to about 275 ± 5 mW (measured) in each beam. Both AOMs are triggered by an arbitrary waveform generator as described in the previous chapter.

The two Crystal Technology 3080-112 AOMs allow independent control over the frequency of each beam, enabling a small frequency difference $2\Delta f$ to be introduced between them that causes the lattice to move at a speed $\lambda \Delta f$ ms^{-1} in the laboratory frame. The atoms remain stationary but have a non-zero initial mean momentum ρ_{L0} in the frame of the moving lattice that can be controlled by changing the magnitude of Δf. Note the subscript 'L' is used to denote the co-moving frame.

Other methods used to introduce a non-zero ρ_0, such as cooling to a non-zero velocity by the addition of a uniform magnetic field [66, 65], broaden the atomic distribution and alter the position of the atoms on the imaging screen, thus limiting such techniques to the field of view of the camera. Our method ensures the atoms remain centred on the camera screen.

The maximum frequency difference it is possible to introduce when $f = 80$ MHz is $\Delta f = \pm 1.25$ MHz on these rf synthesizers. In practice this is further restricted to ± 1 MHz, a limit set by the deflection of the first order beam from the AOM ($\Delta \theta / \Delta f \approx 0.1°$/MHz) and equivalent to a maximum possible

$p_L/2\hbar k_L \approx 120$. Beyond 1 MHz, the beams move off the atomic cloud which diminishes the kick strength and some realignment of the kicking beams is required.

The mean momentum is taken to be the first moment of a background-corrected Gaussian spatial distribution, $\langle \rho \rangle = \dfrac{\int \rho N(\rho) d\rho}{\int N(\rho) d\rho}$, and the atomic energy is quantified by the second moment:

$$E = \frac{\langle \rho^2 \rangle}{2} = \frac{\int \rho^2 N(\rho) d\rho}{2 \int N(\rho) d\rho} \tag{4.3}$$

The errors are calculated using the standard deviation of the five frames averaged to give the intensity distribution (i.e. $N(\rho)$) for each data point.

4.3 Transport by restricting phase space

The sinc-squared modulation discussed in section 4.1 can be used in conjunction with the moving lattice technique to generate highly asymmetric momentum diffusion in the DKR. Consider the variation of the diffusion constant as a function of momentum, as shown in figure 4.4. When the distribution is centred at the maximum of $D(K, \rho_{L0})$ at $\rho_L = 0$ (red line), the atoms are free to diffuse equally far in both directions (indicated by the solid red arrows) before reaching the momentum boundary. Both wings of the atomic momentum distribution experience approximately the same diffusion constant and the resulting momentum diffusion is symmetric.

If the atomic distribution is placed further away from the main peak, for example at $\rho_{L0} = 29.2$ (in green), the diffusion constant is locally asymmetric such that phase space available to the atoms is more restricted on one side than the other. This leads to highly asymmetric diffusion, illustrated by the unequal thicknesses of the green arrows. Positioning the atoms on the momentum boundary, $\rho_{L0} = 2\pi T/t_p = 43$ in dimensionless units, results in very little diffusion because $D(K, \rho_L)$ is so small. There is however a slight difference in the magnitude of the diffusion constant across the atomic distribution due to the relative sizes of the maxima of $D(K, \rho_L)$.
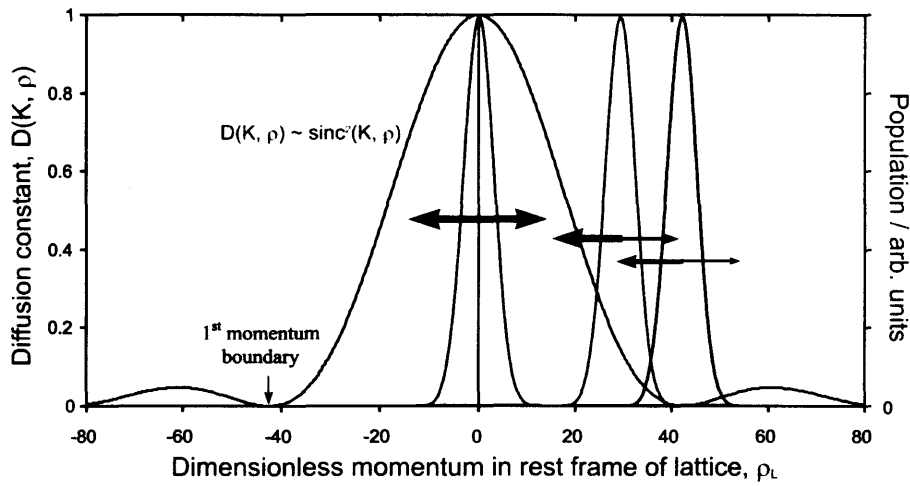
Figure 4.4: The sinc-squared modulation of the diffusion constant as a function of dimensionless momentum ρ_L, the atomic momentum in the moving lattice frame. The initial atomic distribution centred at $\rho_{L0} = 0$ (red) can expand symmetrically but the distribution centred near $\rho_{L0} = 29.2$ (green) cannot as it is severely constrained by the momentum boundary. A little diffusion is possible when the atoms are centred on the momentum boundary itself ($\rho_{L0} = 42.5$, blue) because the wings of the distribution can experience a small, locally asymmetric $D(K, \rho)$. The thickness of the arrows denotes the relative magnitude of the diffusion in the indicated direction.

Figure 4.5 presents some momentum profiles for various values of initial atomic momentum, $\rho_{L0} = 0, 29.2, 42.5$ in an experiment where the momentum boundary occurs at $\rho_b = 42.5 = 13.5\pi$ and $K = 5.3$. The horizontal axis is the dimensionless momentum in the lab frame ρ so the momentum boundary $\rho_b = 42.5$ is displaced by an amount ρ_{L0} in each case.

The experimental parameters are $t_p = (1.42\pm0.02)\mu s$ and $T = (9.47\pm0.02)\mu s$ such that $\hbar_{eff} = 1$ for the results shown. The atomic distribution is positioned at different points along the $D(K_{eff}, \rho)$ curve using the moving lattice technique.

The black line shows the initial or 'unkicked' distribution. If the atoms are positioned at $\rho_{L0} = 0$ ($\Delta f = 0$ kHz, red line), momentum diffusion is very nearly symmetric. The slight asymmetry is probably due to a small misalignment of the beams that form the kicking potential. The shoulder in the momentum profile approximately coincides with the position of the momentum boundary $\rho_b = 43 \pm 1$.

Preparing the distribution at $\rho_{L0} = 29.2$ ($\Delta f = 245$ kHz, green line) results in a highly asymmetric momentum profile because the atoms experience a locally asymmetric diffusion constant that is near-zero at the positive momentum side of the distribution.

There is very little diffusion when the atomic distribution is positioned very close to the momentum boundary, $\rho_L = 42.5$ ($\Delta f = 350$ kHz, blue line). A small amount of diffusion is present because the wings of the atomic distribution can experience a non-zero, locally asymmetric diffusion constant even though the main peak is centred on the momentum boundary. Diffusion towards negative momenta will be greater than diffusion to the right due to the relative sizes of the maxima of $D(K_{eff}, \rho_L)$.

Figure 4.6 highlights the asymmetry present in the momentum profiles of figure 4.5 by plotting $|\rho| . N(\rho)$ as a function of the atomic momentum in the laboratory frame. The dotted lines mark the positions of the momentum boundary in the laboratory frame. For the atomic distribution centred at $\rho_{L0} = 0$ (red), there is reasonable agreement between the position of the momentum boundary $\rho_b = 42 \pm 1$ and the fall-off in diffusion.
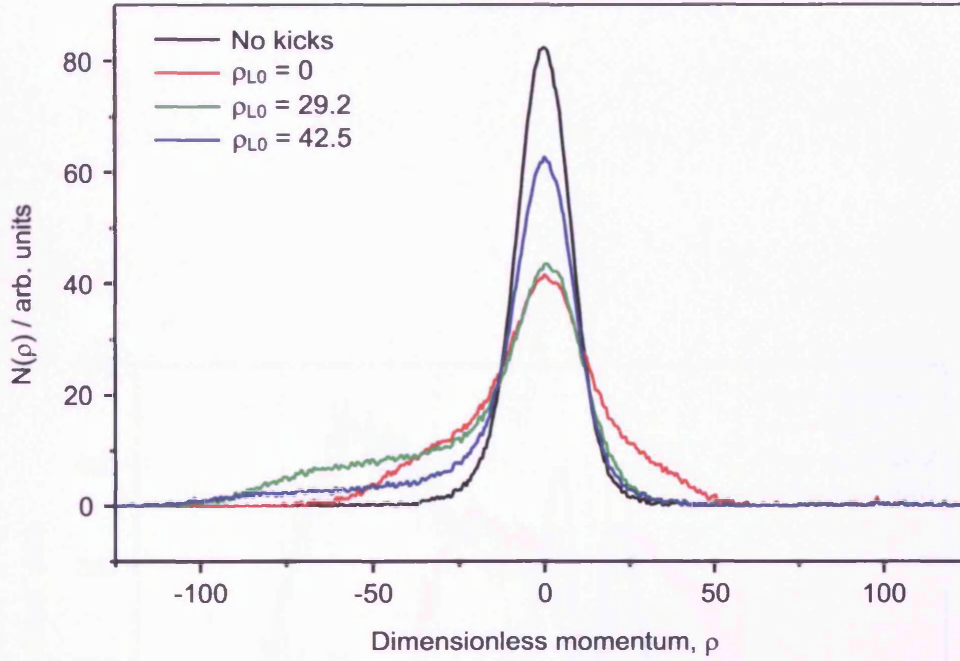
Figure 4.5: Generating asymmetric diffusion by restricting the rotor phase space. In this experiment, the momentum boundary is at $\rho = 42.5$. When the atomic distribution is positioned at $\rho_L = 0$, momentum diffusion is (almost) symmetric. At $\rho_L = 29$ (red line) the positive side of the momentum distribution (on the right) experiences a much smaller diffusion constant, which results in a highly asymmetric momentum profile. There is very little diffusion when the atomic distribution is positioned very close to the momentum boundary, $\rho_L = 42.5$ (blue line). The unkicked distribution is given by the black line.

When $\rho_{L0} = 29$ (green), the momentum boundary is at $\rho_b = 14 \pm 1, -72 \pm 2$ and we have the largest momentum asymmetry. There is very little diffusion towards positive momenta, whilst for negative momenta diffusion increases until the momentum boundary then begins to decrease.

When $\rho_{L0} = 42.5$ (in blue), the momentum boundary is given by $\rho_b = 0, -85 \pm 2$ in the laboratory frame. Diffusion towards positive momenta is minimal (c.f. the unkicked distribution) and the small amount of diffusion towards negative momenta drops sharply beyond the momentum boundary.

The asymmetry seen in figures 4.5 and 4.6 is quantified by the first moment of the atomic distribution, as discussed in Chapter 2, section 2.2 and in section 4.2. Figure 4.7 plots this asymmetry as a function of the atomic momentum in
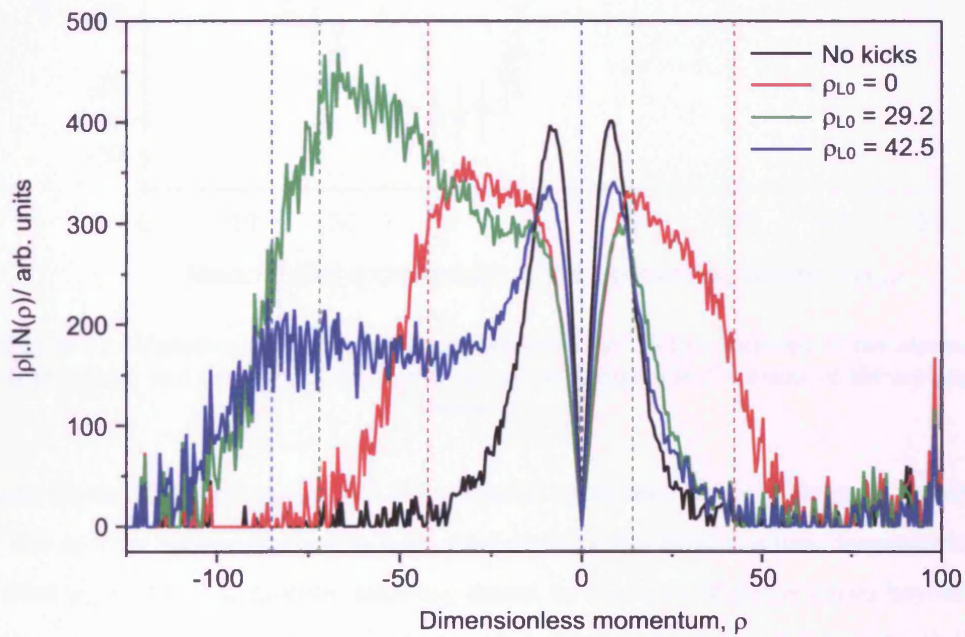
Figure 4.6: The asymmetry is highlighted by plotting $|\rho|.N(\rho)$ as a function of the dimensionless momentum in the laboratory frame ρ for initial atomic momenta in the co-moving frame $\rho_{L0} = 0$ (red), 29 (green), 42.5 (blue). The position of the momentum boundary, shown by dotted lines of a matching colour, is accordingly shifted by an amount ρ_{L0} in the lab frame. The unkicked distribution is given by the black line.
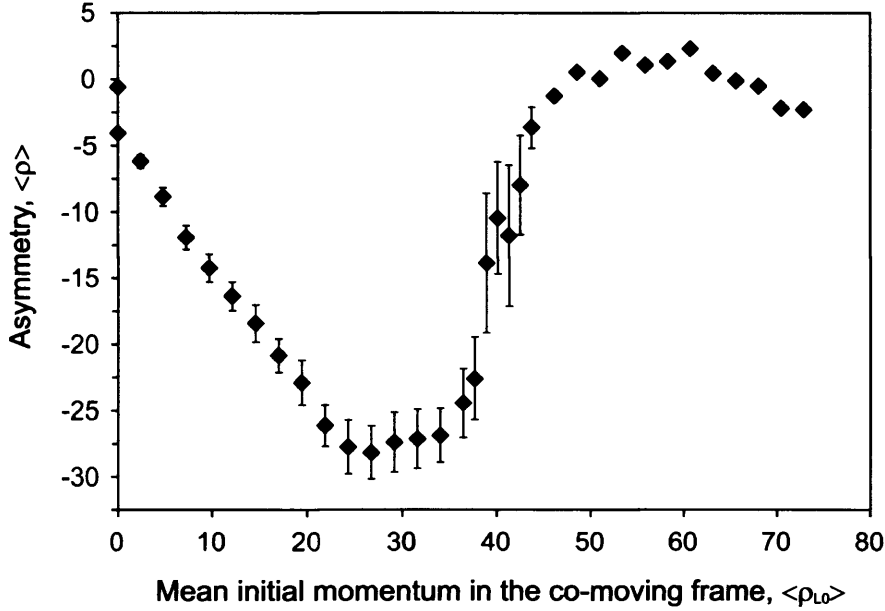
Figure 4.7: Variation of the asymmetry, quantified by the first moment of the atomic distribution, as a function of the initial atomic momentum in the frame of the moving lattice ρ_{L0}.

the frame of the moving lattice for the same experimental parameters as above. The moving lattice method is now used to vary the initial atomic momentum from $\rho_L = 0$ to 73, thereby allowing access to the area of phase space beyond the momentum boundary (which cannot be reached using a static potential) and demonstrating the utility of this technique.

The distribution is initially (almost) symmetric so the momentum asymmetry is close to zero. As ρ_L increases, the phase space becomes restricted on one side by the momentum boundary, which causes an asymmetry in the momentum profile. The asymmetry is dependent on both the gradient of the diffusion constant $(\partial D/\partial\rho)$ and that of the break time $(\partial t^*/\partial\rho)$. The magnitude of the asymmetry $|\langle\rho\rangle|$ roughly follows this trend: it is largest between $20 > \rho_{L0} > 40$, when the difference of $D(K, \rho_{L0})$ across the atomic distribution is maximal, and very nearly falls to zero at the positions of the momentum boundary.

There is a small but finite $\langle\rho\rangle$ in the area past the first momentum boundary.

The size of the asymmetry in this region is smaller than that in the area before the first boundary because $D(K_{eff}, \rho_L)$ is smaller in this region and is positive (unlike the current between $0 < \rho_L < 42.5$) because the gradient of the diffusion constant is of opposite sign.

The finite pulse width approximation to delta kicks can, therefore, have a significant effect on atomic diffusion. The presence of the momentum boundary can produce an asymmetry in the momentum profile so particular care must be taken in future investigations of directed diffusion to ensure the boundary is positioned far away from the region of interest. The results of this section are also presented in [67].

4.4   Exploring mixed phase space

This section presents results of an exploration of the rotor phase space to illustrate the efficacy of our moving lattice technique by mapping stable structures in phase space as a function of the atomic momentum in the frame of the lattice, ρ_L. In addition to being used to generate directed transport by engineering barriers to diffusion in the system's phase space [67], this method may prove to be a useful tool in investigating chaos-assisted tunnelling between two phase space resonances (corresponding to regions of regular motion) in the quantum driven pendulum [68] or in realising a purely deterministic Hamiltonian ratchet [69].

The behaviour of atoms in the vicinity of stable islands has been studied previously in the context of accelerator modes [47]. These islands represent regular motion and trajectories starting on or joining a stable island will always be mapped back on to it, thereby reducing momentum diffusion. Their presence restricts the atomic energy growth so will be seen as dips in a plot of the atomic energy against ρ_L. The energy growth is investigated for various kick strengths for two different values of the effective Planck's constant, $\hbar_{eff} = 0.25$ and 1.

Figure 4.8 shows numerically obtained phase space portraits for values of the stochasticity parameter used in this experiment, $K = 0.7, 1.5, 2.7, 4.1$. At the
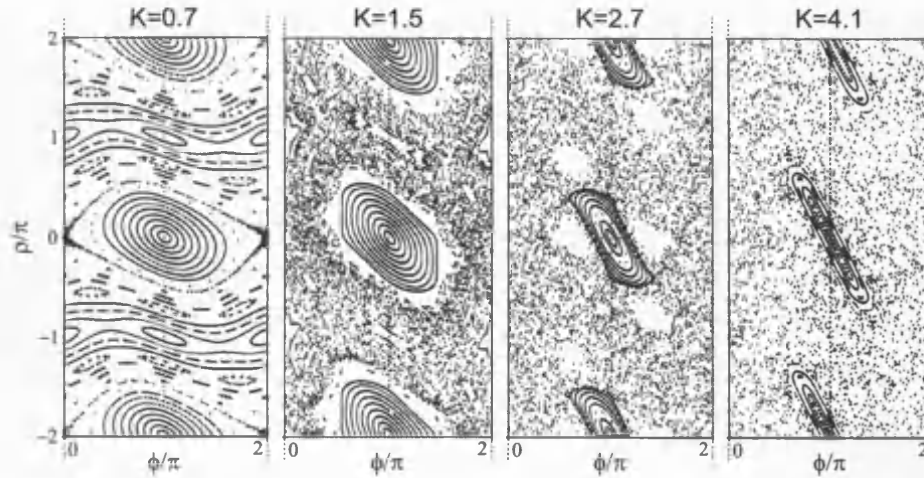
Figure 4.8: Poincaré section plots of phase space for different values of kick strength parameter, $K = 0.7, 1.5, 2.7, 4.1$. Dimensionless momentum is shown on the vertical axis, dimensionless position on the horizontal axis. When K is small, phase space exhibits regular, unbroken structures that limit the energy growth of the atoms. As K increases, the contours (or tori) break up, allowing the atoms to gain energy by executing a random walk in the chaotic regions of phase space.

smallest kick strength $K = 0.7$, the rotor phase space has large stable islands located at $\rho/\pi = 0, \pm 2$. This is below the critical value of $K = 0.96$ so very little atomic energy growth is possible. As the kick strength is increased, phase space becomes increasingly chaotic and the stable islands (which remain centred in the same position) shrink in size.

The experimental method follows the discussion of the previous section, with Cs atoms laser cooled to 6 μK and the detuning of the kicking potential varied between 500 and 5000 natural linewidths to get the above range of K. Cooling to this temperature corresponds to an initial $1/\sqrt{e}$ momentum width of $\sigma_p = 0.69 \pm 0.06$ for $\hbar_{eff} = 0.25$ and $\sigma_p = 2.7 \pm 0.6$ for $\hbar_{eff} = 1$.

It is necessary for the the pulse width $t_p \ll T$ to avoid the presence of the momentum boundary, which can have a significant effect on diffusion as demonstrated elsewhere in this chapter. The kick sequence for $\hbar_{eff} = 0.25$ had a pulse duration of $t_p = 379 \pm 20$ ns and a period of $T = 2.37 \pm 0.20 \mu$s whilst $t_p = 296 \pm 20$ ns, $T = 9.47 \pm 0.02 \mu$s for $\hbar_{eff} = 1$. The differences in t_p result from the limitations of the CAD program used to draw the waveforms.

The results are presented in figure 4.9. For both cases of $\hbar_{eff} = 0.25$ and 1 and at small values of K, stable islands significantly affect diffusion and the results clearly reflect the 2π separation of the stable islands in phase space. There is a peak in the energy growth when the initial momentum is such that the majority of atoms are situated in a chaotic region. Conversely, when the initial momentum is such that the atomic distribution is positioned over a stable structure, the energy growth is minimal but does not fall to zero because, although the distribution may be directly centred on an island, the wings of the distribution can extend into the chaotic regions making diffusion possible for a small number of atoms.

There is very little energy growth at $K = 0.7$, as expected, since tori still exist to keep the atomic momentum bounded. As the stochasticity parameter is increased, these tori vanish and the momentum width of the stable islands decreases. A smaller fraction of atoms are now constrained in momentum because the width of the atomic distribution remains fixed and the corresponding increase in the peak atomic energy for larger K can be seen in our results.

The minimum atomic energy will be higher for larger values of K because the smaller stable islands mean a larger number of atoms will lie outside the contours of these structures and be free to move. At $K = 4.1$, phase space is nearly globally chaotic and the 2π periodicity is correspondingly (almost) absent.

Our ability to resolve stable structure in phase space depends on the dimensionless width of the initial atomic distribution and hence on the value of $\hbar_{eff}$. The dimensionless width of the initial distribution is $\sigma_p/\pi = 0.22$ for $\hbar_{eff} = 0.25$ and $\sigma_p/\pi = 0.87$ for $\hbar_{eff} = 1$, so a small $\hbar_{eff}$ gives a narrow distribution that allows for greater resolution (figure 4.10).

As $\hbar_{eff}$ increases, the wings of the atomic distribution spread further across phase space and a larger proportion of atoms reside over chaotic areas. When $\hbar_{eff} = 0.25$, approximately 98% ($\pm$ 3 standard deviations (s.d.'s) from the mean) of the atomic distribution falls within the stable island when $K = 0.7$ but is distributed over a significantly larger area (nearly all of the phase space
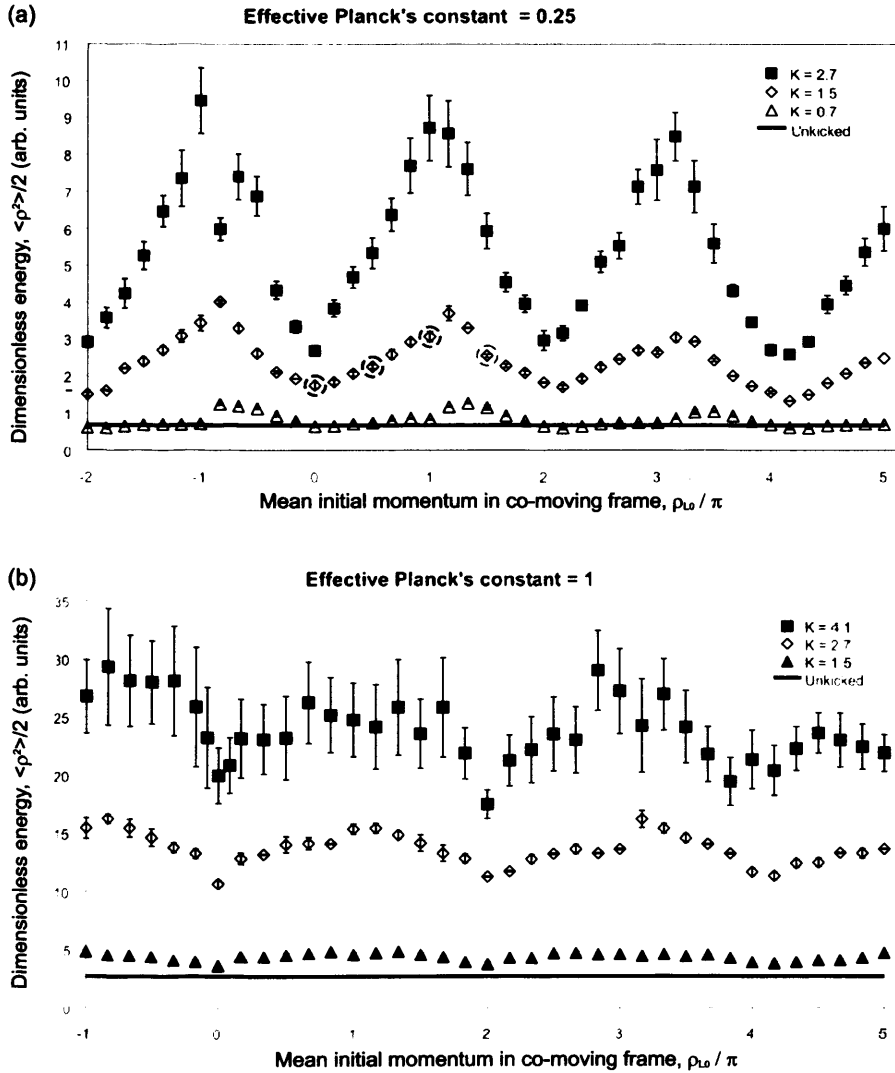
Figure 4.9: The mean atomic energy as a function of initial starting momentum ρ_{L0} for (a) $\hbar_{eff} = 0.25, K = 0.7, 1.5, 2.7$ and (b) $\hbar_{eff} = 1, K = 1.5, 2.7, 4.1$. The magnitude of the energy growth increases as phase space becomes more chaotic (K increases). When the stochasticity parameter is below the critical value ($K = 0.7$ case) the atom remains bounded in momentum space and energy growth is minimal. The circled distributions are shown in detail in figures 4.11 and 4.12.
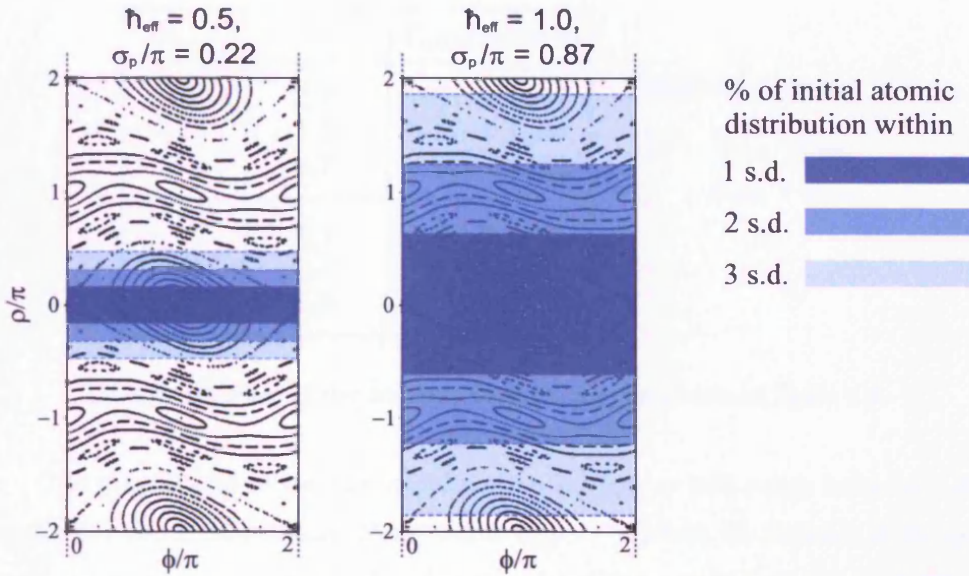
Figure 4.10: The initial atomic distributions for $\hbar_{eff} = 0.25, 1$ superimposed on a phase space portrait of $K = 0.7$. The 1/e width of the distribution $\sigma_p/\pi = 0.22$ when $\hbar_{eff} = 0.25$ and $\sigma_p/\pi = 0.87$ when $\hbar_{eff} = 1$. The shading indicates the percentage of the distribution lying within 1 (darkest), 2 and 3 (lightest blue) standard deviations of $\rho_{L0} = 0$.

unit cell) when $\hbar_{eff} = 1$. Those atoms within ± 1 s.d. of the mean $\rho_L = 0$ (around 68% of the distribution) in the latter case occupy a region greater than the momentum width of the stable island so results taken at small values of $\hbar_{eff}$ are expected to exhibit greater resolution.

The difference in the resolution of stable structures in phase space may be seen by comparing the data for $K = 1.5, 2.7$ for the two values of $\hbar_{eff}$ in figure 4.9. The peaks in atomic energy are very well defined when $\hbar_{eff} = 0.25$ but rather less well when $\hbar_{eff} = 1$. These differences in resolution may be quantified by defining a contrast function, C:

$$C = \frac{E_{max} - E_{min}}{E_{max} + E_{min}} \tag{4.4}$$

where $E_{max,min}$ are the maximum and minimum values of energy $E = \frac{\langle \rho^2 \rangle}{2}$ for a given value of K and effective Planck's constant $\hbar_{eff}$. The results for the parameters investigated in this experiment are given in table 4.1.

h_eff	K	C,contrast fn
0.25	2.7 1.5 0.7	0.57 ± 0.21 0.50 ± 0.04 0.358±0.001
1.0	4.1 2.7 1.5	0.25 ± 0.11 0.21 ± 0.02 0.146±0.001

Contrast function

$$C = \frac{E_{max} - E_{min}}{E_{max} + E_{min}}$$

Table 4.1: Values of the contrast function for the results of figure 4.9.

The magnitudes of the contrast function for $\hbar_{eff} = 0.25$ range between 0.36 and 0.57, much larger than those when $\hbar_{eff} = 1$ which lie between 0.15 and 0.25. Comparing the values of C for $K = 1.5, 2.7$ suggests that the contrast is approximately three times greater when $\hbar_{eff} = 0.25$ than when $\hbar_{eff} = 1$.

The difference in diffusive behaviour caused by centring the atomic distribution on a stable island rather than in chaotic phase space is better illustrated in figure 4.11 for $\hbar_{eff} = 0.25, K = 1.5$. Phase space at this magnitude of K comprises of sizeable stable islands at $\rho/\pi = 0, \pm 2$ surrounded by a chaotic sea (figure 4.8).

When the initial atomic momentum is $\rho_{L0}/\pi = 0$, the majority of atoms are confined by a stable island so there is very little diffusion and the momentum profile is a narrow Gaussian. If instead the distribution is started at $\rho_{L0}/\pi = 1$, in a chaotic region of phase space, the momentum profile is much broader as diffusive growth is possible. These two profiles are circled in dark green and red respectively on figure 4.9, where they correspond to minimal and (almost) maximum energy growth as expected.

The left panel of figure 4.12 portrays the momentum profiles that result from starting the atomic distribution close to a stable structure for the same initial conditions. At $\rho_{L0}/\pi = 0.5$ (dark blue line), the atoms are positioned in chaotic phase space such that the right-hand (more positive momenta) side of the distribution is closer to a stable structure than the left. Recall that
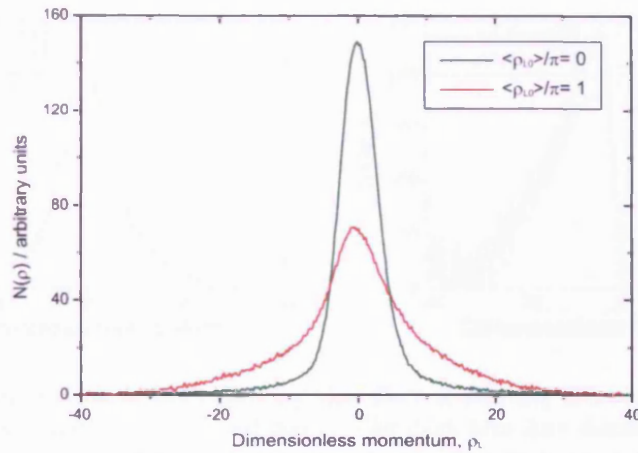
Figure 4.11: Momentum profiles illustrating the difference in momentum growth caused by starting the atomic distribution on a stable island ($\rho_{L0}/\pi = 0$, dark green line), which constrains momentum diffusion, or in chaotic phase space ($\rho_{L0}/\pi = 1$, red line), where energy growth is possible. The points corresponding to these profiles are ringed in these same colours on figure 4.9.

the width of the atomic distribution is $\sigma_p/\pi = 0.22$ so the right edge of the atomic distribution here coincides with the outermost KAM surface of the stable resonance at $\rho_{L0}/\pi = 0$. Diffusion for atoms closest to the island (positive momenta side of the distribution) is highly constrained by KAM tori but atoms initially on the left side of the distribution can diffuse through a much larger area of chaotic phase space. This results in a slightly asymmetric momentum profile, favouring negative momenta.

The situation is reversed when $\rho_{L0}/\pi = 1.5$ (light blue line). The presence of the stable island at $\rho/\pi = 2$ restricts the spread of the rotor wavefunction towards negative momenta in phase space and the resulting momentum profile has the opposing symmetry about $\rho_L = 0$.

The difference between these two distributions is made clearer by the right panel on figure 4.12, where the modulus of the first moment of the momentum distribution $|\rho_L \cdot N(\rho_L)|$ is plotted against atomic momentum. The difference in the area under the peaks of each curve is a measure of the asymmetry in the momentum profile and the two plots are near mirror images of each other. As before, these profiles are circled in the same colours on figure 4.9.
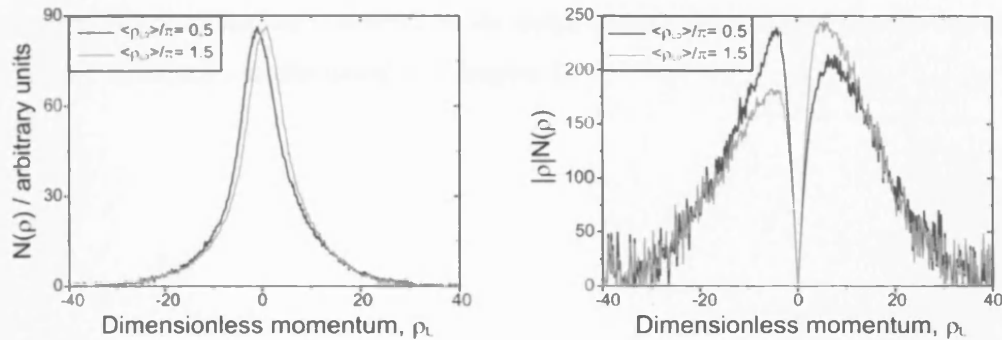
Figure 4.12: Momentum profiles showing the effect of starting the atomic distribution on either side of a stable island. *Left panel:* The dark blue line shows the momentum profile for $\rho_{L0}/\pi = 0.5$ when diffusion towards positive ρ_L is suppressed. The light blue profile is for $\rho_{L0} = 1.5$, when diffusion towards negative ρ_L is constrained. *Right panel:* The opposing asymmetry is more clearly presented by plotting the first moment of the atomic distribution $|\rho|N(\rho)||$. The points corresponding to these profiles are ringed in these same colours on figure 4.9.

In conclusion, this brief investigation has demonstrated the utility of the moving lattice technique in accessing areas of phase space and shown the effect of stable islands on diffusion. We conclude that it is therefore necessary to make $K > 4$ to ensure any asymmetry observed is unrelated to regular islands in phase space. The results of this investigation are presented in [70].

4.5 Summary

This chapter introduced the concept of the momentum boundary, created by approximating delta-kicks with finite-width pulses, that produces a sinc-squared dependence on the initial atomic momentum in the diffusion constant. This modulation was used in conjunction with the moving lattice technique to generate asymmetric diffusion. This technique enables the initial atomic momentum to be changed easily and allows access to areas of phase space that cannot be reached using a stationary potential. Its utility was demonstrated using a simple investigation to map the stable structures in phase space, which can also modify diffusion.

It is therefore important that no significant structures remain in phase space and to avoid the momentum boundary by ensuring that $t_p \ll T$ when observing

asymmetric momentum diffusion in the delta-kicked rotor that is purely due to chaotic dynamics, as discussed in Chapter 5.

CHAPTER 5

Symmetry breaking in the DKR

This chapter introduces two ways in which highly asymmetric momentum diffusion of cold atoms in an optical lattice can be generated in the absence of noise or external driving forces and instead using only chaotic dynamics. Breaking the temporal symmetry of the DKR by employing a two-period pulse sequence makes the kick-to-kick correlation terms in the diffusion constant non-negligible. In particular, diffusion is influenced by the non-zero correlations between next-but-one kicks that introduce a cosinusoidal momentum dependence to the diffusion constant. When coupled with the moving lattice technique to control the initial atomic momentum, this results in a locally asymmetric diffusion constant that can be exploited to produce directed transport.

In the second method, a linear potential gradient of alternating sign is added to the kicking potential to break spatial symmetry such that the atoms experience an additional inertial force in the atomic reference frame. Temporal symmetry is broken by using a two-period kick sequence to satisfy Curie's Principle (that directed motion will result if spatio-temporal symmetry is broken [71]) and achieve directed diffusion.
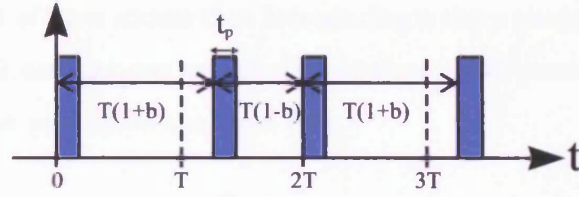
Figure 5.1: The two-period kick sequence with $T_1 = T(1-b)$ and $T_2 = T(1+b)$, where $b \ll 1$ is the chirp parameter.

5.1 Directed motion by breaking temporal symmetry

Deterministic ratchets have been the subject of much scrutiny in recent times [72, 73]. It was long thought that breaking both spatio-temporal symmetry [74] or a mixed phase space [75] was necessary to generate directed diffusion in a 'clean', non-dissipative system. Recent work by Monteiro *et al* [76], however, has proposed an experimentally realisable method of achieving directed diffusion from purely deterministic dynamics that does not rely on stable islands in phase space or engineering an asymmetric potential. The temporal symmetry of the system is broken by a two-period kicking cycle that introduces a cosinusoidal momentum dependence in the diffusion constant which, when used in conjunction with the moving lattice technique, can be be used to generate asymmetric diffusion.

5.1.1 Modifying the diffusion constant

The temporal symmetry of the DKR is broken by introducing a small deviation away from period-one kicks via a chirp parameter b ($b \ll 1$) and using a two-period kicking cycle $T(1-b) : T(1+b)$ instead of regular, single-periodic kicks. This cycle, sketched in figure 5.1, can be written:

$$F(\tau) = \sum_{n=0}^{\infty} \sum_{m=0}^{1} f(\tau - n(T_1 + T_2) - mT_1) \qquad (5.1)$$

such that the kicks occur at $t = T_1, (T_1+T_2), T_1+(T_1+T_2), (T_1+T_2)+(T_1+T_2), ...$ where $T_1 = T(1-b)$ and $T_2 = T(1+b)$.

Jonckheere *et al* have shown that introducing a chirp parameter modifies the next-but-one kick correlations to include a momentum dependence such that the diffusion constant now takes the form [76]:

$$D(K, \rho, b) = \frac{K^2}{2}(1 - 2J_2(K)cos(2\rho b) + ...) \tag{5.2}$$

where $J_2(K)$ is a second order Bessel function and ρ is the atomic momentum. The $2J_2(K)cos(2\rho b)$ term is called the C_2 correction and described correlations between next-but-one kicks.

The diffusion constant is now a cosinusoidal function of the atomic momentum, as represented in figure 5.2 as a function of atomic momentum in the moving lattice frame ρ_L. If the atoms are positioned at $\rho_{L0} = 0$, the diffusion constant is locally symmetric about the mean momentum and atoms diffuse equally far in both directions (left panel).

Asymmetric momentum diffusion can be generated by using the moving lattice technique to change the initial atomic momentum such that the diffusion constant is locally asymmetric (right panel on figure 5.2). The asymmetry in momentum is expected to vary as the derivative $\partial D/\partial \rho_L$. The $cos(2\rho_L b)$ variation of the diffusion constant gives maximal asymmetry when $\rho = (2m - 1)\pi/4b$ and symmetric diffusion when $\rho = m\pi/2b$ (where m is an integer). A modulation of the diffusion constant also results in a modulation of the break time since $D \propto t^*$. This acts to enhance atomic momentum growth when $D(K, \rho, b)$ is large and constrain momentum growth when $D(K, \rho, b)$ is small.

The scaled Hamiltonian of the chirped kick system is given by $\mathcal{H} = \frac{\rho^2}{2} + Kcos\phi F(\tau)$ and a similar analysis to that in Chapter 3 (detailed in [50, 59]) shows that for a two-period kicking cycle the trajectories in phase space are now iterations of the following equations:

$$\rho_{n+1} = \rho_n - Ksin(\phi_n) \tag{5.3}$$

$$\phi_{n+1} = \phi_n + \rho_{n+1}(1 + b(-1)^n) \tag{5.4}$$

where n is the kick number.
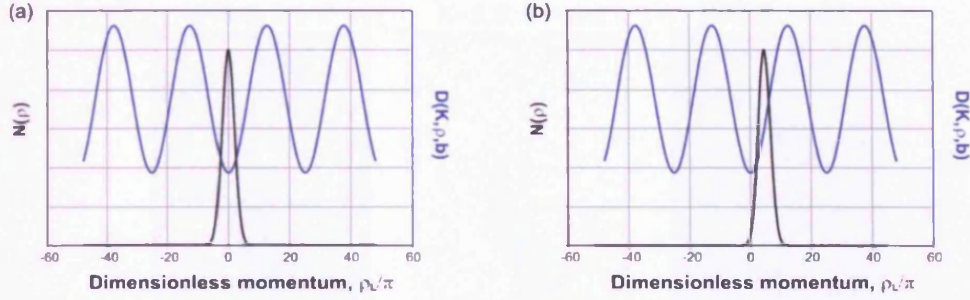
Figure 5.2: The cosinusoidal momentum dependence of the diffusion constant $D(K,\rho,b)$ (blue) and the initial atomic distribution $N(\rho)$ (black) for (a) $\rho_{L0} = 0$ and (b) $\rho_{L0} = 5$.

The position mapping now has an extra b-dependent term when compared with the Standard Map for a regular kick sequence (equation 3.4 in Chapter 3). The effect of this additional parameter is to enlarge the chaotic regions present in phase space for any given value of K, as can be seen in figure 5.3. The left panel of the figure plots the phase space for $K = 3.5$ in the case of regular kicks ($b = 0$) for which regions of regular motion occur at $\rho/\pi = 0, \pm 2$. The middle panel shows the same range of phase space for the same value of K when the chirp parameter $b = 0.2$. Phase space is now significantly more chaotic; cantori still exist at $\rho/\pi = 0$ but the stable islands at $\rho/\pi = \pm 2$ have disappeared completely. Expanding the region of phase space plotted shows the 2π periodicity of the standard map has been replaced by 5π periodicity when $b = 0.2$. This is equivalent to a periodicity of π/b, in agreement with the analytical results of [76, 59].

The difference in the energy growth caused by chirping the kicks can also be observed in the momentum profiles for regular and chirped kick sequences. Figure 5.4 shows the momentum profiles and their corresponding phase space plots for an atomic distribution prepared at $\rho_{L0} = 0$ when $b = 0.2, K = 1.5$ and $\hbar_{eff} = 0.25$. The pulse duration of the kick sequence used was $t_p = 384 \pm 20$ ns and the kick period $T = 2.40 \pm 0.02 \mu$s. The stochasticity parameter $K = 1.5 \pm 0.2$ required the kicking potential to be detuned by approximately -3000Γ and the momentum boundary is located at $\rho_b = 40 \pm 2$.
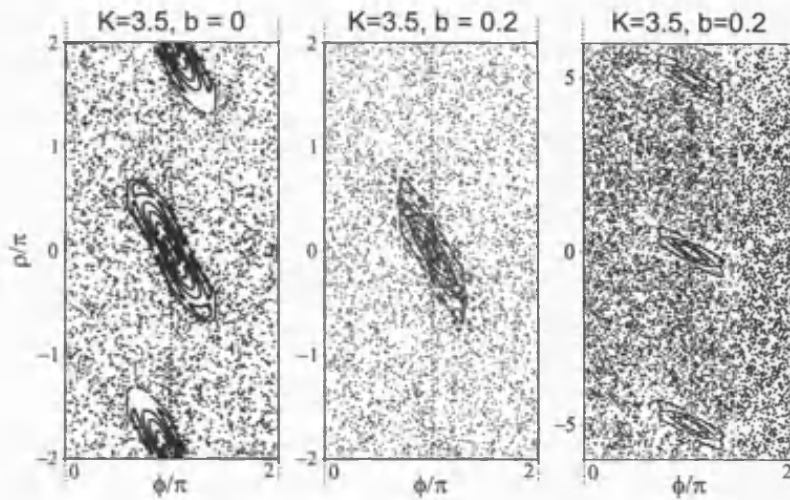
Figure 5.3: The difference in phase space caused by chirping the kick sequence. The left panel plots iterations of the standard map for $K = 3.5, b = 0$ (regular kicks). The middle panel plots the results of equation 5.3 when $b = 0$ for the same value of K. The 2π periodicity has now been replaced by a $\pi/b = 5\pi$ periodicity in momentum (right panel).

When the kick sequence in regular ($b = 0$, blue line) the momentum profile displays only a small deviation from the unkicked distribution (black line). Chirping the kick sequence breaks up a significant fraction of the KAM surfaces restricting atomic motion, allowing a larger fraction of the atomic distribution to diffuse and so broadens the momentum distribution ($b = 0.25$, red line).

The momentum profile of the regular kick sequence (blue line) follows that of the unkicked distribution for small $|\rho|$ but then deviate significantly, suggesting some energy growth is possible for atoms in the wings of the distribution whilst most of the atoms (those located within one s.d. of $\rho = 0$) remain confined by the stable island at $\rho/\pi = 0$. Chirping the kick sequence breaks up most of the KAM surfaces restricting atomic motion so greater momentum growth is possible and the blue line correspondingly deviates from unkicked distribution much earlier (i.e. at much smaller $|\rho|$).

A further caveat to gaining maximal asymmetry is what is called the *ratchet time* in [50]. The name derives from the idealised case of a Hamiltonian ratchet, where dissipative effects can be neglected such that the directed motion is due
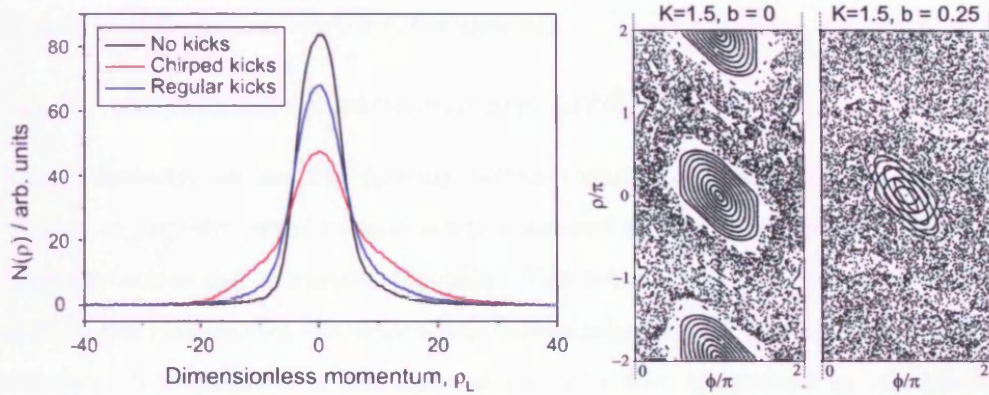
Figure 5.4: Momentum profiles and the corresponding phase space plots for regular kicks ($b = 0$, in red) and chirped kicks ($b = 0.2$, blue) when $K = 1.5$. The black line is the unkicked distribution. The atoms are started at $\rho_{L0} = 0$ in both cases and, as expected, the momentum growth is larger when the kick sequence is chirped.

purely to deterministic mechanics. Like the break time that determines the duration over which the system can absorb energy, the next-but-one kick correction term acts over a finite timescale - the ratchet time t_{rat} - defined as the time taken for the momentum asymmetry to reach 95% of its saturation value. An analytical form for the ratchet time, as derived in [50], is:

$$t_{rat} \propto \frac{1}{Db^2} \qquad (5.5)$$

where $D \equiv D(K, \rho, b)$.

The classical diffusion rates are different for positive and negative momenta over the t_r timescale, D^+ and D^- say [50]. This is the period over which the asymmetry accumulates. Beyond t_r, the rates equalise and the atomic energy growth can once again be described by the quasilinear value, $D^+ \approx D^- \approx D \sim K_{eff}^2/2$.

The clearest experimental signature is predicted when the break time and ratchet time become comparable [76], $t^*/t_r \sim Db/\hbar_{eff} \sim 1$. If the break time is much smaller than t_{rat}, there is little time for the momentum asymmetry to accumulate before the system localises. Beyond the finite lifetime of the C_2 correction t_{rat}, the energy growth continues at the quasilinear rate, which worsens the experimental signal-to-noise ratio of the asymmetry signal and makes the

detection of the asymmetry less favourable.

5.1.2   Asymmetric momentum profiles

Experimentally, we use the moving lattice technique detailed in the previous chapter to vary the initial atomic momentum and thereby vary the local diffusion constant across the momentum profile. The parameters are chosen such that neither the momentum boundary nor stable islands in phase space can affect diffusion. The position of the momentum boundary is checked by calculation (its presence can also be seen in the momentum profiles) and the phase space is carefully examined to ensure no stable structures remain in each case.

For atoms are started at $\rho_{L0} = 0$, the diffusion constant is locally symmetric across the atomic distribution and diffusion is expected to be symmetric (as shown by the left panel in figure 5.2). When the initial atomic momentum is non-zero, the diffusion constant is locally asymmetric and directed diffusion is possible.

Figure 5.6 presents some typical momentum distributions where directed diffusion is evident by the asymmetry in the profiles. In this investigation, the kick sequence has a chirp parameter $b = 1/8$ and the stochasticity parameter $K = 2.1$. The kick period $T = 2.37 \pm 0.02\mu s$ gives an effective Planck's constant of $\hbar_{eff} = 0.25$ and 80 pulses of duration $t_p = 379 \pm 20$ ns ensures that the momentum boundary at $\rho_b = 40 \pm 2$ has no effect on diffusion and that there is enough time for the system to localise.

The phase space plots for these conditions are shown in figure 5.5. Iterating the Standard Map (that is, using a regular kick sequence) for $K = 2.1$ reveals the presence of stable structures occurring with 2π periodicity in momentum (left panel). Chirping the kick sequence, however, breaks these tori up so that no significant barriers remain to influence diffusion when $b = 1/8$ (right panel).

Maximum asymmetry is expected when $\rho_{L0}/\pi = \pm 2$ for $b = 1/8$ following the analysis in section 5.1.1 and indeed it can be seen that the momentum profiles corresponding to these starting momenta are highly asymmetric. When the initial atomic momentum is $\rho_{L0} = +2\pi$ (in red), the momentum profile is
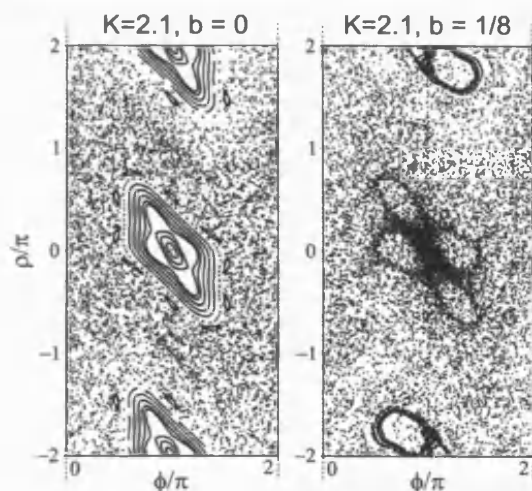
Figure 5.5: Phase space plots for $\hbar_{eff} = 0.25, K = 2.1$ when the chirp parameter $b = 0$ (right) and $b = 1/8$ (left), confirming that the stable islands are replaced by cantori when the kicks are bi-periodic. Any momentum asymmetry should therefore be due to chaotic dynamics alone.

heavily skewed to the right but this trend is reversed for $\rho_{L0} = -2\pi$ where more atoms are pushed to higher momenta on the left side of the profile. This is because the gradient of $D(K, \rho, b)$ across the atomic distribution for $\rho_{L0}/\pi = +2$ varies in opposite sense to that of $\rho_{L0}/\pi = -2$. The variation of the diffusion constant with respect to the atomic distribution is schematically shown on the panels on the right of figure 5.6 for (a) $\rho_{L0}/\pi = +2$ and (b) $\rho_{L0}/\pi = -2$. The distributions corresponding to the maximum gradients are very nearly mirror images of each other with the discrepancies most likely due to a slight misalignment of the kicking beams. The inset shows more clearly the asymmetry in the momentum profile associated with a starting momentum of $\rho_{L0}/\pi = 2$.

5.1.3 Time evolution

The time evolution of the asymmetry of the momentum profiles in figure 5.6 ($b = 1/8$) can be seen in figure 5.7 for several different starting momenta. The evolution is difficult to see by plotting a series of profiles so instead the asymmetry is quantified by the first moment of the atomic distribution, $\langle \rho \rangle = \int \rho N(\rho) \partial \rho / \int N(\rho) \partial \rho$. This is plotted against the number of kicks (in two kick
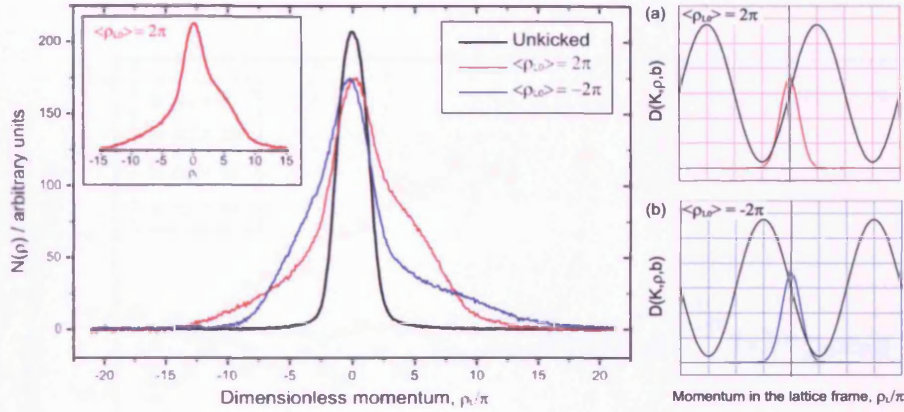
Figure 5.6: Momentum profiles illustrating the difference between starting the atoms at (a) $\rho_{L0} = 2\pi$ (red) and (b) $\rho_{L0} = -2\pi$ (blue) when the kick sequence is chirped by a factor $b = 1/8$. The diffusion constant in locally asymmetric in both cases and the momentum asymmetry that results is skewed in opposite directions, thus reflecting the relative gradients of $D(K, \rho, b)$ experienced by the atoms (pictured on the panels on the right). The symmetric unkicked distribution (black line) is included for comparison. *Inset:* The asymmetry can be clearly seen in the momentum profile for $\rho_{L0} = 2\pi$.

steps) to build up a picture of the time evolution of the asymmetry. The variation of the diffusion constant across the atomic distribution is figuratively represented in panels (a)-(d) on figure 5.7. In all cases, the asymmetry settles to within 10% of its final value after around 60 kicks.

When $\rho_{L0} = +2\pi$ (red line, panel (b)), the atoms are positioned such that they experience the maximum possible gradient of diffusion constant across the distribution. The gradient is positive so results in a positive asymmetry. In the $\rho_{L0} = +6\pi$ (green, panel (c)) instance, the gradient of the diffusion constant across the atomic distribution is of the opposite sign and the resulting asymmetry is negative. No asymmetry is expected when the atoms are started off at $\rho_{L0} = 0, 4\pi$ (black, blue lines respectively) because the diffusion constant is locally symmetric but $\langle \rho \rangle$ is not quite zero in either case. This offset can be attributed to some small asymmetry in the initial atomic distribution resulting from a slight misalignment of the beams comprising the kicking potential. The magnitude of the offset in $\langle \rho \rangle$ for each set of results varies because it is impossible to exactly replicate the starting conditions when setting up each experiment.
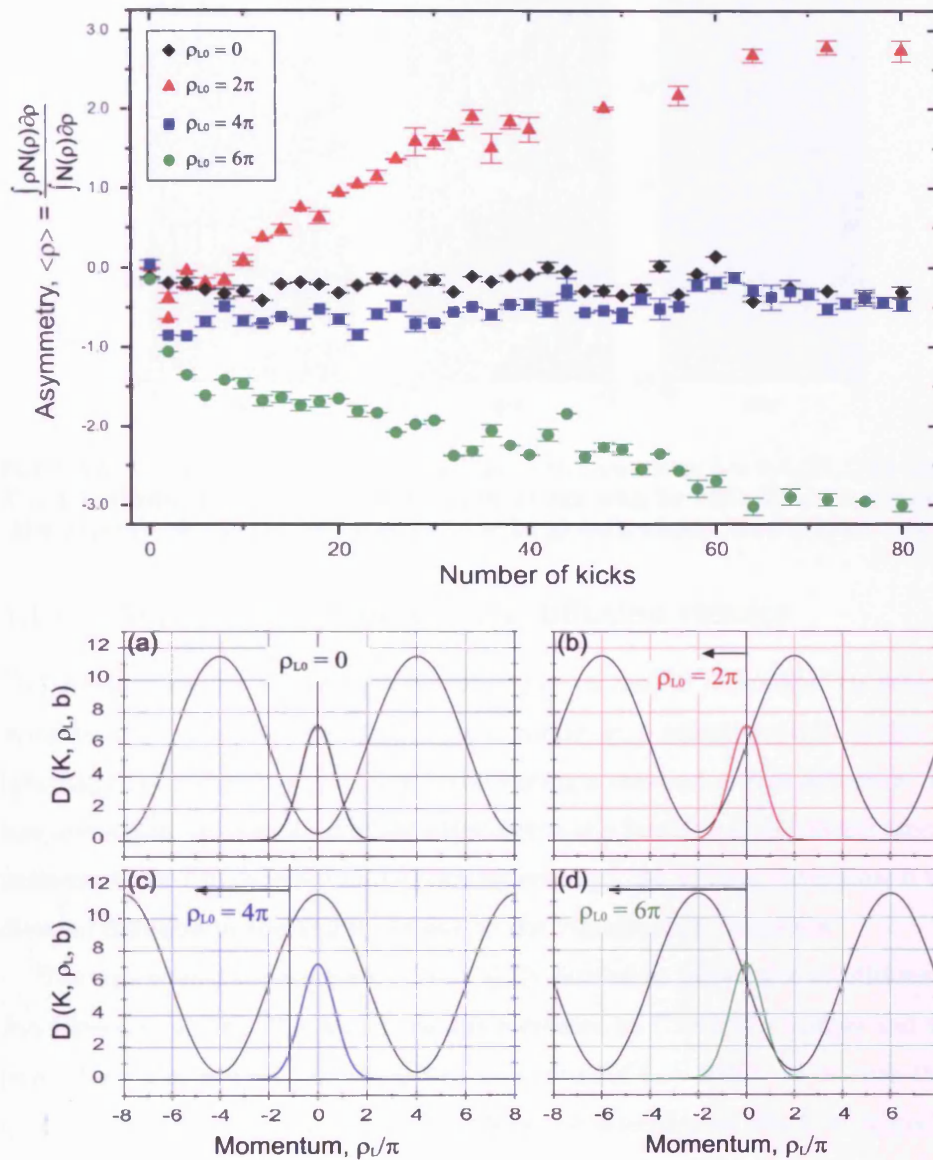
Figure 5.7: Time evolution of the asymmetry $\langle \rho \rangle$ for a chirp parameter $b = 1/8$ when (a) $\rho_{L0} = 0$ (black), (b) $\rho_{L0} = 2\pi$ (red), (c) $\rho_{L0} = 4\pi$ (blue) and (d) $\rho_{L0} = 6\pi$ (green). The position of the atomic distribution (coloured lines) relative to the diffusion constant (black line) are drawn on panels (a)-(d). There is little asymmetry when the diffusion constant is locally symmetric (cases (a) and (c)) but the asymmetry grows with kick number when $D(K, \rho, b)$ is locally asymmetric until it saturates after about 60 kicks (cases (b) and (d)).
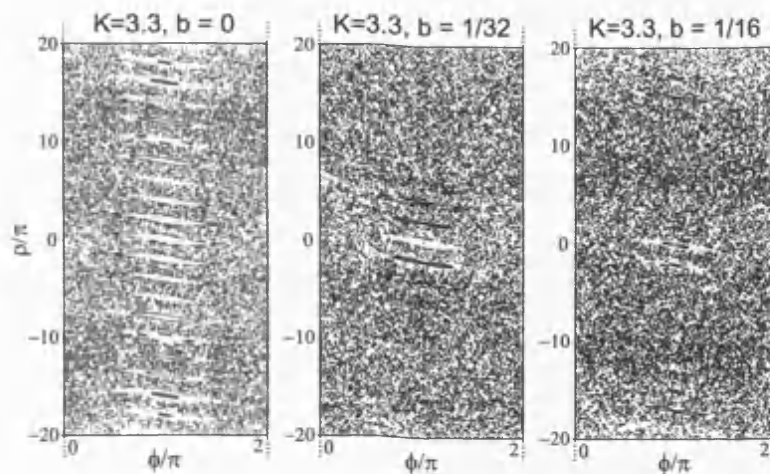
Figure 5.8: Phase space portraits for various chirp parameters $b = 0, 1/32, 1/16$ when $K = 3.3$. Whilst phase space exhibits stable islands with 2π periodicity for a regular kick sequence ($b = 0$), it can be assumed to be globally chaotic for $b = 1/32, 1/16$.

5.1.4 Asymmetric momentum diffusion results

The previous results in this chapter have shown that it is possible to achieve asymmetric momentum diffusion of cold atoms in a pulsed optical lattice by breaking the time symmetry of the system using a two-period kick sequence. We now investigate the variation of the asymmetry as a function of the initial atomic momentum for two different chirp parameters $b = 1/32, 1/16$ to determine if the directed diffusion in the system is due to the Hamiltonian dynamics.

The experimental parameters are slightly altered to match the conditions in Jonckheere *et al* [76]. The kick period is increased to $T = 9.47 \pm 0.02 \mu s$ and the pulses have a measured full-width half maximum of $t_p = 296 \pm 20$ ns such that $t_p/T = 1/32$ and the momentum boundary has a negligible effect on diffusion ($\rho_b = 2\pi T/t_p$). The sequence consists of 160 two-kick cycles, enough to ensure $t > t^*, t_{rat}$. The effective Planck's constant $\hbar_{eff} = 1.0$ and the stochasticity parameter $K = 3.3 \pm 0.3$. Figure 5.8 shows the phase space portraits for these conditions. Stable islands are present in the case of the Standard Map ($b = 0$) but no tori exist to affect diffusion when the kick sequence is chirped.

Figure 5.9 plots our experimental results for the asymmetry as a function
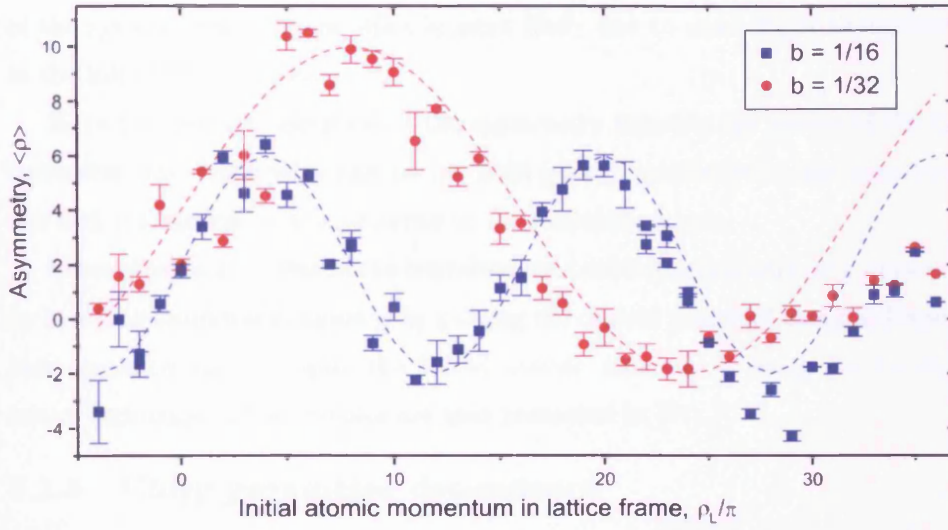
Figure 5.9: The periodic variation of asymmetry $\langle\rho\rangle$ as a function of initial atomic momentum in the moving lattice frame ρ_{L0} for $b = 1/32, 1/16$. The dotted lines are sinusoidal fits to the experimental data with a period π/b.

of the initial atomic momentum in the frame of the moving lattice for $-4 \leq \rho_{L0}/\pi \leq 36$ for two different chirp parameters $b = 1/32$ (in red) and $1/16$ (blue). Dashed lines in identical colours mark functions of the form $f(\rho_{L0}) = A_0 sin(2\pi\rho_{L0}b) + B$, where the coefficients A_0 and B are arbitrarily chosen to fit the experimental data.

The momentum asymmetry oscillates with the predicted period π/b for both sets of data, as confirmed by the sinusoidal fits to the data. These fits are in excellent agreement with the experimental data over a large range of ρ_{L0}, until $\rho_{L0} \approx 30$ in the $b = 1/32$ case and $\rho_{L0} \approx 25$ when $b = 1/16$.

The detuning of the kicking potential is checked every 10 readings but we do not realign the lattice over the atomic cloud so these discrepancies are possibly due to the increased deflection of the first order beam from the acousto-optical modulators controlling the beams that form the lattice. The beams move by $0.1°/$MHz so causes a slight deflection of around $0.03°$ for $\rho_{L0} \approx 30$. A significant deflection (around 1 MHz) will reduce the magnitude of the stochasticity parameter experienced across the atomic distribution and change the dynamics

of the system. The vertical offset is most likely due to some slight asymmetry in the initial distributions.

Since the periodic variation of the asymmetry matches the period of the C_2 correction, the asymmetry can be (at least partly) attributed to the next-but-one kick correlation term and hence to deterministic forces.

In conclusion, it is possible to introduce momentum asymmetry into a system by breaking temporal symmetry by pulsing the optical potential using a chirped kick sequence and changing the initial atomic momentum using the moving lattice technique. These results are also presented in [77].

5.1.5   Chirp parameter dependence

The magnitude of the asymmetry in figure 5.9 is larger when the chirp parameter is smaller ($b = 1/32$). The ratchet time $t_r \propto 1/b^2$ so we can expect a twofold increase in the chirp parameter to result in a factor of four difference in the relative amplitudes as the time over which atoms can accumulate asymmetry quadruples. This would be true if the experimental parameters were adjusted between runs to keep the ratchet time comparable to the break time (which was not the case in this experiment) and the diffusion constant scaled linearly with b. The break time is less than the ratchet time when $b = 1/32$ so the system localised before reaching maximum asymmetry.

With this in mind, we explore the time evolution of the asymmetry for three different values of the chirp parameter $b = 1/8, 1/16, 1/32$. All experimental settings are identical to those used in the previous experiment, detailed in section 5.1.4. The starting atomic momentum is picked to give the maximum possible positive asymmetry, that is to say $D(K, \rho, b) = (2n - 1)\pi/4b$, so is $\rho_{L0} = 2\pi, 4\pi, 8\pi$ for $b = 1/8, 1/16, 1/32$ respectively. The results are presented in figure 5.10.

In all instances the magnitude of the asymmetry increases with time but reaches saturation only for the largest value of b investigated. The rate of the increase depends on b, with the gradient greater for larger values of the chirp parameter. It is possible to estimate the ratchet time when $b = 1/8$ but the
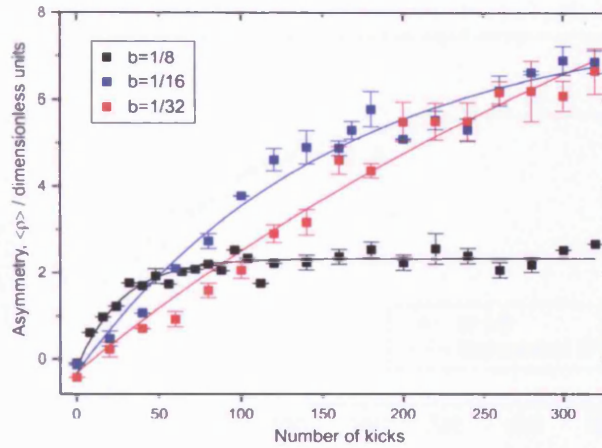
Figure 5.10: The chirp parameter dependence of the asymmetry $\langle \rho \rangle$, here demonstrated by plotting $\langle \rho \rangle$ as a function of the number of kicks for three values of the chirp parameter $b = 1/8, 1/16, 1/32$. The continuous lines are the results of an exponential fit to the data of the form $\langle \rho(t) \rangle = \langle \rho \rangle_{sat}(1 - e^{-t/\beta_r})$.

asymmetry does not saturate within the timescale of the experiment when the chirp parameter is smaller.

The time for which the potential is pulsed cannot be increased because the atoms fall out of the interaction region but an exponential fit to the existing data of the form $\langle \rho(t) \rangle = \langle \rho \rangle_{sat}(1 - e^{-t/\beta_r})$ can be used to give a useful estimate of t_r. The factor β_r is the characteristic time constant of the asymmetry growth and, if the definition of t_r as the time taken to reach 95% saturation value is adopted, is related to the ratchet time by $t_r = \beta_r ln20$. The initial rate of growth of the asymmetry is given by $R_{\langle \rho \rangle} = \frac{d\langle \rho \rangle}{dt}\Big|_{t=0} = \frac{\langle \rho \rangle}{\beta_r}$.

The values of the break time, required for comparison, can be extracted from plots of the atomic energy as a function of the number of kicks, figure 5.11. On a plot of the atomic energy against time, the Standard map break time is measured by the intercept the saturated energy value makes with the classically predicted energy growth $E = Dt$ [50].

A more appropriate method of analysis for the purposes of comparison is to fit the atomic energy growth by a function of identical form to that used in analysing the ratchet time, $E(t) = E_{sat}(1 - e^{-t/\beta^*})$. Here β^* is a characteristic
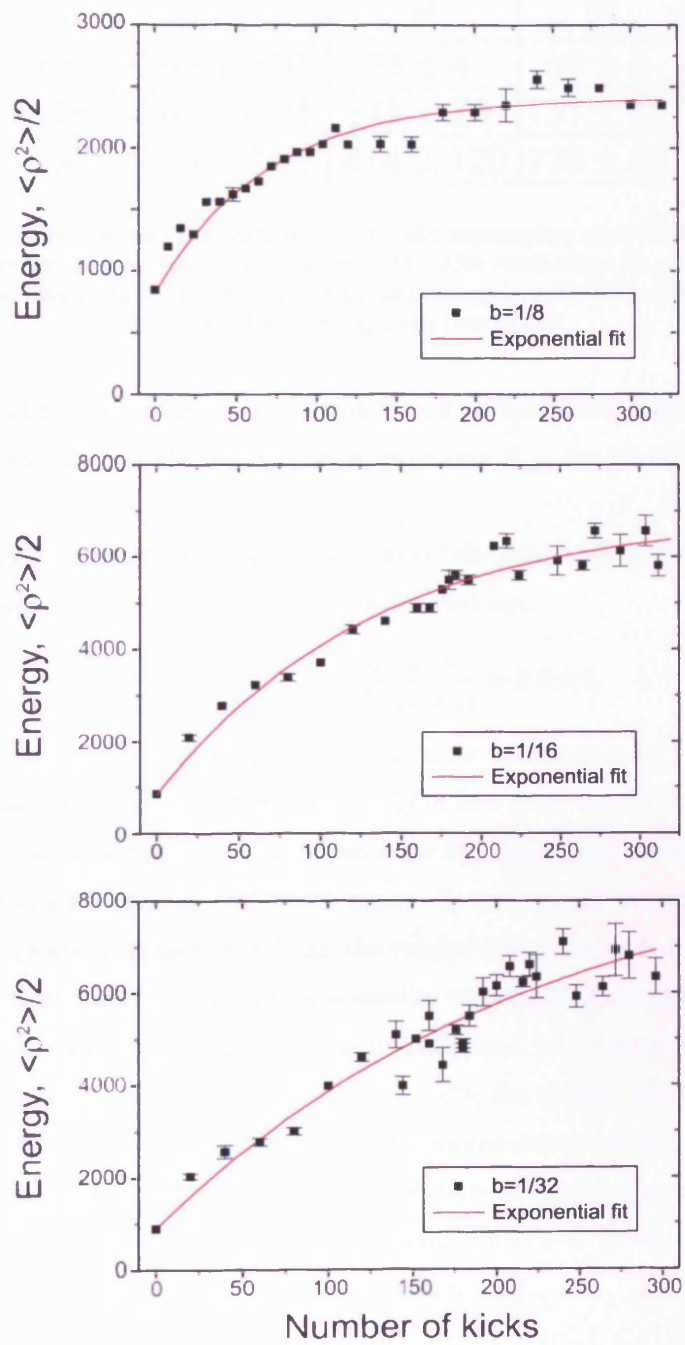
Figure 5.11: Exponential fits to the energy growth when the chirp parameter $b = 1/8, 1/16, 1/32$. The fits are of the form $E(t) = E_{sat}(1 - e^{-t/\beta^*})$, where the characteristic time constant β^* is proportional to the break time.

b	$R_{<\alpha>}$	β_r	β^*
1/8	0.08 ± 0.01	31 ± 4	69 ± 6
1/16	0.06 ± 0.01	145 ± 23	131 ± 15
1/32	0.03 ± 0.01	414 ± 120	220 ± 50

Table 5.1: Results of the exponential fits to the asymmetry growth in figure 5.10 and to the atomic energy growth in figure 5.11. The coefficients β_r and β^* are the characteristic times constants of asymmetry and energy growth respectively and $R_{\langle \rho \rangle}$ describes the initial growth rate of $\langle \rho \rangle$.

time constant that is related to the break time t^*. The characteristic timescales β_r, β^* and estimates of the asymmetry growth rate $R_{\langle \rho \rangle}$ are tabulated in figure 5.1.

In addition to quantifying the growth rate of the initial asymmetry, this data allows a rough check of equation 5.5 to be carried out:

$$\frac{t_{r(b=1/16)}}{t_{r(b=1/8)}} = 4.7 \pm 1, \frac{t_{r(b=1/32)}}{t_{r(b=1/16)}} = 2.9 \pm 1 \tag{5.6}$$

The inverse-squared relationship between t_r and b in equation 5.5 holds (within experimental errors) for $b = 1/8$ and $b = 1/16$ but does not for $t_{r(b=1/16)}$ and $t_{r(b=1/32)}$. The poor fit may be accounted for by comparing the characteristic times constants for ratchet and break times. In the case of the smallest chirp parameter investigated here, $b = 1/32$, the ratchet time is exceeded by the break time and the asymmetry saturates at a smaller value than it should because the system localises before the maximum asymmetry can be accumulated.

The converse is true for $b = 1/8$ (i.e. $t_r < t^*$); the system has become fully asymmetric but the signal-to-noise ratio of the momentum profiles is degraded as the there has not been enough time for maximum atomic energy growth. The break time and ratchet time are matched only when $b = 1/16$, the optimum conditions for observing asymmetry according to [76].

5.2 Directed motion by breaking spatiotemporal symmetry

In this section, we describe a method of generating directed diffusion that is based on a 'rocking ratchet', a much studied model for directed motion that is described in greater detail in Chapter 7. The general requirement for a rocking ratchet is a periodic external force of zero mean that breaks the spatial symmetry of the system [71]. We do this by the addition of a linear potential gradient A that alternates sign with successive kicks. The total potential can now be written:

$$V(\phi) = K cos\phi + A\phi(-1)^n \qquad (5.7)$$

Recall that ϕ is the scaled position and n labels the number of kicks. Combining this new potential with the chirped kick sequence yields the following Hamiltonian for the system (in scaled units):

$$\mathcal{H} = \frac{\rho^2}{2} + [K cos\phi + A\phi(-1)^n]F(\tau) \qquad (5.8)$$

where $F(\tau)$, as defined in equation 5.1, describes a two-period kick sequence $T(1-b) : T(1+b)$.

Deriving the equations of motion from equation 5.8 and following the steps described in Chapter 3, we find that the phase space mapping now depends on three parameters K, A and b:

$$\rho_{n+1} = \rho_n + K sin(\phi_{n+1}) + A(-1)^n \qquad (5.9)$$

$$\phi_{n+1} = \phi_n + \rho_n(1 + b(-1)^n) \qquad (5.10)$$

The introduction of the linear potential gradient also modifies the C_2 correction term such that the diffusion constant is now described by:

$$D(K, \rho, b, A) = \frac{K^2}{2}[1 - 2J_2(K)cos(2\rho b - A) + ...] \qquad (5.11)$$

The diffusion constant varies cosinusoidally with atomic momentum and has a period of π/b once more so the asymmetry oscillates with the gradient of $D(K, \rho, b, A)$ [76]. The potential gradient A acts as a phase shift, enabling the diffusion constant to be made locally asymmetric with respect to the initial atomic distribution by changing the magnitude of A. The asymmetry in momentum is therefore also expected to display a cosinusoidal dependence on A, with the positions of maximum asymmetry occurring when $A = (2m - 1)\pi/4$ and minima when A is an integer m multiple of π.

5.2.1 Accelerating the lattice

The moving lattice experimental apparatus requires only a slight adjustment to incorporate a linear potential gradient. Previously, applying a frequency difference $2\Delta f$ between the two beams overlapped to form the kicking potential caused the interference pattern formed by these two beams to move at a constant speed $\lambda \Delta f$.

Varying the frequency difference to one lattice beam $\Delta f(t)$ with time causes the lattice to accelerate by $a = \frac{\lambda}{2} \frac{d\Delta f(t)}{dt}$. This is equivalent to subjecting the atoms to an inertial force in the reference frame of the moving lattice. The Hamiltonian describing this system may be written:

$$H = \frac{p^2}{2M} + V_0 cos(2k_L x) + Max \qquad (5.12)$$

where x and p are variables in the accelerating frame.

The above equation is identical to equation 5.8 when converted into scaled units, with the explicit form of the potential gradient now given by $A = 2k_L a T t_p$. Linearly ramping $\Delta f(t)$ by an amount ν over one kick period T corresponds to a linear acceleration of $a = \lambda \nu/2T$ and therefore a linear potential gradient of $A = 2\pi \nu t_p$. Such a frequency ramp superimposed on a chirped kick sequence is sketched in figure 5.12. The sign of A can be changed by accelerating the lattice in the opposite direction. Frequency chirping the lattice is experimentally achieved by modulating the output of one rf synthesizer by a sawtooth function
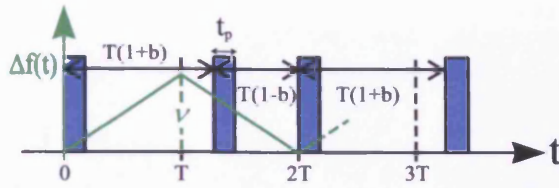
Figure 5.12: Atoms can be subjected to a linear potential gradient by introducing a time-varying frequency to accelerate the kicking potential. Linearly ramping the frequency of one lattice beam by an amount ν in time T results in a potential gradient $A = 2\pi\nu t_p$. A two-period kick sequence with $T_1 = T(1-b)$ and $T_2 = T(1+b)$ ($b << 1$) is used to break temporal symmetry.

derived from an arbitrary waveform generator.

The atoms are laser cooled to about 6 μK (corresponding to a dimensionless rms momentum width $= 2.8 \pm 0.1$ when $\hbar_{eff} = 1$) and centred at $\rho_{L0} = 0$ in this series of experiments. The diffusion constant is made locally asymmetric by changing a via the magnitude of ν. This is easily accomplished using the rf synthesizer control panel. The kick sequence has a chirp parameter $b = 1/16$ and is composed of pulses of duration $t_p = 296 \pm 20$ ns and period $T = 9.47 \pm 0.02\mu$s and where care has been taken to ensure the momentum boundary $\rho_b/\pi = 64 \pm 4$ has a negligible effect on atomic momentum diffusion.

The effective Planck's constant of the system is $\hbar_{eff} = 1$ and the stochasticity parameter is chosen to be $K = 2.6 \pm 0.3$. That phase space is sufficiently globally chaotic at this value is verified by the phase space portraits in figure 5.13. Stable islands occur at a periodicity of 2π when the kick sequence is unchirped but very few cantori remain when $b = 1/16$ to affect diffusion.

Figure 5.14 illustrates the effect of varying the sign and magnitude of the potential gradient. In the absence of a potential gradient, $A = 0$ (black), the diffusion constant is locally symmetric and there is no asymmetry visible in the atomic profile. The variation of $D(K, \rho, b, A)$ becomes asymmetric across the momentum profile when A is non-zero, with the gradient of the diffusion constant varying in opposing senses for $A = +\pi/2$ (red) and $A = -\pi/2$ (blue). Maximum asymmetry is expected at these momenta and accordingly the atomic distribution is skewed towards negative momenta when $A = \pi/2$ in contrast to
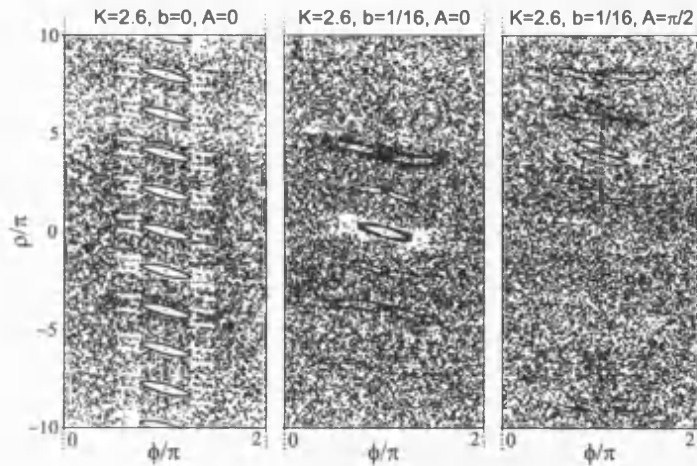
Figure 5.13: Phase space portraits for the conditions used in the accelerated-lattice experiments $K = 2.6, b = 1/16$. Stable islands are present at a periodicity 2π when the kick sequence is regular but only cantori are present (at an altered periodicity of π/b) when the sequence is chirped by a factor $b = 1/16$. When the linear potential gradient $A = \pi/2$, the remaining cantori are shifted by $+4\pi$ along the momentum axis.

greater energy growth for positive momenta when $A = -\pi/2$.

This difference can be examined in greater detail by plotting the first moment of the momentum distribution $|\rho| \cdot N(\rho)$. The magnitude of the asymmetry in the two cases $A = \pm\pi/2$ is (almost) equal and opposite, reflecting the relative values of $\partial D/\partial \rho$ experienced by the atoms.

Results of an experiment to determine the variation of the asymmetry as a function of the potential gradient for $K = 2.6, b = 1/16$ are presented in figure 5.16. Once again the asymmetry $\langle\rho\rangle$ is quantified by the first moment of the distribution. It is expected to oscillate with a period π/b but the rf synthesizer only allows a maximum $\nu = \pm1.25$ MHz, which limits the largest potential gradient it is possible to achieve to $A = \pm3\pi/4$. The range of A investigated is therefore extended using the moving lattice technique to cool the atoms down to $\rho_{L0} = 8\pi$. Overlapping two sets of data, taken with the atomic distribution centred on $\rho_{L0} = 0$ (black dots) and $\rho_{L0} = +8\pi$ (red dots), allows the modulation of $\langle\rho\rangle$ to be investigated over slightly more than one period. The blue line is an Excel fit to the data of the form $f(\rho) = 1 + 3.5sin(2\rho b - A)$.
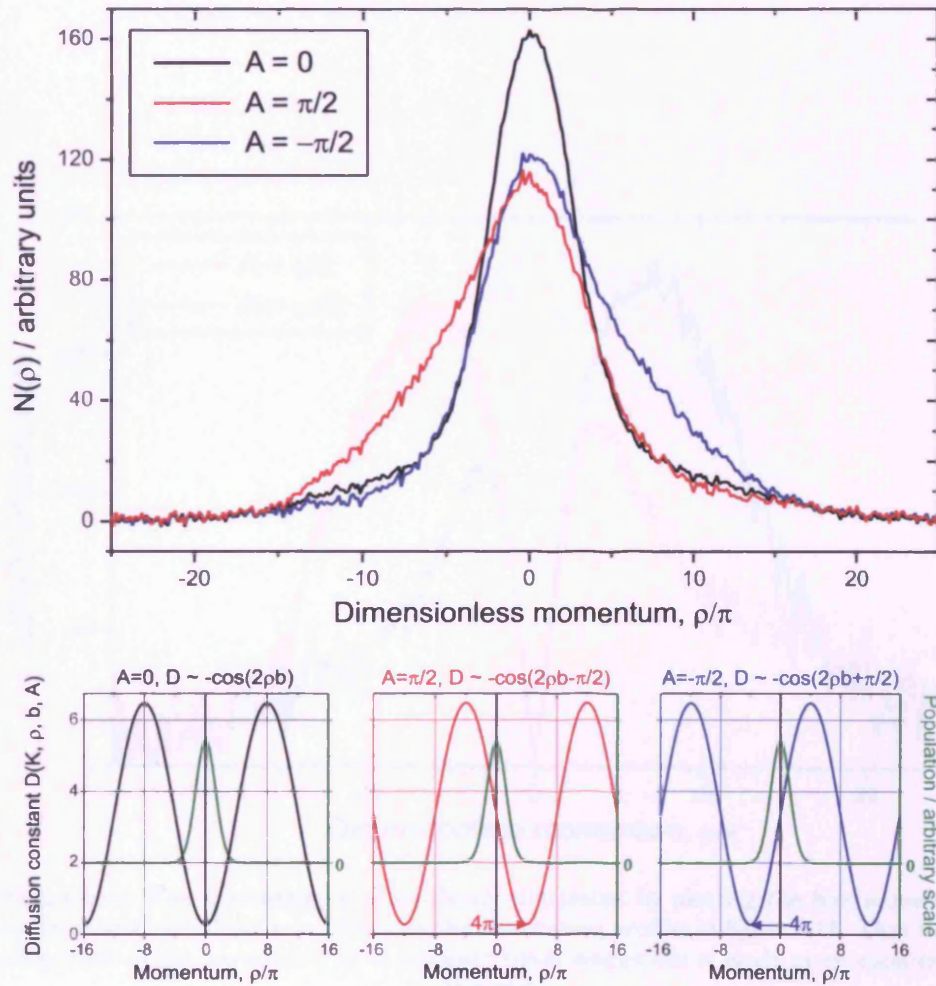
Figure 5.14: The effect of imposing a linear potential gradient A that alternates sign with the kick number on atomic diffusion for $K = 2.6, b = 1/16$. The applied potential gradients are of opposite sign and correspondingly the momentum profile is heavily skewed towards negative momenta when $A = \pi/2$ (red) and towards positive momenta when $A = -\pi/2$ (blue). Diffusion is symmetric in the absence of a potential gradient (black).
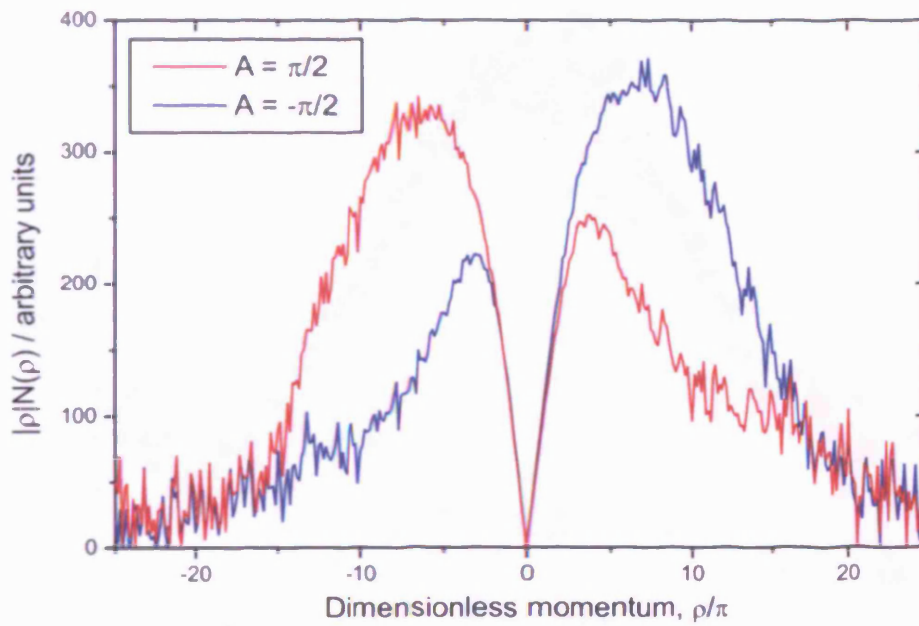
Figure 5.15: The asymmetry is more clearly illustrated by plotting the first moment of the atomic distribution $|\rho.|\, N(\rho)$ for the momentum profiles in figure 5.14. That the magnitude of the asymmetry is of (almost) equal magnitude is made more apparent by this plot.
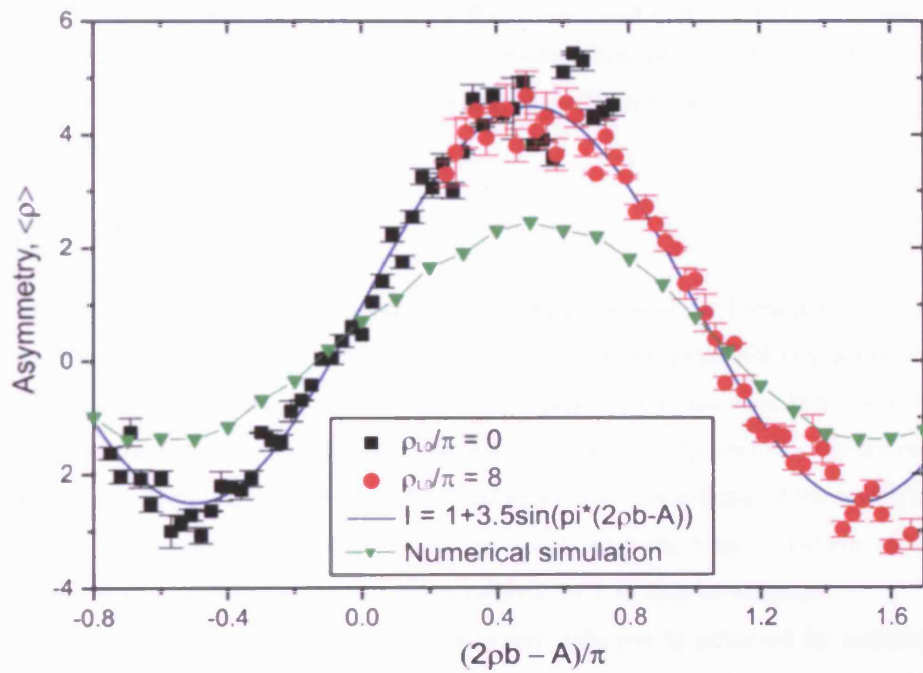
Figure 5.16: The variation of the momentum asymmetry $\langle\rho\rangle$ as a function of the applied linear potential gradient for $K = 2.6, b = 1/16$. The results of two experiments, the first where the initial atomic momentum $\rho_{L0} = 0$ (black) and second where $\rho_{L0} = 8\pi$ (red), are combined to map the oscillation of $\langle\rho\rangle$ over slightly more than one period. The numerical simulation (green) is courtesy of Monteiro et al.

From the results, it is clear that the extra term A in the C_2 correction due to incorporating a linear potential gradient in the system behaves like a phase shift in the diffusion constant. Maximum asymmetry is found when $A = \pi/2$. A numerical simulation (in green, courtesy of Monteiro *et al*) agrees well with the 2π periodicity of the data but not in magnitude. The discrepancy in the size of A is most likely due to the assumptions made in the simulation that are not borne out experimentally. For instance, the simulation assumes a Gaussian distribution that is very narrow in both momentum and space but the actual momentum distribution is slightly wider and the spatial distribution is very much broader by comparison.

5.3 Summary

In this chapter, asymmetric diffusion is first generated by breaking the temporal symmetry in a spatially symmetric system using a chirped kick sequence. This introduces a cosinusoidal momentum dependence in the next-but-one kicks correlation term in the diffusion constant that can be exploited by the moving lattice technique to produce directed diffusion. The periodicity of the variation of the asymmetry is shown to be as expected, and the time evolution of the asymmetry as a function of the chirp parameter b is also investigated.

A second method of generating directed diffusion is achieved by breaking spatio-temporal symmetry in the accelerating frame of the system. Accelerating the kicking potential breaks spatial symmetry and is equivalent to the addition of an inertial term in the system Hamiltonian. This modifies C_2 correction in the diffusion constant once again (it now depends on A) and leads to asymmetric diffusion when coupled with a chirped sequence that breaks temporal symmetry.

The double delta-kicked rotor

The subject of the previous chapter was the generation of asymmetric momentum diffusion by breaking temporal symmetry in spatially symmetric and asymmetric systems. The mechanism responsible in both cases was the introduction of a chirp parameter b in the kick sequence. This made the term describing correlations between next-but-one kicks in the diffusion constant momentum dependent, which was exploited using the moving lattice technique to produce a momentum asymmetry in the system that varied with a period π/b.

New corrections to the diffusion constant appear when b is so large that the kick sequence more closely resembles a 'double' kick sequence, a sequence composed of pairs of pulses occurring at regular intervals. Correlations between these kick pairs (i.e. between previously uncorrelated nearest neighbour kicks) and corrections coupling families of kicks lead to a modulation of the diffusion constant (hence energy growth) that can be used to exploited to generate directed diffusion.

6.1 Double kicks

The consequences of approximating delta-kicks by finite width pulses has been investigated in [64, 67] and was also the topic of Chapter 3. The use of non-zero width pulses produces a modulation proportional to its Fourier transform in the

stochasticity parameter $K = \frac{V_0}{\hbar}\hbar_{eff}t_p$ and hence a sinc-squared oscillation in the diffusion constant $D \propto K^2/4$ that is reminiscent of the single slit envelope in diffraction experiments.

Continuing this analogy, a kick sequence that consists of pairs of closely spaced kicks ('double kicks') should hypothetically result in a modulation of K similar to the interference pattern seen in a Young's double slits experiment, i.e the convolution of the sinc function that is the FT of a square pulse and the cosine variation that is the FT of a comb function produces a fast modulation of the diffusion constant as sketched in figure 6.1. We therefore expect to observe a fast modulation of $D(K)$ corresponding to the $\cos^2$ fringes in the optical analogue.

A double kicks sequence with pulses of width t_p separated by t_s and an interval T between successive kick pairs is pictured in figure 6.2.

The presence of two distinct periods in the kick sequence modifies the Standard Map such that the trajectories in phase space are now described by two sets of coupled equations:

$$\phi_{n+1} = \phi_n + \rho_n T \tag{6.1}$$

$$\rho_{n+1} = \rho_n + K\sin\phi_{n+1} \tag{6.2}$$

$$\phi_{n+2} = \phi_{n+1} + \rho_{n+1}\epsilon \tag{6.3}$$

$$\rho_{n+2} = \rho_{n+1} + K\sin\phi_{n+2} \tag{6.4}$$

where $\epsilon = t_s/T$. An example phase space portrait for $K = 3.3, \epsilon = 0.1$ is presented in figure 6.4.

Unlike the Standard Map case, the double-DKR phase space is distinctly stratified due to correlations between nearest neighbour kicks. These strata or 'momentum trapping regions' coincide with trajectories with starting conditions $\rho\epsilon = (2n + 1)\pi$ for which the effect of one kick is cancelled by the following kick. This corresponds to an atom travelling half a lattice period $\Lambda = \lambda/2$ during t_s such that the total kick strength (which must be averaged over one period)
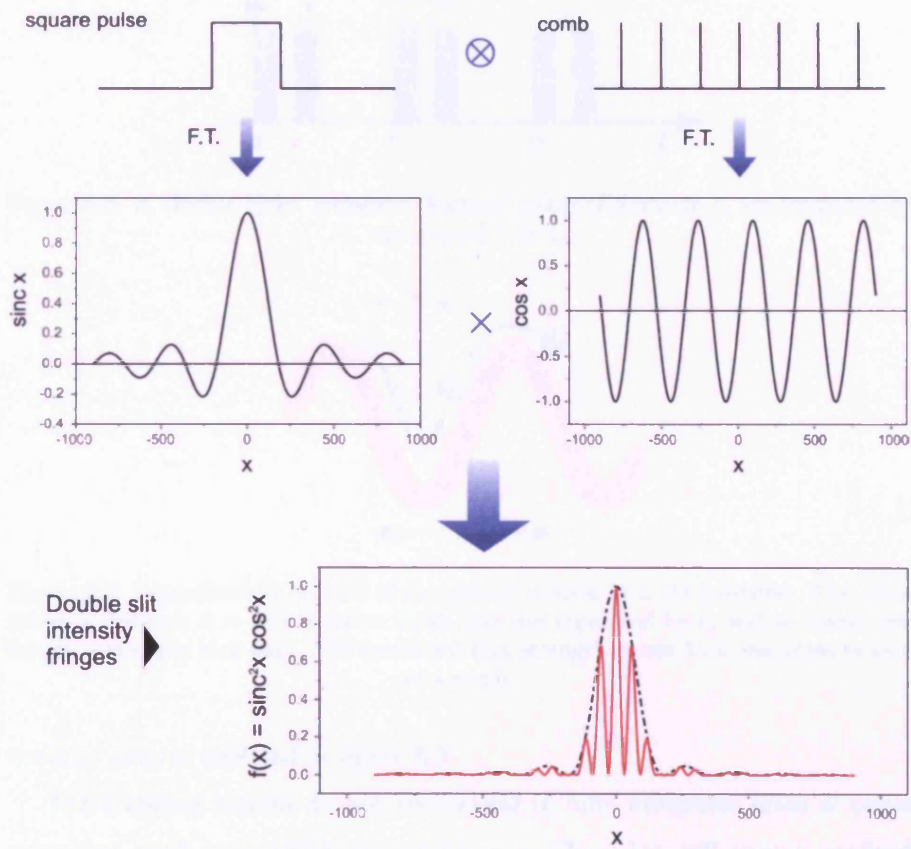
Figure 6.1: The modulation of K is related to the Fourier transform of the pulse shape so a modulation of the energy $D \propto K^2$ is expected to recall the interference pattern of a double slits experiment.
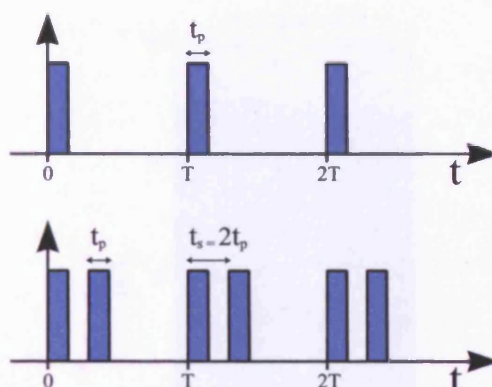
Figure 6.2: A 'double kicks' sequence. Pairs of pulses of duration t_p are separated by t_s and period $T \gg t_s$.
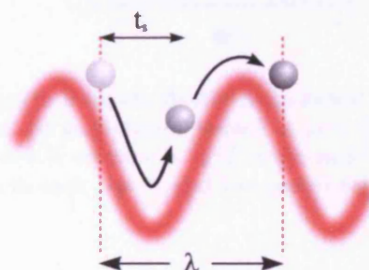
Figure 6.3: Semi-classical picture of the atomic motion in a 1D potential. The atom moves a distance $\Lambda = \lambda/2$ between kicks that are separated by t_s and so covers one lattice period per kick pair. The combined kick strength of one kick pair sums to zero as a result.

sums to zero, as depicted in figure 6.3.

The trapping regions do not correspond to fully integrable areas of phase space but most trajectories started at $\rho\epsilon = (2n + 1)\pi$ will remain confined within them. Conversely, enhanced energy growth is expected for trajectories with initial conditions $\rho\epsilon = 2n\pi$ (where the effect of one kick is reinforced by the following kick) and intermediate behaviour is expected for all other starting conditions.

In Chapter 5 we saw that breaking the temporal symmetry of the system by using a bi-periodic sequence with a chirp parameter b (such that $T(1 - b)$: $T(1 + b)$) introduces a momentum dependence to the diffusion constant:
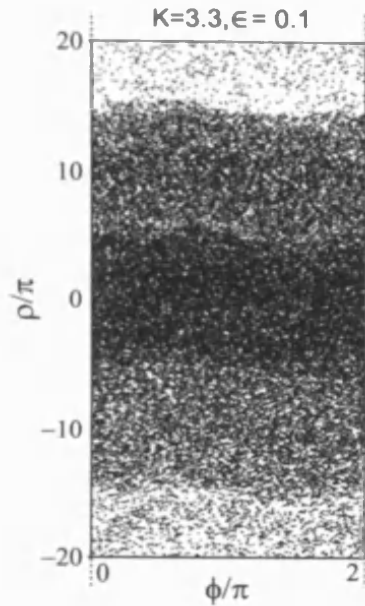
Figure 6.4: Phase space portrait for the double delta-kicked rotor, illustrating the 'momentum trapping regions' for trajectories started at $\rho\epsilon = (2n + 1)\pi$. The parameters here are $K = 3.3$ and $\epsilon = 0.1$, where $\epsilon = t_s/T$ is the ratio between the time interval between the kicks in each pair t_s and the period between kick pairs T.

$$D(K, \rho, b) \cong K^2[\frac{1}{2} - J_2(K)cos(2\rho b) + ...].$$

$$(6.5)$$

The second term in equation 6.5 is the C_2 correction that describes correlations between next-but-one kicks $C_2(K, \rho, b) = J_2(K)cos(2\rho b)$. The C_2 correlations dominate diffusion over the typically short timescale t_r and the momentum asymmetry oscillates as a function of the initial atomic momentum with a period π/b, as confirmed by experiment in Chapter 5.

A double kicks sequence could naively be considered to be an extreme case of the above (a normal kick sequence with a very large value of b), but [78] reports that an analysis of momentum diffusion only in terms of the $C_2(K, \rho, b)$ correction is unsuccessful at describing the experimental results. Instead, three completely new correction terms appear when a double kick sequence is introduced: the C_1 correction couples nearest neighbour kicks whilst the other terms (C_{G1} and C_P) describe correlations between families of kicks.

The C_1 correction term describes the correlations between nearest neighbour kicks m and $m+1$, $C_1 = \langle K^2 sin\phi_m sin\phi_{m+1}\rangle$, where m labels the kick number. In the contrast to all previous experiments described in this thesis (where nearest neighbour kicks were uncorrelated), the C_1 correction is non-zero for the double delta-kicked rotor. Jones *et al* [78] have shown that this correction is $C_1 \propto cos(\rho\epsilon)$ and acts over the shortest timescale (when compared with the other corrections) $t_{C1} \sim 10/(K\epsilon)^2$. For short times, therefore, the atomic energy growth can be written:

$$E \cong \frac{K^2}{4}[1 + cos(\rho\epsilon)]t \qquad (6.6)$$

The energy growth is minimal when $\rho\epsilon = \pm(2n + 1)\pi$ and largest when $\rho\epsilon = \pm 2n\pi$ for $n = 0, 1, 2, \ldots$.

The C_{G1}-correction term acts to couple the second kick in a kick pair with *all* the kicks preceding it. This correction can be shown to be the sum of the correlations between the second kick in a pair (labelled kick j) and all the kicks m before it, $\sum_{m=0}^{j-1} \langle K^2 sin\phi_m sin\phi_j\rangle$ where $m < j$. The individual terms in the summation are very weak when compared with the C_1 correction but they accumulate over time to make the C_{G1} correction dominant at the longest timescales. Jones *et al* [78] have shown that this correction takes the form:

$$C_{G1} \propto -cos(\rho\epsilon) \qquad (6.7)$$

with the same period of oscillation as the C_1 correction but the opposite sign.

The C_{G1} correction therefore acts to make energy minima observed when the C_1 correction dominates into energy maxima at longer times, which may be thought counter-intuitive when the phase space structure is considered. The positions of the energy minima seen initially correspond to momentum trapping regions where no diffusion is expected. When the C_{G1} correction dominates, therefore, maximal atomic energy growth corresponds to the majority of trajectories escaping trapping regions. A Floquet state analysis of the effect of subjecting the atoms to a double kick sequence can be seen found in [79].

On intermediate timescales, when $|C_{G1}| \sim |C_1|$ (so partially cancel each other out), the effects of the third type of correction C_P may be observed. This correction results from a series of n cosinusoidal terms $C_{P_n} \propto K^2 cos(n\rho\epsilon)$ that sums to produce behaviour reminiscent of a Poisson sum formula $\sum_n cos(n\rho\epsilon) = \sum_n \delta[\rho\epsilon - (2n+1)\pi]$. For this reason, the $C_P = \sum C_{P_n}$ correction is called the 'Poisson term'. It results in inverted peaks in the energy maxima when $\rho\epsilon = (2n+1)\pi$, corresponding to the positions of stable islands in phase space, but the physical mechanism responsible for this behaviour is as yet unknown.

A detailed analysis of these new corrections may be found in [80].

6.2 Results

We begin our exploration of the double-DKR by investigating the transition from DKR (single kicks) dynamics to double-DKR dynamics by performing an investigation in which the chirp parameter is increased until the single kicks sequence begins to resemble the double kicks case. The results are presented in figure 6.5.

In this experiment, the Cs atoms are first cooled and trapped in our MOT then further cooled to about 6 μK in an optical molasses. The trap/molasses beams are then turned off and the far detuned lattice beams switched on. No frequency difference is introduced between the lattice beams so that the atomic distribution is prepared at $\rho_{L0} = 0$ for all values of b.

The lattice beams are detuned by approximately -2000Γ to give a potential depth of $V_0/\hbar = 18$ MHz and a stochasticity parameter of $K = 1.7 \pm 0.2$. The effective Planck's constant is $\hbar_{eff} = 0.25$ and the potential is pulsed 160 times (i.e. 160 kicks) in each experimental cycle.

All the kick sequences used are of the form $T(1 + b) : T(1 - b)$ and have the same pulse width ($t_p = 379$ns) and period ($T = 2.37\mu$s) but different chirp parameters: $b = 0$, 0.06, 0.24. The parameter ϵ, used to characterise double kicks sequence, is related to the chirp parameter by $\epsilon = (1 - b)/(1 + b)$. Figure 6.6 presents the phase space diagrams relevant to this experiment.
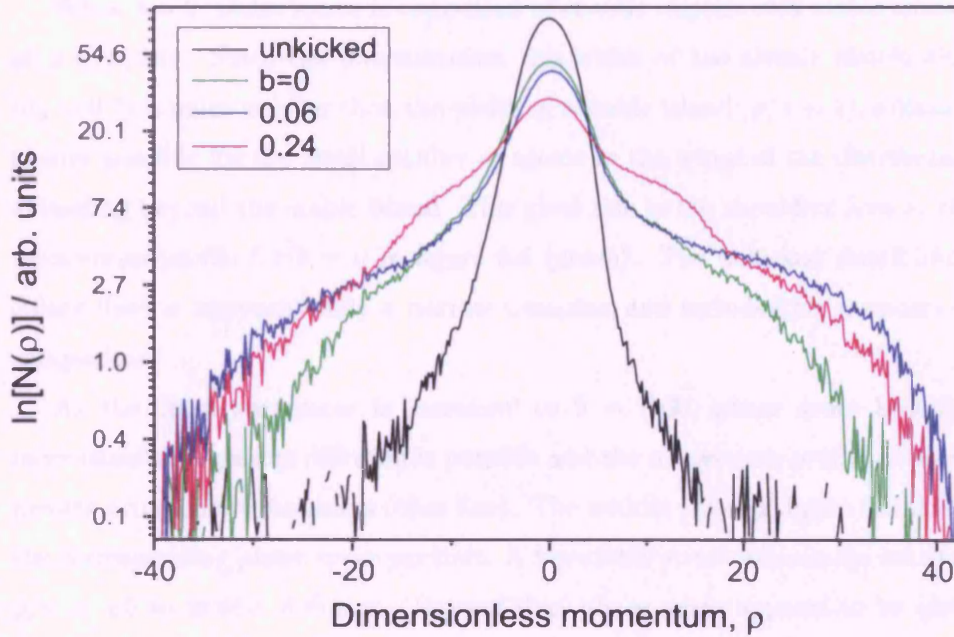
Figure 6.5: The effect increasing the chirp parameter b has on a momentum profile. When $b = 0.24$, the kick sequence closely resembles a double kicks sequence with
$$\epsilon = (1 - b)/(1 + b) = 0.61.$$
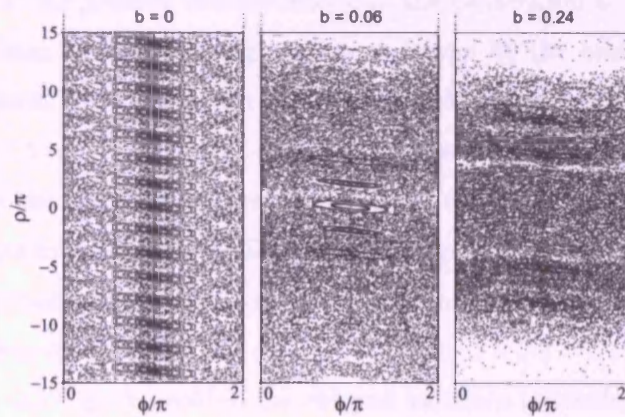
Figure 6.6: Poincaré Surfaces of Section for $K = 1.7$ and various chirp parameters $b = 0, 0.06, 0.24$. *Left panel:* Stable islands occur with 2π periodicity. *Middle panel:* Phase space is more chaotic but small stable islands remain between $\rho/\pi = \pm5$. *Right panel:* Momentum trapping regions are expected at $\rho/\pi = \pm1.6, 4.9, 8.2, 11.5$ when $b = 0.24$. The first trapping region cannot be seen but the second region is clearly marked by a white line stretching parallel to the position axis. The third region is less well marked and very few trajectories appear beyond $\rho \approx 12$, which roughly coincides with the fourth trapping region.

When $b = 0$, phase space is comprised of chaotic regions with stable islands at $\rho = 0, 2n\pi$. Since the dimensionless rms width of the atomic distribution ($\sigma_p = 0.7$) is much smaller than the width of a stable island ($\rho/\pi \sim 1$), diffusion is only possible for the small number of atoms in the wings of the distribution extending beyond the stable island. This gives rise to the shoulders seen in the momentum profile for $b = 0$ in figure 6.5 (green). The unkicked distribution (black line) is approximately a narrow Gaussian and included for purposes of comparison.

As the chirp parameter is increased to $b = 0.06$, phase space becomes more chaotic so greater diffusion is possible and the momentum profile develops greatly pronounced shoulders (blue line). The middle panel of figure 6.6 shows the corresponding phase space portrait. A few stable structures remain between $\rho/\pi \approx \pm 5$ to inhibit diffusion. Beyond this, phase space appears to be globally chaotic and the atoms are free to diffuse until they reach the momentum boundary $\rho_b = 39 \pm 2$. The momentum profile therefore has a narrow central region where diffusion is limited, with much wider wings beyond $\rho \approx 10$ and a sharp cutoff at the position corresponding to the momentum boundary.

The positions of the trapping regions are given by the minima in the cos term in equation 6.6. We expect to find regularly occurring trapping regions at $\rho/\pi = \pm (1.1 \times (2n + 1))$ and indeed it is possible to make out faint white lines marking the edges of momentum trapping regions at $\rho/\pi \approx 1, \pm 5$ in the phase space portrait. At this small value of b, however, the correlations between nearest neighbour kicks is also very small, so the momentum trapping regions have little effect on diffusion.

When $b = 0.24$ (pink profile), the chirped sequence resembles a double kick sequence and the unusual, double-shouldered profile typical of the double-delta kicked rotor is observed. At this value of b, $\epsilon = 0.6$ and the trapping regions are expected at $\rho/\pi = \pm 1.6, 4.9, 8.2, 11.5$. The double-DKR phase space (far right panel in figure 6.6) appears to be made up of three distinct momentum trapping regions.

Whilst it is not possible to make out the first trapping region in the phase
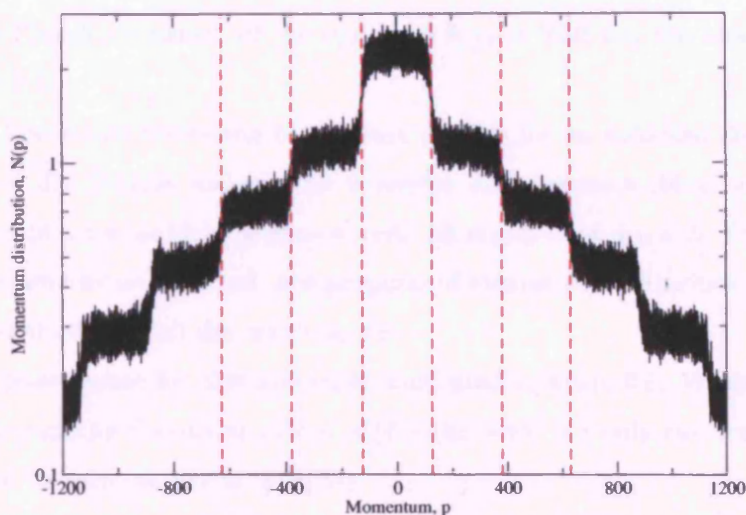
Figure 6.7: Numerical simulation, courtesy of Creffield *et al* (in preparation), showing the distinctive 'staircase' momentum profile of the double-DKR. The red dotted lines indicate momentum trapping regions.

space portrait, its expected position coincides extremely well with the first shoulder of the momentum profile (at $\rho \approx 5$). The second trapping region can be clearly seen in phase space and also agrees very well with the position of the second shoulder of the momentum profile ($\rho \approx 15$). The third trapping region (at $\rho = \pm 26$) is not as clearly marked in the phase space portrait, nor is the cut-off in the momentum profile as clear.

Subsequent numerical analysis has confirmed the appearance of this unusual, double-shouldered 'staircase' profile, see figure 6.7 and [78].

The new correlation terms introduced by a double kicks sequence also have a momentum dependence. Figure 6.8 presents a series of momentum profiles for a double kicks sequence with $b = 0.60, \epsilon = 0.24$ as a function of the initial atomic momentum. We use the moving lattice technique to change the initial momentum and recall that the atomic momentum in the co-moving frame is denoted by the subscript 'L'.

In this series of experiments, the pulse width is $t_p = 470 \pm 23$ ns, the kick period $T = 3.78 \pm 0.01 \mu$s and the separation between kick pairs is equal to two pulse widths $t_s = 2t_p$. The momentum boundary is located at $\rho_b = 51 \pm 2$. The

effective Planck's constant of the system is $\hbar_{eff} = 0.40$ and the kick strength $K = 5 \pm 0.5$.

The first panel shows the momentum profiles for an unkicked distribution (black), a distribution kicked with a regular kick sequence (blue) and atoms subjected to a double kicks sequence (red), all prepared at $\rho_{L0} = 0$. The profiles are all symmetric as expected. For purposes of comparison, we include the single kicks distribution in all the other panels.

The phase space for this system is illustrated in figure 6.9. We expect momentum trapping regions at $\rho/\pi = \pm (4 \times (2n + 1))$ but only two trapping regions can be seen (at $\rho/\pi \approx \pm 10, 30$).

Comparing the momentum profile initially prepared at $\rho_{L0} = 0$ with the phase space diagram, we see that the edge of the first trapping region is in good agreement with the position of the first shoulder of the profile. A second shoulder is not observed because the momentum boundary inhibits diffusion beyond $\rho_b = 51 \pm 2$.

As the initial atomic momentum is increased, momentum asymmetry develops for both single and double-kicked distributions due to presence of the momentum boundary but it is immediately apparent that the double-shouldered 'staircase' profile only appears when the sequence is composed of closely spaced kick pairs.

Consider the momentum profile for $\rho_{L0} = 46$. In this case, the momentum boundary is located at $\rho_b = 4 \pm 0.2, -97 \pm 5$ in the laboratory frame. Diffusion is heavily restricted towards positive momenta because of the boundary but two shoulders are clearly defined on the negative momenta side of the atomic distribution. We estimate the positions of trapping regions to be $\rho \approx 10, 40, 85$ (marked in green dotted lines on the diagram), the latter two in good agreement with the phase space diagram ($\rho \approx 31, 94$).

A close examination of the atomic energy and asymmetry for single and double kick sequences shows some unexpected behaviour, figures 6.10 and 6.11. The effective Planck's constant for this data is $\hbar_{eff} = 1$ and the stochasticity parameter $K = 3.4 \pm 0.3$. The pulse width $t_p = 296 \pm 14$ ns, kick period
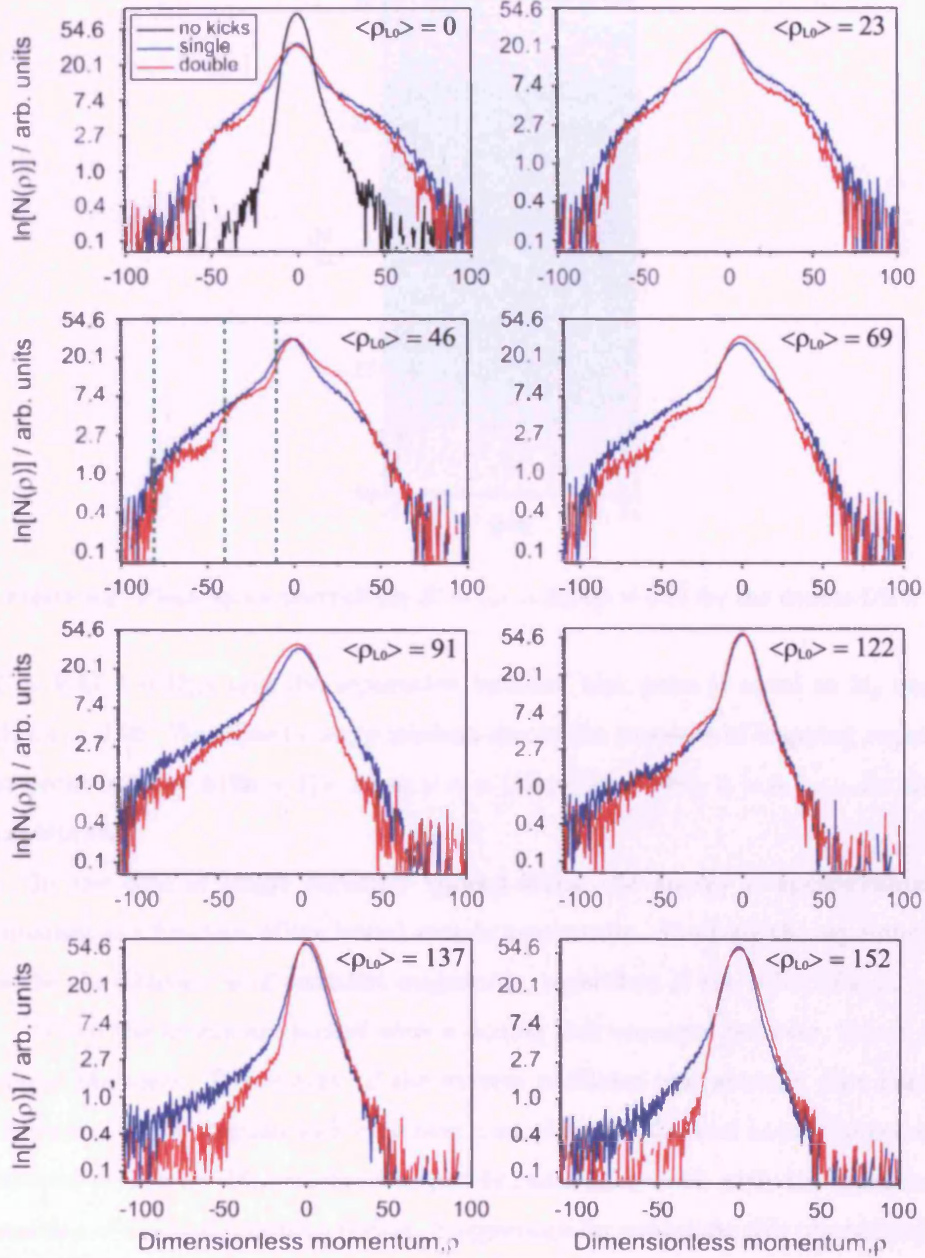
Figure 6.8: Momentum profiles of the double-DKR for various initial atomic momenta $\langle \rho_{L0} \rangle$ (in red). The kick strength is $K = 5$ and $\epsilon = 0.24$. The momentum profiles for the single kicks case for otherwise identical experimental parameters are in blue whilst the unkicked distribution is shown in black. In the $\rho_{L0} = 46$ case, the green dotted lines roughly indicate the position of momentum trapping regions.
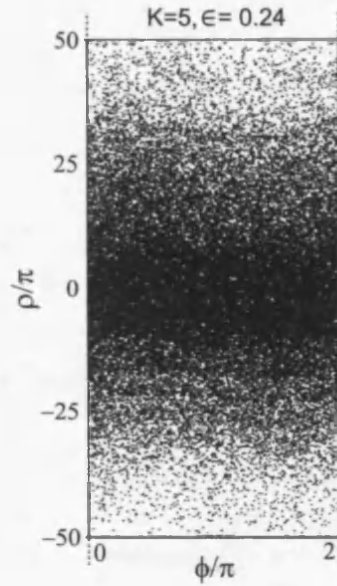
Figure 6.9: Phase space portrait for $K = 5, \epsilon = 0.24(b = 0.6)$ for the double-DKR.

$T = 9.47 \pm 0.02\mu$s and the separation between kick pairs is equal to $2t_p$ such that $\epsilon = 0.06$. We expect energy minima due to the presence of trapping regions to occur at $\rho\epsilon = \pm(2n + 1)\pi$, so at $\rho = \pm(16 \times (2n + 1)\pi)$, $n = 0, 1, ...$ for this experiment.

In the case of single regularly spaced kicks, the energy is approximately constant as a function of the initial atomic momentum. Similarly the asymmetry of the distribution is of constant magnitude, regardless of the value of ρ_{L0}.

When the atoms are kicked with a double kick sequence however, this is no longer the case. The energy of the system oscillates and actually dips below the energy of the regular kick case over a small range of initial atomic momenta centred at $\rho/\pi = 16$, which corresponds remarkably well with the predicted position of the first trapping region. Suggestions for exploiting this phenomenon as a momentum filter for cold atoms have been made [79].

Next we investigate the double delta-kicked rotor as a function of $\epsilon = t_s/T$, by varying the separation between the kicks in each pair. Each correction term acts on a different timescale (the C_1 correction being dominant at small times,
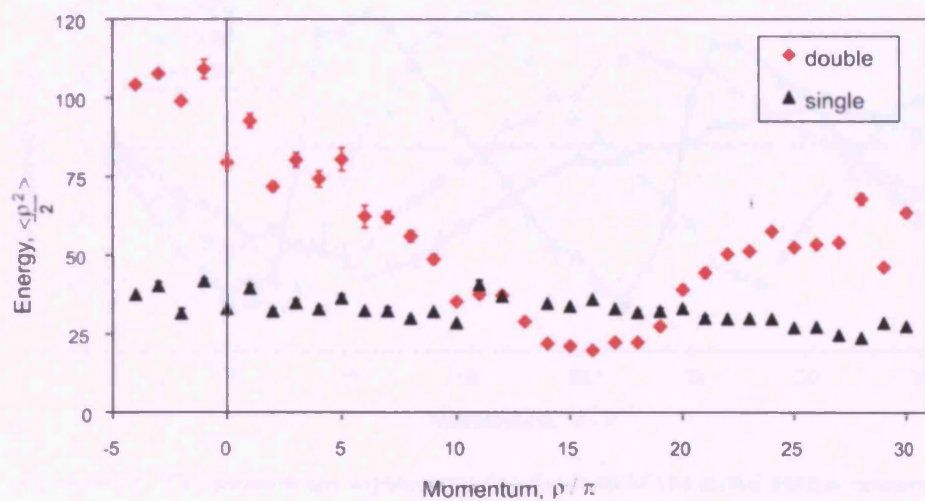
Figure 6.10: The atomic energy as a function of initial atomic momentum for regular and double kicks sequences.
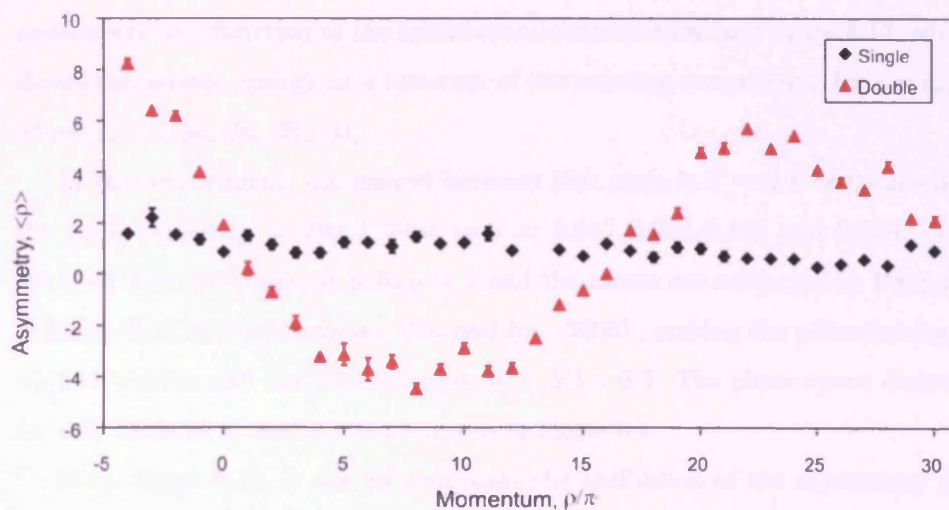
Figure 6.11: The momentum asymmetry as a function of initial atomic momentum for regular and double kicks sequences.
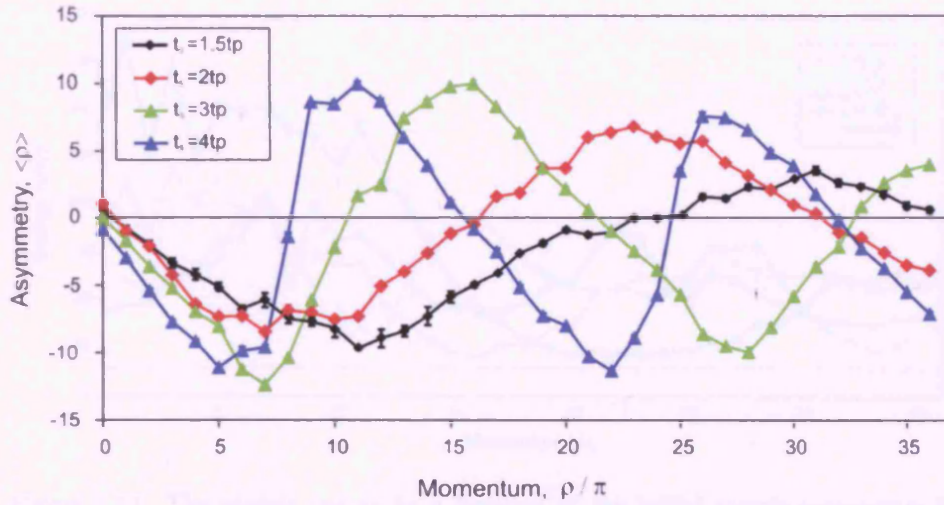
Figure 6.12: The momentum asymmetry as a function of the initial atomic momentum for several values of $\epsilon = 0.047, 0.063, 0.125, 0.156$.

C_{G1} at long times and C_P at intermediate times) but all timescales have a dependence on ϵ. By varying ϵ, therefore, we can observe the effect the new correction terms have on the energy growth of the double-DKR.

The results of this experiment are reported in figure 6.12, which plots the asymmetry as a function of the initial atomic momentum, and figure 6.13, which shows the atomic energy as a function of the starting momentum, for $\epsilon = t_s/T$ where $t_s = 1.5t_p, 2t_p, 3t_p, 4t_p$.

In this experiment, the period between kick pairs is $T = 9.47 \pm 0.02\mu s$ and the pulse width $t_p = 296 \pm 14$ns so $\epsilon = 0.047, 0.063, 0.125$ and 0.156. The effective Planck's constant is $\hbar_{eff} = 1$ and the atoms are subjected to 100 pairs of kicks. The lattice beams are detuned by -2000Γ, making the potential depth $V_0/\hbar = 11$MHz and the kick strength $K = 3.3 \pm 0.3$. The phase space diagram for this value of K and $\epsilon = 0.1$ is given in figure 6.4.

From figure 6.12, it can be seen that the oscillation of the asymmetry becomes more rapid as t_s becomes larger. The oscillation also becomes less sinusoidal as the separation is increased. The differences are due to the different kick-to-kick correlation terms that dominate in each case.
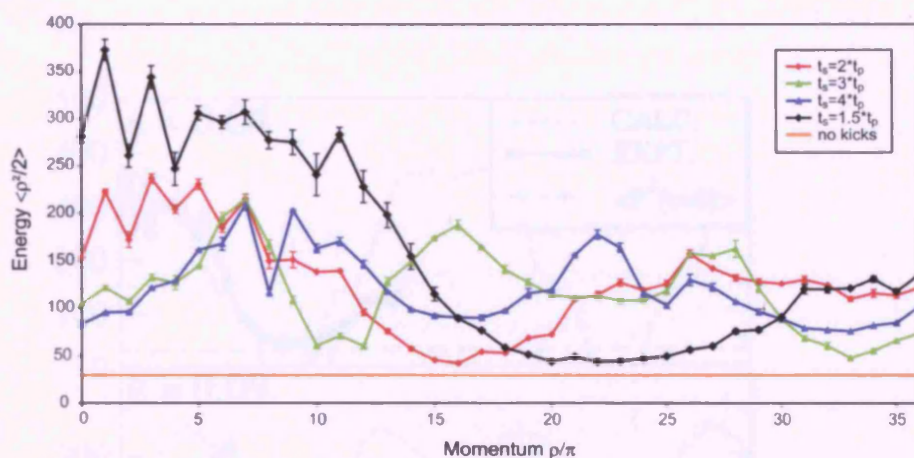
Figure 6.13: The atomic energy as a function of the initial atomic momentum for $\epsilon = 0.047, 0.063, 0.125, 0.156$

The variation in atomic energy as a function of t_s is more carefully investigated in figure 6.14, which plots energy as a function of the initial atomic momentum against the numerical simulations of Jones *et al* [78].

In the topmost panel of figure 6.14, the C_1 correction is the dominant term and the atomic energy is a co-sinusoidal function of momentum. As the separation between the pulses in each kick pair is increased (second panel down), the C_1 and C_{G1} corrections begin to cancel each other out. Accordingly, the atomic energy does not fall to as low a minium value and dips start to appear at the maxima as the C_{G1} correction acts to transform energy maxima into minima. At intermediate timescales, the Poisson correction becomes dominant and clear inverted peaks may be observed (third panel down). At even greater separations, these inverted peaks become much smaller because the C_{G1} correction dominates.

6.3   Summary

This chapter introduced and characterised the double delta-kicked rotor, where the DKR is kicked by a series of closely spaces pairs of kicks or double kicks rather than a regular kick sequence. Initially we showed that the double-DKR
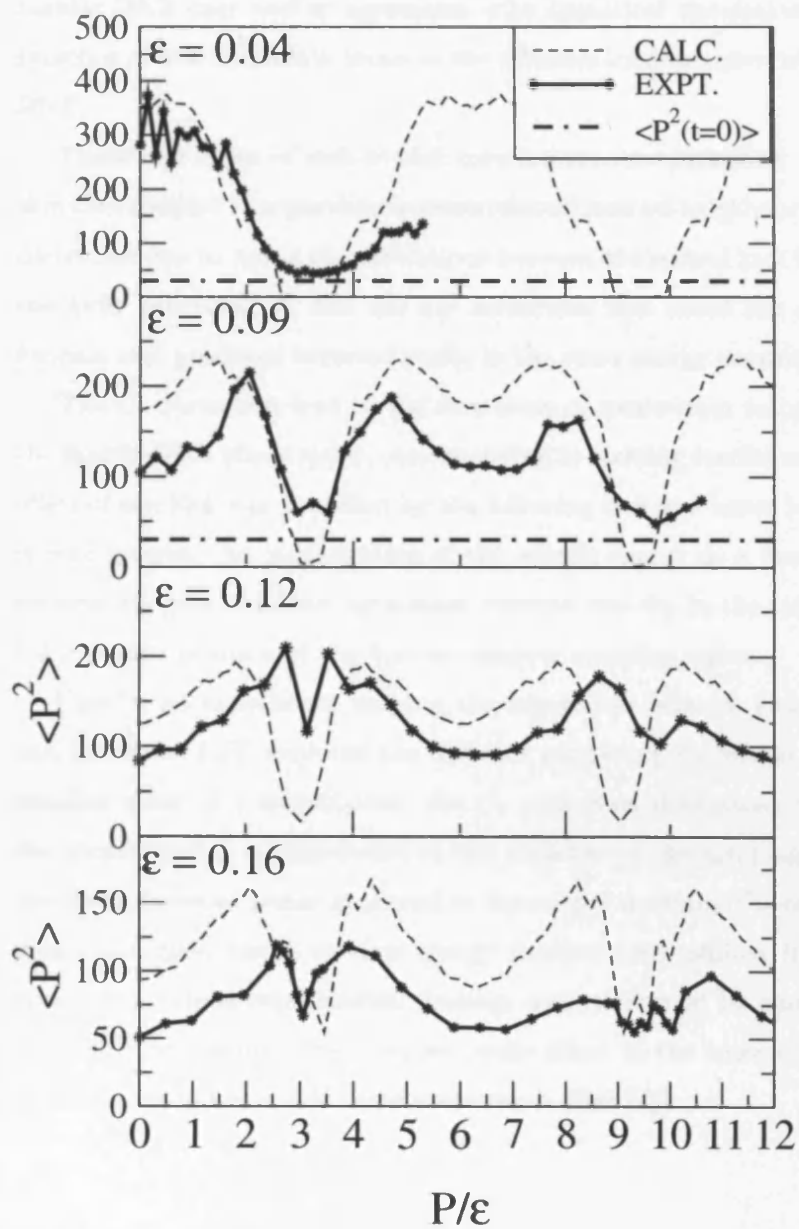
Figure 6.14: A comparison of the experimental data with numerical fits for the atomic energy as a function of the starting momentum. The vertical axis shows the atomic energy $\langle \rho^2 \rangle /2$ and the horizontal axis is dimensionless momentum ($P \equiv \rho$). Thanks to T. Monteiro for the simulations [78].

momentum profile was an unusual 'staircase' shape (quite distinct from the regular DKR case and in agreement with numerical simulations), due to the presence of new correction terms in the diffusion constant governing the double-DKR.

Three new types of kick-to-kick correlations were identified: the C_1 correction that coupled (the previously uncorrelated) nearest neighbour kicks; the C_{G1} correction due to non-zero correlations between the second kick in pair with all the kicks preceding it; and the C_P correction that acted like a Poisson sum formula and produced inverted peaks in the rotor energy maxima.

The C_1 correction lead to the formation of momentum trapping regions in the double-DKR phase space, corresponding to starting conditions for which the effect of one kick was cancelled by the following kick and hence lead to minimal energy growth. An investigation of the atomic energy as a function of initial momentum gave excellent agreement between the dip in the rotor energy and the expected position of the first momentum trapping region.

Finally, an experiment varying the separation between kicks in each pair and hence $\epsilon = t_s/T$ explored the different competing correction terms. At the smallest value of ϵ investigated, the C_1 correction dominated and minima in the atomic energy corresponded to the positions of the trapping regions. As ϵ increased, inverted peaks appeared in the energy maxima (C_P-correction dominant) and then began to turn energy maxima into minima (C_{G1} correction dominant). These experimental findings were confirmed by numerical simulations of excellent fit. The inverted peaks effect in the rotor energy could be exploited for use as a cold atom momentum filter [79].

CHAPTER 7

A Brownian ratchet

A ratchet is a device that produces unidirectional motion from a system under no net bias. In particular, a Brownian ratchet generates directed motion ('a current') by rectifying random fluctuations. There has been much recent interest in studying such systems because it is thought that they may model molecular motors like kinesin, the protein responsible for muscular contraction [81, 82]. This chapter details a method of realising a Brownian ratchet using cold caesium atoms in a 3-dimensional optical potential. A current of atoms is shown to be generated when the temporal symmetry of the system is broken by applying an oscillating force of zero mean to rectify random fluctuations (noise) in the optical lattice.

7.1   Introduction

Brownian motion is named after the botanist Robert Brown who made observations of random motion of pollen grains on water in 1827 and today it is known as the archetype of a random walk. Almost 80 years later, Brownian motion was set in a more mathematical framework by Einstein, Smoluchowski and by Langevin (cited in [83]), who separated the forces acting on a particle suspended in a liquid into two parts: firstly random fluctuations that time-average to zero and secondly a viscous drag force that acts to damp any induced particle mo-

tion. The amplitude of the fluctuations depends on the viscosity of the medium and also its temperature so is often termed thermal noise.

Ratchets driven by thermal noise are called Brownian motors [71]. The basic concept behind ratchets is easily explained using a Smoluchowski-Feynman ratchet, shown in figure 7.1 and realised on a molecular scale by Kelly *et al* in [84]. It consists of a set of paddles attached to a saw-toothed ratchet and pawl system by a frictionless axle. A weight is fixed near the middle of the axle to measure any work done by the paddles and the whole system is surrounded by a gas at thermal equilibrium. In the absence of a temperature gradient, the effect of thermal noise is isotropic across the system.

At first glance, one expects the weight to be lifted by the combined action of the gas molecules colliding with the paddles and the pawl that permits the ratchet to turn in only one direction. This, however, is in essence a perpetual motion machine and so a ratchet where directed motion results from unbiased fluctuations violates the second law of thermodynamics. This 'Brillouin's Paradox' was solved by Marian von Smoluchowski and popularised Richard Feynman, who noted that gas collisions could occasionally lift the pawl to allow the ratchet to turn in the opposite direction. The net motion of the ratchet will be nil and the system will not have done any work lifting the weight suspended by the axle. The presence of spatial asymmetry alone, therefore, does not result in directed motion and a temperature gradient or doing work on the system is necessary to realise a ratchet that is permissable by the second law of thermodynamics [85].

Much of the recent interest in ratchets stems from the possibility that molecular motors may employ an action similar to the ratchet effect, in contracting muscles for example. The hydrolysis of certain proteins (like adenosine triphosphate (ATP) or sodium-potassium adenosine triphospate (KTP) [83]) may produce fluctuations of the potential that may be rectified to generate directed motion of other proteins.

Studying the directed flow of particles also has relevance in the area of electronics and nano-electronics. In fact, it may be said that a Brownian motor
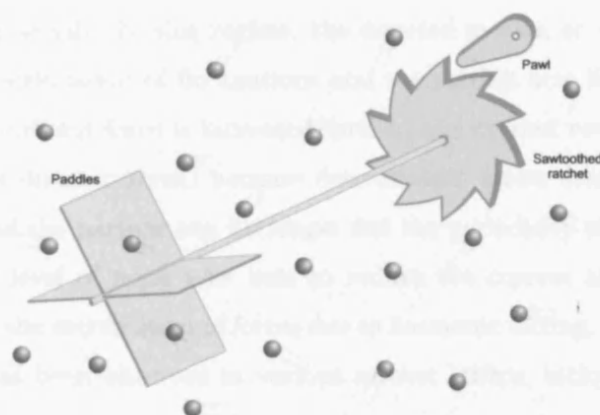
Figure 7.1: A Smoluchowski-Feynman ratchet.

acts (almost) like a electrical rectifier [86]. As electronic circuitry becomes ever more miniaturised, building molecular ratchets may present a way of controlling the current in such a device.

The ratchet effect is an already familiar phenomenon, being used in self-winding wristwatches and ratchet screwdrivers. Gear levers work according to the same principle. The first requirement is some way in which the spatial inversion symmetry of the system might be broken. The Smoluchowski-Feynman ratchet illustrates the second requirement for directed motion, namely that the system is not in thermal equilibrium. Once these two conditions are met, directed motion is possible in a spatially periodic system.

Brownian ratchets can be separated into two basic classes based on the mechanism responsible for directed motion: flashing ratchets, where a stochastic perturbation varies the shape of the potential without affecting its spatial periodicity, and tilting ratchets, wherein unbiased perturbations form an additional driving force on the particles and make the system dynamics spatially asymmetric. The magnitude and direction of the current depends usually on the fine tuning of a system parameter and also on the symmetries that exist in the system.

The typical signature of a Brownian ratchet is current reversal [87, 71, 88, 89]. For a given level of noise, the current increases with the force amplitude

(providing it is small). In this regime, the directed motion or reverse current is due to the rectification of fluctuations and the ratchet acts like a Brownian motor. As the driving force is increased further, the current reverses direction (now called the direct current) because deterministic forces dominate over the fluctuations and the particle can no longer feel the periodicity of the potential. Increasing the level of noise now acts to reduce the current and this regime corresponds to the rectification of forces due to harmonic mixing. This is current reversal and has been observed in various ratchet setups, including nanoscale ratchet pumps.

In the rectification of fluctuations regime, a Brownian ratchet also displays stochastic resonance-like behaviour [90, 91, 92]. This is characterised by a current that initially increases with the amplitude of the fluctuations until an optimum is reached, then decreases as the noise level in increased further and confirms that the system acts like a fluctuations rectifier.

7.2 Types of ratchet

Ratchets are categorised according to the amount of noise and dissipation present and further subdivided by the mechanism responsible for generating the particle current. Brownian ratchets are driven by thermal noise. Replacing random noise with deterministic chaos led to the discovery of noise-free dissipative ratchets, while ratchets with no friction terms form clean Hamiltonian ratchets wherein the particle current is generated by chaotic dynamics alone. Brownian ratchets remain the most widely studied ratchet type, due to their possible applications in biology.

There are two main types of Brownian ratchet that can be realised: those that bias Brownian motion by fluctuating the potential and those that do so using a fluctuating force that time-averages to zero. In the first type, called *flashing* or pulsating ratchets, a particle current is produced by intermittently pulsing (or flashing) an asymmetric potential [88, 91]. This is schematically represented in figure 7.2.

(i) Potential On

(ii) Potential Off

(iii) Potential On

Current
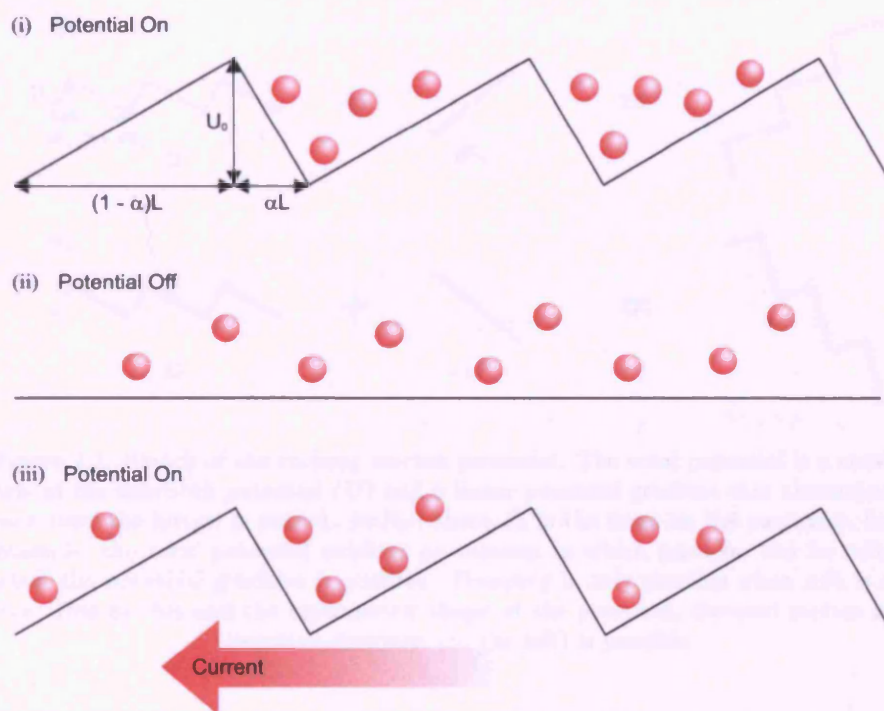
Figure 7.2: Diagrammatical representation of a flashing ratchet. (i) Particles are initially localised at the minima of the ratchet potential. (ii) The potential is switched off for an arbitrary (typically short) time during which the particles are free to diffuse symmetrically in space (iii) The potential is switched back on and the particles retrapped. More particles are trapped near the steep edge of the potential because of its asymmetric shape, which shifts the centre of mass of the particle distribution and so leads to directed motion.

The particles (atoms or molecules, for example) are initially localised at the minima of a sawtooth potential. The potential is switched off for a short time during which the particles diffuse symmetrically and then pulsed back on. The particles are once again trapped at the minima of the potential but the probability of trapping a particle is greater by the steeper edge of the sawtooth, causing an imbalance in the direction of diffusion. The centre of mass of the particle distribution therefore moves preferentially in a direction defined by the shape of the potential (towards the left in this case). Work is done on the system when the ratchet potential is turned on so this model does not violate the second law.
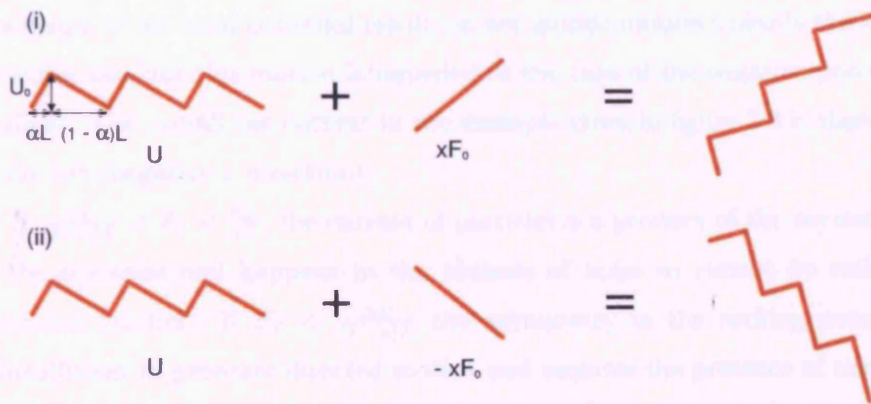
Figure 7.3: Sketch of the rocking ratchet potential. The total potential is a combination of the sawtooth potential (U) and a linear potential gradient that alternates sign each time the lattice is pulsed, $\pm x F_0$ (where F_0 is the force on the particles). In this example, the total potential exhibits no minima in which particles can be collected when the potential gradient is positive. Trapping is only possible when $x F_0$ is negative. Due to this and the asymmetric shape of the potential, directed motion in the negative direction (to the left) is possible.

The second type of Brownian ratchet, called *tilting* or rocking ratchets, use an external driving force to make the system dynamics spatially asymmetric and are further subdivided depending on the properties of the driving force $F(t)$. If $F(t)$ is stochastic these ratchets are known as *fluctuating force* ratchets and when $F(t)$ is a periodic function they fall into the category of *rocking* ratchets. The latter rocking ratchet [93, 94, 95] is the type of ratchet used in our experiments. In our case a spatially symmetric optical potential is subjected to a zero-mean bi-harmonic driving force but the principle of a rocking ratchet can be best illustrated using the following, simpler example. Consider a potential that is the combination of a sawtooth potential and a linear potential gradient $\pm F_0$ that alternates sign each time the potential is pulsed, as illustrated in figure 7.3.

When the total potential is a superposition of the sawtooth and linear potential gradient of the form $U(x) = U_0 + x F_0 > 0$, there are no potential minima present to catch the particles. If the linear potential gradient is of the opposite case, $U(x) = U_0 - x F_0 < 0$, potential minima exist and trapping is possible.

The shape of the total potential results in net atomic motion towards the lower potential side but this motion is impeded in the case of the negative potential gradient. The overall net current in the example given in figure 7.3 is therefore to the left (negative x direction).

If $\frac{U_0}{(1-\alpha)L} < F_0 < \frac{U_0}{\alpha L}$, the current of particles is a product of the asymmetry of the potential and happens in the absence of noise so cannot be called a Brownian ratchet. If $F_0 < \frac{\Delta U}{(1-\alpha)L}$ the asymmetry in the rocking potential is insufficient to generate directed motion and requires the presence of thermal noise to produce a current. In this regime, the system corresponds to a Brownian motor.

A Brownian particle of mass m in a ratchet potential $U(x)$ can be mathematically represented by the following equation of motion:

$$m\ddot{x}(t) + U'\left(x(t)\right) = -\eta\dot{x}(t) + f_0\xi(t) \qquad (7.1)$$

where η is the drag coefficient and $\xi(t)$ is the thermal noise in the system, which is Gaussian white noise that time-averages to zero and satisfies the fluctuation-dissipation relationship $\langle\xi(t)\xi(s)\rangle = 2\eta k_B T\delta(t - s)$, where $f_0 = 2\eta k_B T$ is the noise intensity. The first term on the left hand side of equation 7.1 is the inertial term and $U'\left(x(t)\right) \equiv \frac{d}{dx}U\left(x(t)\right)$ is the (conservative) force resulting from interaction with the periodic potential. Together they describe the deterministic dynamics of the system whilst the terms on the right represent the thermal environment.

When the system exhibits free thermal diffusion, $U'\left(x(t)\right) = 0$ (the particles do not interact with the potential) and the mean square displacement $\langle x^2(t)\rangle = 2\left(\frac{k_B T}{\eta}\right)$ describes a random walk characterised by a diffusion constant $D = k_B T/\eta$.

For all other cases a statistical analysis can be used to derive a system-specific expression for the particle current. The results of such an analysis on a given system shows the particle current falls to zero when the system is in thermal equilibrium, thus satisfying thermodynamics. It also confirms the

results of the Smoluchowski-Feynman ratchet thought experiment. The presence of asymmetry in the system potential alone does not produce directed particle motion. A full derivation of the expression for the particle current in the cases of a 'clean' ($\xi(t) = T = 0$), Hamiltonian ratchet and a flashing ratchet can be found in [50, 71].

As mentioned before, the Brownian motor we have realised may also be considered a rocking ratchet because the directed motion is a product of ac forces in the system that time average to zero. Unlike the system studied above, however, the periodic potential used is spatially symmetric and the mechanism responsible for generating a particle current may be elaborated further by considering the system symmetries and symmetry breaking. A comprehensive review of directed motion in spatially symmetric ratchets can be found in [71].

7.3 Symmetry breaking

In [96], Flach *et al* outline the possibilities of generating a finite particle current by breaking the temporal symmetry of the system alone. For convenience, this analysis of directed diffusion in terms of the symmetries of the system is restricted to a Brownian particle in the regime of weak damping where friction can be neglected ($\eta = 0$) and the system is described by equation 7.2. This regime does not correspond to a Brownian motor but is included as it gives a useful picture of the symmetries involved.

$$m\ddot{x}(t) + f(x) + E(t) = 0 \qquad (7.2)$$

where $f(x) \equiv U'(x)$ and $E(t)$ is a time-dependent driving force.

Let us now consider the reflection and translational symmetries for x and t in the system. If $f(x)$ is antisymmetric after an argument shift $f(x + \chi) = -f(x + \chi)$, the system can be said to have $\hat{f}_a$ symmetry. If $E(t)$ is such that $E(t + \tau) = E(-t + \tau)$, it is said to possess $\hat{E}_s$ symmetry while it has $\hat{E}_{sh}$ symmetry if $E(t)$ is antisymmetric after a coordinate shift equal to any odd integer multiple of $T/2$, $E(t) = -E(t + T/2)$.

This system is invariant under a reflection in x coupled with a shift in t ($\hat{S}_a := x \to -x, t \to t + T/2$) if $f(x)$ has $\hat{f}_a$ symmetry and $E(t)$ possesses $\hat{E}_s$ symmetry. In addition, if $E(t)$ possesses $\hat{E}_s$ symmetry then equation 7.2 is invariant under the transformation $\hat{S}_b := t \to (-t + 2\tau)$.

These transformations $\hat{S}_a$ and $\hat{S}_b$ essentially produce new particle trajectories. For a trajectory $x(t; x_0, p_0), p(t; x_0, p_0)$ with initial coordinates in position and momentum $x_0 = x(t_0; x_0, p_0)$ and $p_0 = p(t_0; x_0, p_0)$ respectively, these are described by the following equations:

$$\hat{S}_a \begin{pmatrix} x(t; x_0, p_0) \\ p(t; x_0, p_0) \end{pmatrix} = \begin{pmatrix} -x(t + T/2; x_0, p_0 + 2\chi) \\ -p(t + T/2; x_0, p_0) \end{pmatrix} \tag{7.3}$$

$$\hat{S}_b \begin{pmatrix} x(t; x_0, p_0) \\ p(t; x_0, p_0) \end{pmatrix} = \begin{pmatrix} x(-t + 2\tau; x_0, p_0) \\ -p(-t + 2\tau; x_0, p_0) \end{pmatrix} \tag{7.4}$$

Note that the new trajectories generated by the symmetry functions carry the opposite sign of p when compared with the initial trajectories. The average particle velocity $\langle \dot{x} \rangle$ is therefore zero, verifying that no net current can be produced when these symmetries are present in the system.

For the specific case of a spatially periodic harmonic potential $U(x) = cos x$ and a bi-harmonic periodic driving force $E(t) = E_1 cos \omega t + E_2 cos(2\omega t + \alpha)$, the symmetry $\hat{S}_a$ is broken if $E_{1,2} \neq 0$ and $\hat{S}_b$ no longer holds if $\alpha \neq 0, n\pi$ or $E_{1,2} \neq 0$. The detailed analysis of [96] shows the current is independent of the starting conditions and its direction only depends on the way in which the symmetries are broken. The average particle velocity produced by the symmetry breaking is proportional to $\frac{E_1^2 E_2}{p_0^4 \omega^3} sin \alpha$. The amplitude of the current can be found by averaging the particle velocity over p_0 and its direction is determined by the sign of $E_2 sin \alpha$. The control parameter for the system is therefore α: the current falls to zero when $\alpha = 0, n\pi$ and it is necessary for α to be static in order to generate a non-zero current.

The current also vanishes as $p_0 \to \infty$, although the symmetries remain broken, when the system approximates the situation of a free particle moving in an external electric field. Their research further adds that no symmetry broken

transport is possible when only one harmonic is present in $f(x)$ and $E(t)$ and that the amplitude of the current may be controlled through the addition of noise.

Experimentally it is impossible to realise a truly non-dissipative ratchet such as the one described above. A small amount of noise always present in the system (since the temperature can never equal zero) but it is possible to approximate a Hamiltonian ratchet by using a large driving force [97] (see also section 7.5). In this regime the particle current is due to harmonic mixing in a non-linear medium. At such large driving forces, the anharmonicity of the potential has an effect on the force on the atoms ($U'(x)$ is no longer $\propto -sinx$) and the non-linear mixing of the two harmonics ω and 2ω produces a current I proportional to the phase difference ϕ between them ($I \propto sin\phi$).

The analysis of the symmetries of the system in the presence of noise and a small driving force is highly complex and the reader is referred to [96] for an in-depth explanation.

7.4   Cold atom realisation of a Brownian motor

To date, Brownian motors have been realised using molecules, nanoelectronics and optical potential systems [84, 82, 98, 86]. We now describe the realisation of a rocking ratchet using cold caesium atoms in a spatially symmetric 3D optical potential subjected to an external zero mean force composed of two harmonics. Fluctuations in the system arise from fluorescence cycles between different optical surfaces, which for small driving forces, are rectified by the applied force. In this regime the system corresponds to a Brownian motor.

A single lattice beam, say in the z direction, is phase modulated to produce a variation in the electric field of the lattice that provides the driving force required for directed motion. This time-dependent phase modulation is composed of two harmonics $\alpha(t) = \alpha_0[Acos\omega t + \frac{B}{4}cos(2\omega t - \phi)]$ (where A, B are both constants) and alters the electric field to include an α-dependence:

$$E_0[\hat{\epsilon}_x e^{i(k_L z - \omega_L t)} - \hat{\epsilon}_x e^{i(-k_L z - \omega_L t - \alpha(t))}] \tag{7.5}$$

where E_0 is the real amplitude of the electric field and k_L, ω_L are the lattice wavevector and frequency respectively.

This is equivalent to accelerating the optical potential by $\lambda \ddot{\alpha}(t)/2$ in the laboratory frame of reference. Dynamics in the reference frame of the moving potential $U(2kz - \alpha(t))$ are given by the co-ordinate transformation $z' = z - \alpha(t)/2k_L$, and the acceleration $a = \ddot{\alpha}(t)$ is equivalent to the atoms experiencing an inertial force:

$$F = Ma = \frac{M}{2k} \ddot{\alpha}(t) \tag{7.6}$$

$$F = \frac{M\omega^2 \alpha_0}{2k_L} \left(A\cos\omega t + B\cos(2\omega t - \phi) \right) \tag{7.7}$$

The periodic external force is therefore a combination of two harmonics of frequencies ω and 2ω with a phase difference ϕ between them, as desired for this realisation of a rocking ratchet. The relationship between the constants A and B as a function of centre of mass velocity was investigated in [97] and found to give a maximum current when $A = B$. Following this work, the constants A and B are set at unity in these experiments. The fundamental frequency ω is chosen to be roughly equal to the vibrational frequency of the lattice Ω such that the results obtained are in the regime of a non-adiabatic driving force.

7.4.1 The Umbrella lattice

Ratcheting occurs only in one dimension (z direction) but a 3D potential is necessary for confinement in the other two directions to increase the interaction time and allow observation of the ratchet effect.

There are many beam configurations that produce 3D lattices (see, for example, [99] for a review) and the topography of the lattice depends on the relative orientation and polarisations of the beams. We employ an 'Umbrella-like lattice' beam configuration that consists of the interference pattern between four laser

beams and forms a lattice with sites of pure circular polarisation (which gives long confinement times, hence optimum cooling, for atoms at the bottom of the wells).

This choice of configuration was also motivated by being able to easily integrate the necessary extra optics into the existing experimental setup. There is space for the beams to be positioned in this way and it also allows independent control over the beam in the z direction without significant modification of the control program. The umbrella lattice is discussed in greater detail in the next section.

The 3D potential is formed by the interference pattern of four laser beams in the 'umbrella-like configuration, figure 7.4. A 150 mW diode laser (the 'lattice' laser) is typically detuned by -10Γ from the Cs D2 line (recall that $\Gamma = 5.22$ MHz). A combination of beam splitters and halfwave-plates are used to split the output of the lattice laser three times to form the four beams of desired intensity. A comprehensive review of 2D and 3D optical lattices can be found in [99, 14].

Beam 1, the 'ratchet beam', (k_1) propagates in the $x - y$ plane and is linearly polarised in the x-direction, $\hat{\epsilon}_1 = \hat{k}_z$. The other 3 beams (k_{2-4}) lie along the edges of a triangular-based pyramid, at 120^0 to each other. Beams k_{2-4} are linearly polarised perpendicular to the plane of the beam and k_1 $(\hat{\epsilon}_j = \frac{k_j \times \hat{k}_1}{k^2})$ and all subtend $\phi = 30^0$ to k_1.

This choice of ϕ requires the electric field amplitudes to be $E_1 = \varepsilon_0$, $E_{2,3} = \varepsilon_0\sqrt{3 + cos^2\theta}/6cos\theta = \varepsilon_0\sqrt{5}/6$, $E_4 = \varepsilon_0/3$ to result in the desired spatially symmetric potential with minima of pure circular $(\sigma^+$ or $\sigma^-)$ polarisation.

For atoms with a $F_g = F \to F_e = F + 1$ transition, there exist $2F + 1$ sub-levels and, as mentioned in Chapter 2, optical pumping between different ground state sub-levels continues to occur after the atoms have localised in the potential wells of the lattice. The Sisyphus cooling phase ends when the atoms have lost enough kinetic energy to become trapped in the lattice sites but they continue to oscillate at the bottom of the wells. Whilst a transition into another sub-level is highly unlikely at the very centre of a well, the atoms
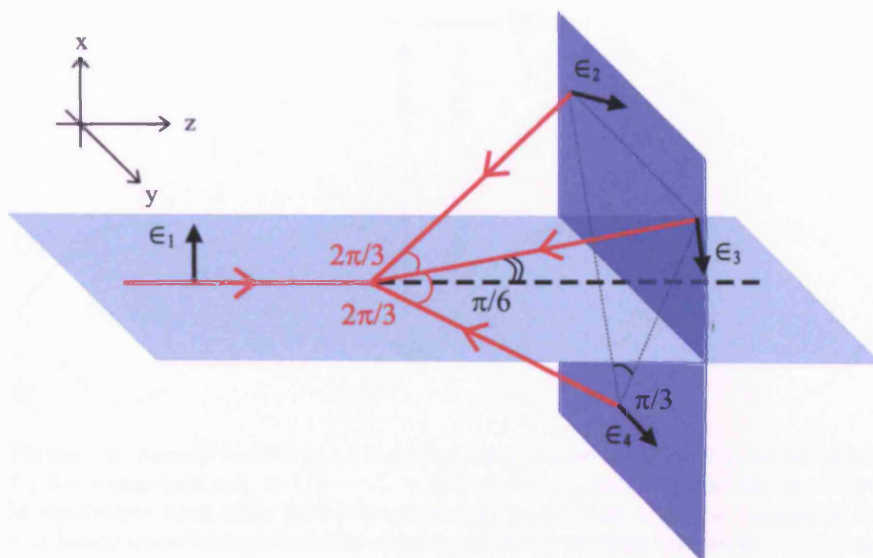
Figure 7.4: A 3-dimensional optical lattice in the 'umbrella-like' configuration. The beam polarisations are shown by thick black arrows.

can experience a non-zero probability of a transition into another sub-level (via an excited state) as soon as they shift off-centre. Transitions between different potential surfaces are random since optical pumping is a stochastic process, so introduces a randomly fluctuating force to the system.

Optical pumping between different potential surfaces also allows atoms that retain enough kinetic energy to move between neighbouring potential wells. An atom pumped into an excited state $|e\rangle$ can decay to a different ground state sub-level and become localised in an adjoining lattice site as illustrated in figure 7.5. The atoms may move between adjacent sites with equal probability so the motion can be characterised by a random walk with a step size equal to one lattice period.

The optical pumping rate is quantified by $\Gamma_s = U_0/\Delta$, wherein the potential depth U_0 is calculated using the measured vibrational frequency and the constant of proportionality is set at unity, and is given in measured scattering units (MSU) throughout this Chapter, which are equivalent to events per second (or Hz). The hitherto neglected geometrical factor can be calculated by performing
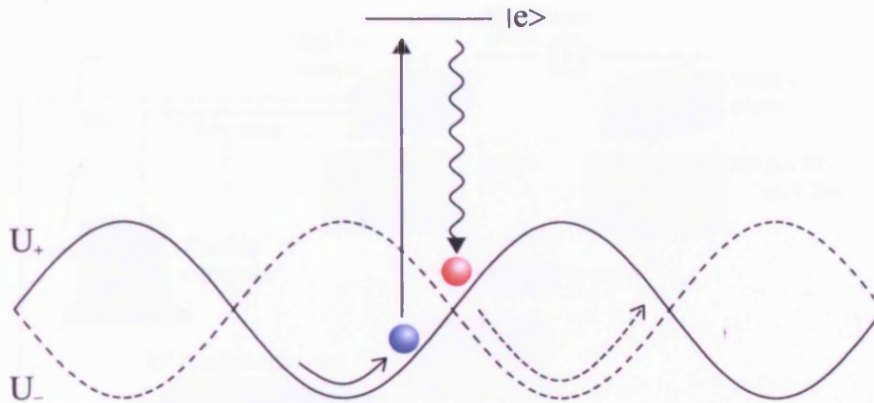
Figure 7.5: Atomic motion in a 1D optical lattice, shown here for two potential surfaces $U_\pm$ for atoms with a $J_g = 1/2 \rightarrow J_e = 3/2$ transition. Although the atoms are localised in the lattice sites, they have enough energy to oscillate near the bottom of the well and hence a non-zero probability of being optically pumped into an excited state. This may be followed by decay into a different potential surface thereby moving the atom to an adjacent potential well.

Bragg scattering experiments [100].

The mechanism responsible for fluctuations in the ratchet system here described is optical pumping between different ground state sub-levels in the umbrella lattice, which makes the photon scattering rate Γ' the appropriate quantity to denote noise levels:

$$\Gamma' \propto U_0/\Delta \qquad (7.8)$$

where U_0 is the depth of a lattice potential well, Δ is the lattice laser detuning from resonance and the constant of proportionality is a numerical factor specific to the geometry of the lattice.

The scattering rate is varied by changing the laser intensity I and detuning simultaneously, thereby keeping the potential depth $U_0 \propto I/\Delta$ the same for all experiments. Changes in the detuning are compensated for by changing the beam intensity via the rf level to the lattice AOMs whilst monitoring the vibrational frequency of the lattice using probe transmission spectroscopy (see section 7.4.3).
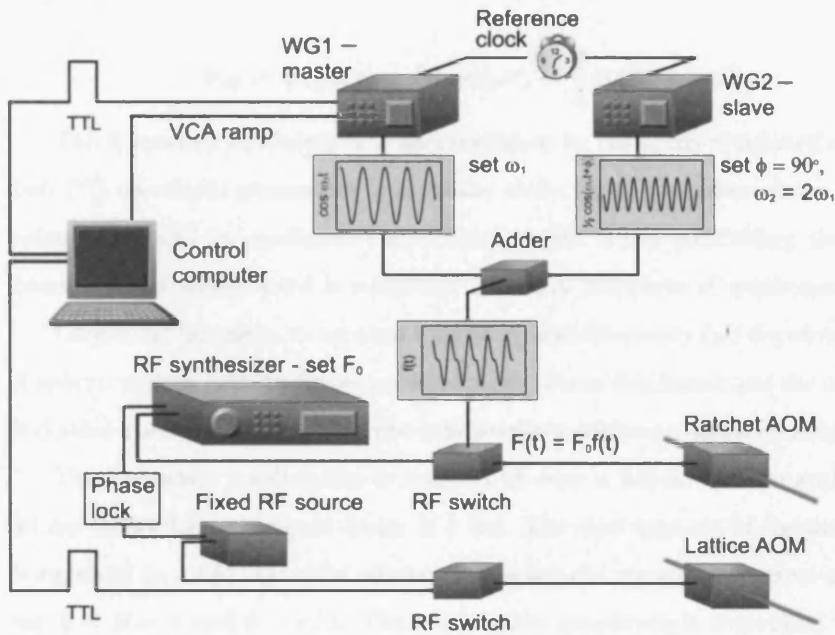
Figure 7.6: Pictorial representation of the equipment stages involved in the phase modulation of the lattice.

7.4.2 Phase modulating the lattice

The spatial symmetry of the atomic dynamics is broken by introducing an external bi-harmonic driving force $F = F_0[A cos \omega t + B cos(2\omega t - \phi)]$ via a phase modulation of the ratchet beam (beam 1, k_1) using a function $\alpha(t) = \alpha_0[A cos(\omega t) + B/4 cos(2\omega t - \phi)]$. The output of the lattice laser is first split into two components, the ratchet beam and another beam that will later be split into the other three lattice beams. They are both passed through separate acousto-optic modulators, each one controlled by its own rf switch that is triggered by a TTL signal from the experiment control program, before being sent through the vacuum chamber of the magneto-optical trap in the umbrellalike configuration.

Rather than phase modulating the ratchet beam directly, we apply a frequency modulation Φ_M that is linked to the phase modulation by its derivative:

$$\Phi_M = d\alpha/dt = \alpha_0[A sin(\omega t) + \frac{B}{2} sin(2\omega t - \phi)].$$ (7.9)

The frequency modulation is accomplished by using the combined output of two TTi waveform generators in a master-slave setup (they then share the same reference clock) to modulate the rf level to the AOM controlling the ratchet beam. The rf source used is a SMY01 Rohde & Schwartz rf synthesizer.

Care must be taken to account for the master frequency (ω) dependence of ϕ. A macro written into an Excel worksheet calculates this factor and the correction is double-checked by observing the combined waveform on an oscilloscope screen.

The frequency modulation is ramped up over a period of 2 ms and lasts for 30 ms before being ramped down in 2 ms. The slow turn-on of the modulation is required to avoid transient effects. Following the recommendations of [97], we set $A = B = 1$ and $\phi = \pi/2$. The modulation amplitude is controlled via the rf synthesizer. The set-up of the apparatus is pictured in figure 7.6.

The control parameter for this Brownian ratchet, the phase difference ϕ in equation 7.6, is now the phase difference between the two harmonics and is easily adjusted using the waveform generator.

7.4.3 Probe transmission spectroscopy

An atom near the bottom of the potential, where the potential may be assumed to be harmonic, can be treated like a oscillator with a vibrational energy level spectrum $E_n = (n + \frac{1}{2})\hbar\Omega_{vib}$, where Ω_{vib} is the natural frequency of oscillation. The potential depth of the lattice is easily calculated if the vibrational frequency, Ω_{vib}, is known. In this instance, Ω_{vib} is determined by probe transmission spectroscopy [101], where a low intensity probe beam propagated through the lattice can drive stimulated Raman transitions between adjacent vibrational energy levels by either absorbing a photon from or emitting a photon into the pump (i.e. lattice) beam of frequency ω.

In the semiclassical picture, the presence of a weak probe beam of frequency causes a periodic modulation of the potential. When the probe detuning,
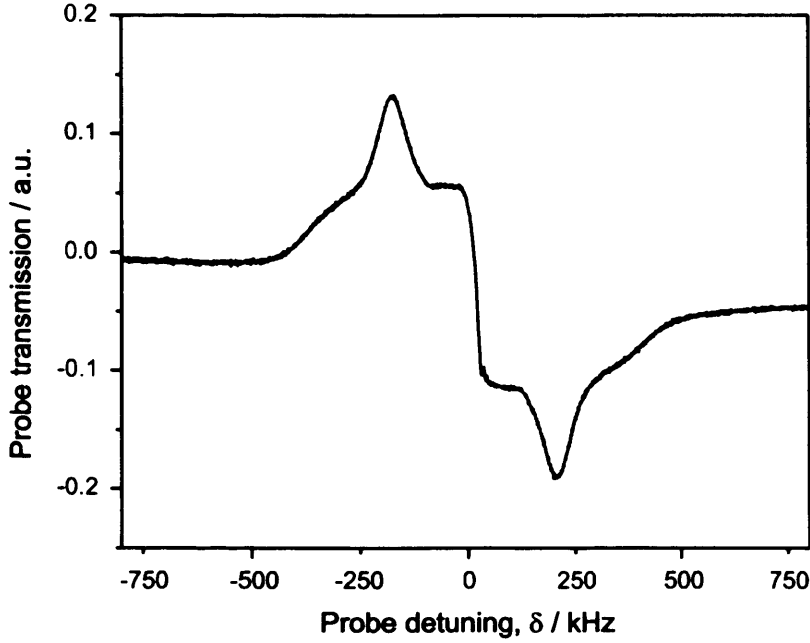
Figure 7.7: A typical probe transmission spectrum.

$\delta_{probe} = \omega_{probe} - \omega_{lattice}$, equals the vibrational energy level spacing, the atom produces a resonant response.

The probe beam intensity is recorded as a function of its detuning from the lattice beam and the vibrational frequency extrapolated from the features in the signal.

Stimulated Raman transitions occur when the probe detuning is an integer m multiple of the frequency spacing between vibrational levels:

$$2\pi \times \delta_{probe} = \pm m\Omega_{vib}. \qquad (7.10)$$

This situation is illustrated in figure 7.8. For an atomic distribution localised in a lattice site, most atoms can be assumed to be in the lowest vibrational state with increasingly smaller fractions present in the higher vibrational levels. When $2\pi \times \delta_{probe} = +m\Omega$, therefore, photons from the probe beam are absorbed (causing a loss in probe beam intensity), whilst absorption of photons from the lattice beam followed by stimulated emission into the probe beam occurs when

Figure 7.8: Stimulated Raman transitions between two vibrational levels in the lattice. The size of the green circles indicate the relative population in each level.

$2\pi \times \delta_{probe} = -m\Omega$ (probe gain).

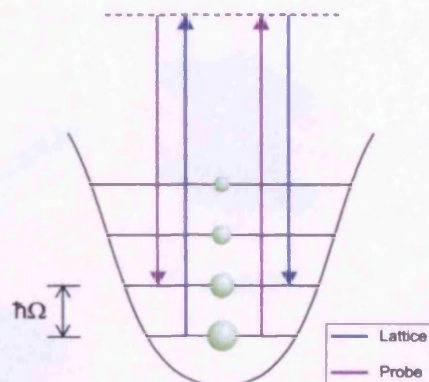A typical spectrum is shown in figure 7.7. In our setup, a linearly polarised probe beam propagates through the MOT vacuum cell at a small angle to the ratchet beam but in the same plane $\hat{k}_z$. The frequency of the probe beam (ω_{probe}) is detuned from the lattice beams ($\omega_{lattice}$) by an amount $\delta_{probe} = \omega_{probe} - \omega_{lattice}$ and swept across a range, typically $\delta = \pm(600 - 1000)$ kHz, in 10 ms.

The sharp feature around $\delta = 0$ is a Rayleigh resonance, due to scattering from the moving interference pattern formed by the probe and lattice beams. The frequency separation between the peak and dip of the probe transmission signal (the Raman resonance) is then used to calculate the vibrational frequency and hence the potential depth of the lattice.

7.4.4 The experimental cycle

A typical experimental cycle, pictorially represented in figure 7.9, begins by cooling and trapping the atoms in the MOT for around 2 seconds before switching off the trap's magnetic field coils, detuning the trap beams further and cooling the atoms for a further 30 ms in an optical molasses. The trap/molasses beams are switched off and the atoms are loaded into the 3D potential for the ratcheting phase. The modulation stage lasts for 30 ms but is slowly ramped up and
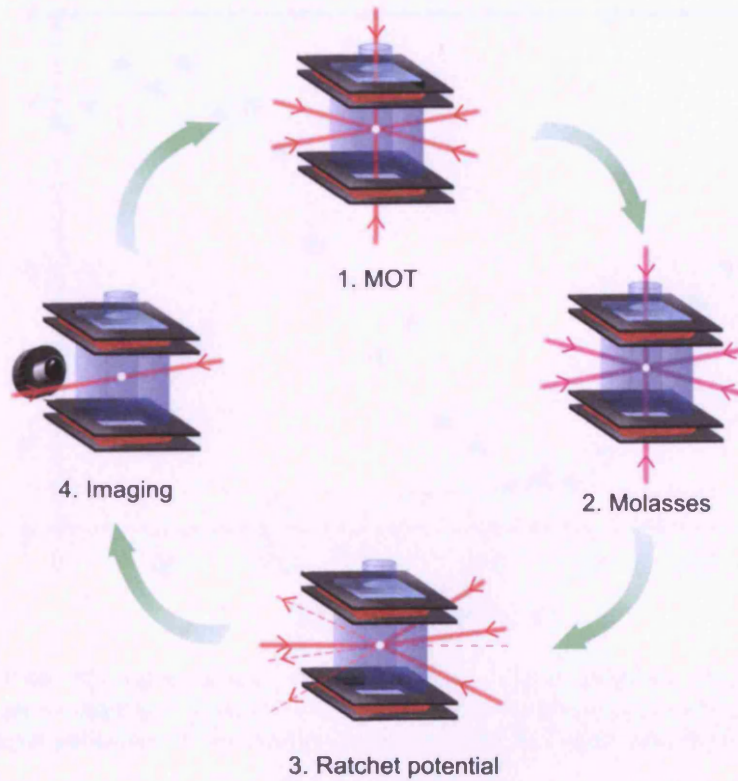
Figure 7.9: Pictorial representation of our experimental cycle, which lasts around 3 seconds.

down over a period of 2 ms to avoid any transient effects.

Finally the motion of the atomic distribution is observed by briefly illuminating the atoms with near resonant light and imaging the scattered light using a cooled CCD camera (as described in Chapter 2). Each data point is an average of five frames and the centre of mass (CM) velocity of the atomic distribution along the z direction can be calculated using the first moment of the atomic distribution. Results of the CM velocity as a function of differing levels of noise are presented in section 7.5.
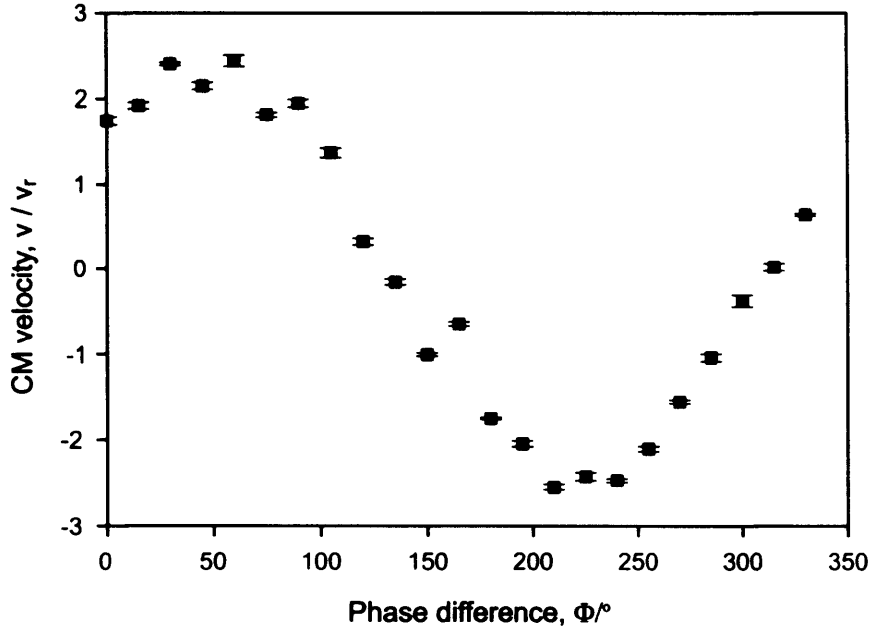
Figure 7.10: The centre of mass velocity, in units of recoil velocities, as a function of ϕ, the phase difference between the two harmonics (frequencies ω and 2ω), which is the control parameter of the system for determining the magnitude of the current at a given scattering rate.

7.5 Results

The first investigation of this Brownian ratchet confirms directed diffusion is possible in this ratchet system. Figure 7.10 presents results of the centre of mass velocity as a function of the control parameter ϕ which verifies the presence of a current in the system. The lattice vibrational frequency is 160 ± 10 kHz and the measured scattering rate $\Gamma_s = 540 \pm 50$ Hz. The results also show the expected oscillatory behaviour with ϕ and hence that it is indeed the control parameter for the Brownian ratchet system at a given scattering rate. We notice that $\phi = \pi/2$ corresponds to the point at which the temporal symmetry of the system is maximally broken (hence maximum current).

We now fix $\phi = \pi/2$ and investigate the centre of mass (CM) velocity as a function of the driving force for several different scattering rates. Because this model system is relatively unexplored, and the physical reason for the rectifica-
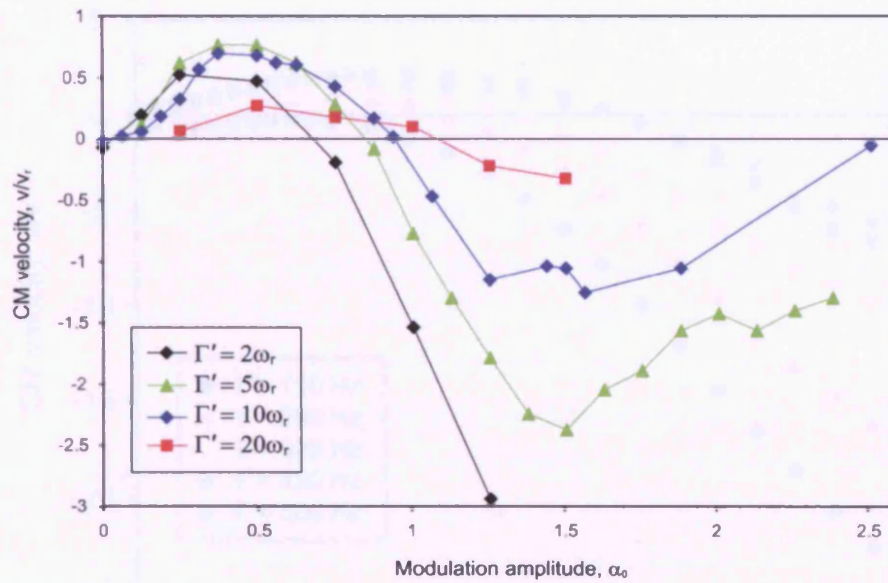
Figure 7.11: Results of a Monte Carlo simulation showing the current reversal behaviour expected in our Brownian ratchet.

tion of fluctuations is not yet known for the case of optical pumping between different potential surfaces, figure 7.11 shows the results of a Monte Carlo simulation of this system (with the exception that the simulation considers a 1D lattice) from Jones *et al* [102]. The numerical simulation demonstrates a non-zero current can be expected from that system and displays the current reversal behaviour characteristic of a Brownian lattice. At small α_0, the fluctuations are rectified and a reverse current is observed. This falls to zero when harmonic mixing begins to dominate the system dynamics. As the modulation amplitude is increased further in the rectification of forces regime, the noise becomes a nuisance and the influence of the periodicity of the potential on the atomic dynamics is reduced so the current approaches zero once more

The experimental results are presented in figure 7.12. The data set has been smoothed by five-point adjacent averaging, which has unfortunately left a small vertical offset to the data. This offset is positive or negative depending on the scattering rate. The plots of the CM velocity in units of the recoil velocity as a function of the modulation amplitude are in very good agreement
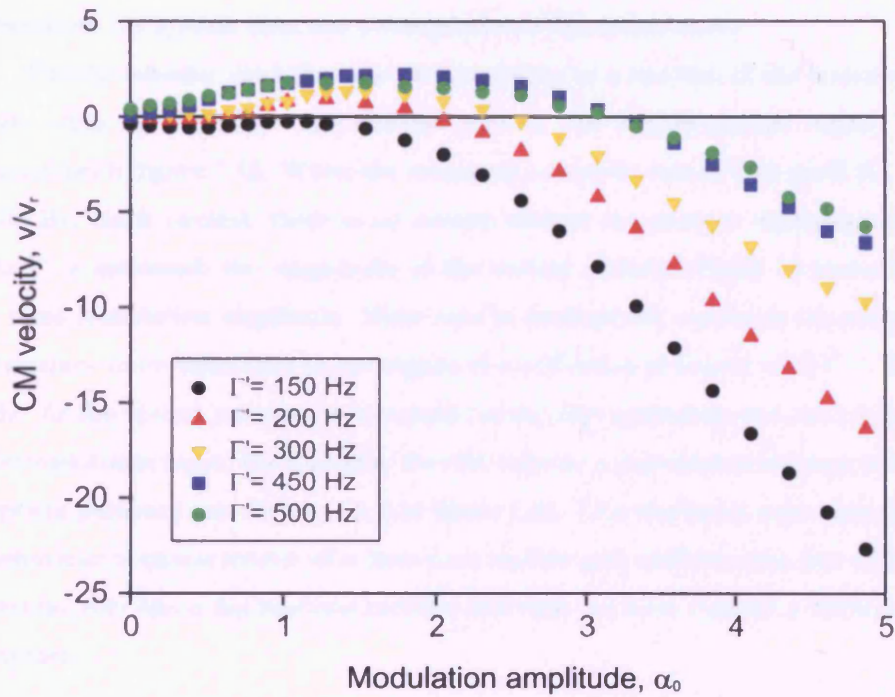
Figure 7.12: Experimental results showing the current reversal behaviour in a Brownian ratchet for several different measured scattering rates, $\Gamma' = 150, 200, 300, 450, 500$ Hz. The centre of mass velocity is given in units of the recoil velocity.

with the theory and the numerical simulation. For a fixed scattering rate, the reverse current increases with the amplitude of the force for small α_0. As α_0 is increased further, the current decreases and reverses direction (becoming a direct current) as the rectification of forces dominates the rectification of fluctuations. The reduction in the magnitude of the direct current, seen in the numerical simulation, is not present in the experimental data because any further increase in α_0 is limited by the available range on the rf synthesizer.

The rectification of forces results from the anharmonicity of the potential at large driving forces. In a non-linear medium, the mechanism responsible is harmonic mixing. The non-linear medium here is the anharmonic potential and the two harmonics produce a force proportional to the phase difference between the two frequencies. This rectified force is $\bar{F} \propto sin\phi$ and fluctuations in the system no longer contribute to the generation of a current. In this regime,

therefore, the system does not correspond to a Brownian motor.

Finally consider the behaviour of this system as a function of the scattering rate when α_0 is small. The relevant section, the reverse current regime, is expanded in figure 7.13. When the measured scattering rate is very small ($\Gamma_s = 150$ Hz, black circles), there is no reverse current (no positive displacement). As Γ' is increased, the magnitude of the reverse current initially increases for a fixed modulation amplitude. Noise acts to increase the current in the system · (contrary to its behaviour in the regime of rectification of forces) until $\Gamma' = 450$ Hz. As the optical pumping is increased beyond this scattering rate, the current decreases once more. For example, the CM velocity is plotted as a function of the optical pumping rate for $\alpha_0 = 1.8$ in figure 7.14. This stochastic resonance-like behaviour is characteristic of a Brownian ratchet and confirms that this model system acts like a fluctuations rectifier and that we have realised a Brownian ratchet.

7.6 Conclusion

In this chapter, we have realised a Brownian ratchet using cold caesium atoms in a 3D umbrella lattice as a model system. The source of noise in the system is optical pumping between the potential surfaces of the different ground state sub-levels of the lattice and it is quantified by the optical pumping rate Γ'. The experimental results show the behaviour predicted both by theory and by numerical simulations. Current reversal and stochastic resonance-like behaviour is evident, confirming that this system corresponds to the realisation of a Brownian motor in the regime of small driving forces. The added importance of this realisation in the type of system used. All the experimental parameters, including the scattering rate, may be controlled by adjusting the parameters of the laser fields involved. Unlike solid state systems there are no defects in the crystal structure and optical lattices are a far more tunable system than an optical tweezers set-up. There is much potential for a system such as this for use in ratchet experiments, including forming a testing ground for deterministic

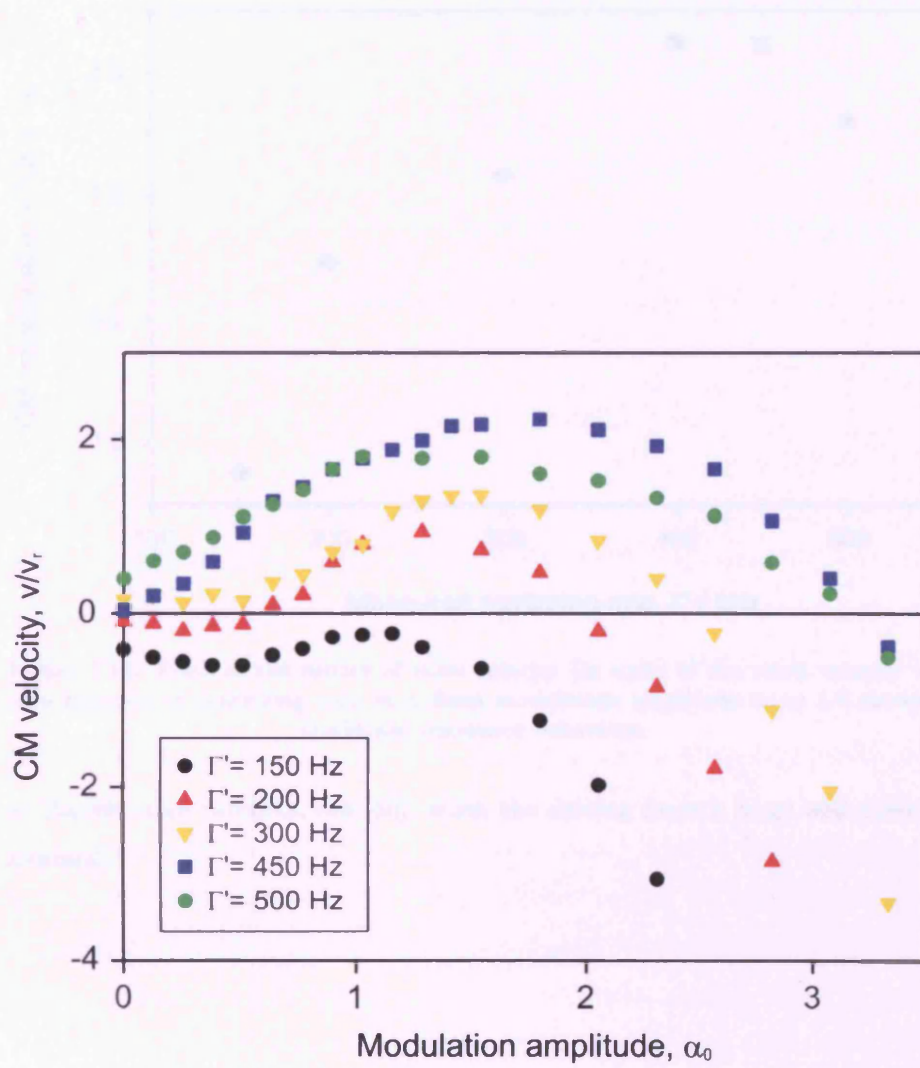Figure 7.13: Expanded section from figure 7.12, showing the regime of the rectification of fluctuations.
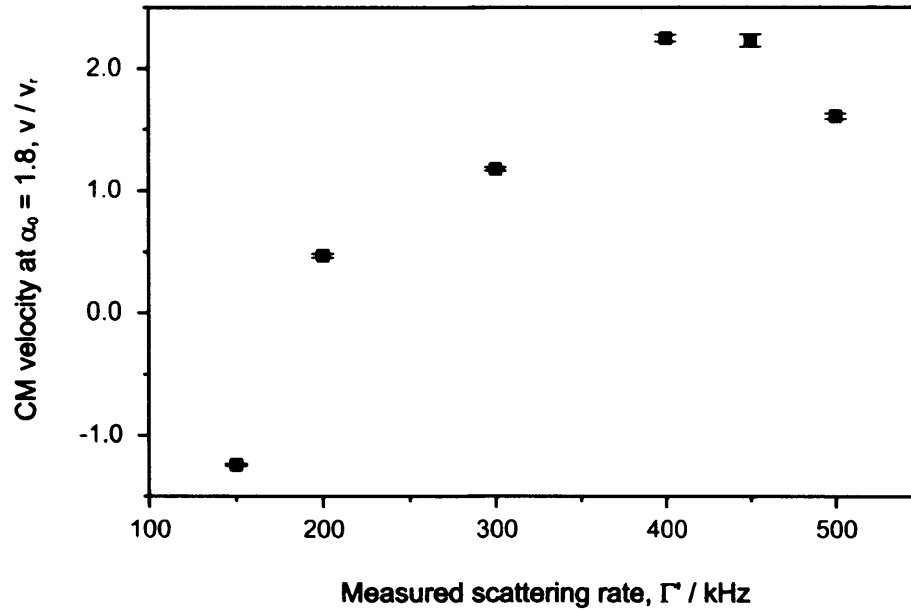
Figure 7.14: Plots of the centre of mass velocity (in units of the recoil velocity v_r) as a function of scattering rate at a fixed modulation amplitude $\alpha_0 = 1.8$ showing stochastic resonance behaviour.

or Hamiltonian ratchets, see [50], when the driving force is large and noise is minimal.

CHAPTER 8

Conclusion

This thesis has detailed several ways in which directed atomic transport can be realised using laser-cooled caesium atoms in optical lattices, roughly subdivided into methods of generating transport in dissipative regimes wherein a Brownian motor may be realised or those in non-dissipative regimes, when the dynamics of the system are deterministic and transport was generated using several different methods.

In the first part of this thesis (Chapters 3-6), we demonstrated how directed motion may be generated in a non-dissipative regime by modelling a delta-kicked rotor (DKR) using cold Cs atoms in a pulsed, far-detuned optical lattice. The DKR is a freely moving planar rotor subjected to instantaneous impulses, which are not possible to realise experimentally. The square-pulse approximation to the delta-kicks introduced a sinc-squared momentum dependence to the diffusion constant $D(K, \rho)$. The minima of $D(K, \rho)$ are called the momentum boundary, a barrier to atomic diffusion that, when used in conjunction with the moving lattice technique, could be exploited to produce asymmetric diffusion. The utility of the moving lattice technique was also demonstrated by the exploration of mixed phase space in Chapter 4.

In Chapter 5, the temporal symmetry of the DKR was broken by pulsing the potential according to a bi-periodic kick sequence $T(1-b) : T(1-b)$ with a chirp parameter b. This introduced a cosinusoidal momentum- and chirp parameter-

dependence into the kick-to-kick correlation terms in the diffusion constant, specifically the C_2 correction term quantifying correlations between next-but-one kicks. Directed transport was observed when the diffusion constant was made locally asymmetric, with the magnitude and direction of the momentum asymmetry dependent on ρ_0. The growth of the asymmetry was investigated and the expected periodicity of the oscillation of the asymmetry, π/b, was also verified experimentally.

Asymmetric diffusion was also produced as a result of breaking both the spatial and temporal symmetry of the DKR. Temporal symmetry was broken by chirping the kick sequence as before and a linear potential gradient that alternated sign with successive kicks was imposed on the optical potential to break spatial symmetry. The potential gradient A was achieved by chirping the frequency difference between the lattice beams to accelerate the potential and was equivalent to an additional inertial force in the reference frame of the lattice. The modulation of the diffusion constant in this case also depended on the magnitude of A. Results showing the generation of momentum asymmetry, its dependence on A and asymmetric momentum profiles were presented in Chapter 5.

In Chapter 6, we realised a 'double delta-kicked rotor' by using a kick sequence of closely spaced pairs of kicks (a double kicks sequence) that made the higher order correlation terms in the diffusion constant non-negligible. In particular, correlation terms that coupled families of kicks and non-zero correlations between nearest neighbour kicks caused a fast modulation of the diffusion constant that generated a unique, double-shouldered momentum profile. Chapter 7 presented evidence of a new type of Brownian ratchet, realised using the Cs atoms in a near-detuned (hence dissipative) lattice and where the current of atoms was produced from unbiased fluctuations. Unlike ratchet systems investigated to date, the mechanism producing noise in this ratchet was optical pumping between the different ground state sub-levels of the lattice. The atoms were subjected to a zero-mean external force composed of two harmonics with a phase difference ϕ between them, $F = F_0[A\cos\omega t - B\cos(2\omega t - \phi)]$ $(A = B = 1)$,

which produced a current. Results are presented for several different levels of noise. Current reversal, the typical signature of a Brownian ratchet, was observed as was stochastic resonance-like behaviour that confirmed the device acted like a fluctuations rectifier. The physical means by which a current is produced is not well understood in ratchets consisting of more than one potential surface and experiments are underway to bring this mechanism to light.

APPENDIX A

Publications

Our published and soon-to-be published papers are presented in this appendix:

1) P. H. Jones, M. Goonasekera, H. E. Saunders-Singer and D. R. Meacher,
Shifting the boundaries: Pulse-shape effects in the delta-kicked rotor,
Europhys. Lett. **67**, 928 (2004).

2) P. H. Jones, M. Goonasekera, H. E. Saunders-Singer and D. R. Meacher,
Asymmetric diffusion in the delta-kicked rotor with broken time symmetry,
arXiv quant-ph 0309149, accepted into Phys. Rev. A. (2004).

3) M. Goonasekera, P. H. Jones, H. E. Saunders-Singer and D. R. Meacher,
Exploring the mixed phase space of the delta-kicked rotor with a moving lattice,
in preparation (2004).

4) P. H. Jones, M. Goonasekera and F. Renzoni, *Rectifying fluctuations in an optical lattice,* Phys. Rev. Lett. **93**, 073904 (2004).

5) R. Gommers, P. Douglas, S. Bergamini, M. Goonasekera, P. H. Jones and F. Renzoni, *Resonant activation in a nonadiabatically driven optical lattice,* accepted for publication in Physical Review Letters.

Bibliography

[1] Nobelprize.org, http://nobelprize.org/physics/laureates/index.html.

[2] C. S. Adams and E. Riis, *Laser cooling and trapping of neutral atoms*, Prog. Quant. Electr. **21**, 1 (1997).

[3] D. Wineland and H. Dehmelt, *Proposed $10^{14}\Delta\nu < \nu$ laser fluorescence spectroscopy on Tl^+ mono-ion oscillator III*, Bull. Am. Phys. Soc. **20**, 637 (1975).

[4] T. Hänsch and A. Schawlow, *Cooling of gasses by laser radiation*, Opt. Commun. **13**, 68 (1975).

[5] H. J. Metcalf and P. van der Straten, *Laser cooling and trapping of neutral atoms* (Springer-Verlag, Inc., New York, USA, 1999).

[6] C. J. Foot, *Laser cooling and trapping of atoms*, Contemp. Phys. **32**, 369 (1991).

[7] P. D. Lett, R. N. Watts, C. I. Westbrook, W. D. Phillips, P. L. Gould, and H. J. Metcalf, *Observation of atoms laser cooled below the Doppler limit*, Phys. Rev. Lett. **61**, 169 (1988).

[8] J. Dalibard and C. Cohen-Tannoudji, *Laser cooling below the Doppler limit by polarization gradients: Simple theoretical models*, J. Opt. Soc. Am. B **6**, 2023 (1989).

[9] C. Cohen-Tannoudji and W. D. Phillips, *New mechanisms for laser cooling*, Physics Today **43**, 33 (1990).

[10] P. J. Ungar, D. S. Weiss, S. Chu, and E. Riis, *Optical molasses and multi-level atoms: Theory*, J. Opt. Soc. Am. B **6**, 2058 (1989).

[11] D. R. Meacher, *Optical lattices: Crystals bound by light*, Chem. Phys. **39**, 329 (1998).

[12] P. Verkerk, D. R. Meacher, A. B. Coates, J.-Y. Courtois, S. Guibal, B. Lounis, C. Salomon, and G. Grynberg, *Designing optical lattices: An investigation with caesium atoms*, Europhys. Lett. **26**, 171 (1994).

[13] P. S. Jessen and I. H. Deutsch, *Optical Lattices*, Adv. At. Mol. Opt. Phys. **37**, 95 (1996).

[14] C. Mennerat-Robilliard and G. Grynberg, *Cold atoms in dissipative optical lattices*, Phys. Rep. **355**, 335 (2001).

[15] Homer, *The Odyssey, Book XI: The Book of the Dead (Nekuia)* (Penguin Books Inc., Harmondsworth, Middlesex, England, 1959), Vol. 14th edition, (trans. E. V. Rieu).

[16] D. Wineland, W. Itano, J. Bergquist, and J. Bollinger, Technical Report No. 1086, NIST, 1985.

[17] E. L. Raab, M. Prentiss, A. Cable, S. Chu, and D. E. Pritchard, *Trapping of neutral sodium atoms with radiation pressure*, Phys. Rev. Lett. **59**, 2631 (1987).

[18] S. A. Hopkins and A. V. Durrant, *Parameters for polarization gradients in three-dimensional electromagnetic standing waves*, Phys. Rev. B **56**, 4012 (1997).

[19] P. Kohns, P. Buch, W. Supitz, C. Csambal, and W. Ertmer, *On-line measurement of sub-Doppler temperatures in a Rb magneto-optical trap by trap centre oscillations*, Europhys. Lett. **22**, 517 (1993).

[20] C. D. Wallace, T. P. Dinneen, K. Y. N. Tan, A. Kumarakrishnan, P. L. Gould, and J. Javanainen, *Measurements of temperature and spring constant in a magneto-optical trap*, J. Opt. Soc. Am. B **11**, 703 (1994).

[21] C. G. Townsend, N. H. Edwards, C. J. Cooper, K. P. Zetie, C. J. Foot, A. M. Steane, P. Szriftgiser, H. Perrin, and D. J., *Phase space density in the magneto-optical trap*, Phys. Rev. B **52**, 1423 (1995).

[22] C. Monroe, W. Swann, H. Robinson, and C. Wieman, *Very cold trapped atoms in a vapour cell*, Phys. Rev. Lett. **65**, 1571 (1990).

[23] W. Ketterle, K. B. Davis, M. A. Joffe, A. Martin, and D. E. Pritchard, *High densities of cold atoms in a dark spontaneous-force optical trap*, Phys. Rev. Lett. **70**, 2253 (1993).

[24] W. D. Phillips, *Atomic micromanipulation with magnetic surface traps*, Phys. Rev. Lett. **83**, 3398 (1998).

[25] J. J. Arlt, O. Marago, S. Webster, S. Hopkins, and C. J. Foot, *A pyramidal magneto-optical trap as a source of slow atoms*, Opt. Commun. **157**, 303 (1998).

[26] K. B. McAdam, A. Steinbach, and C. Wieman, *A narrow-band tunable diode laser system with grating feedback and a saturated absorption spectrometer for Cs and Rb*, Am. J. Phys. **60**, 1098 (1992).

[27] C. Wieman, G. Flowers, and S. Gilbert, *Inexpensive laser cooling and trapping experiment for undergraduate laboratories*, Am. J. Phys. **63**, 317 (1995).

[28] P. Jones, *Ultra-cold atoms in non-dissipative lattices*, DPhil, University of Oxford, 2001.

[29] J. Gleick, *Chaos* (Cambridge University Press, Cambridge, 1997).

[30] T. S. Monteiro, D. Delande, and J. Connerade, *Have quantum scars been observed?*, Nature **387**, 863 (1998).

[31] S. Sridhar, *Experimental observation of scarred eigenfunctions of chaotic microwave cavities*, Phys. Rev. Lett. **67**, 785 (1991).

[32] A. Mouchet, C. Miniatura, R. Kaiser, B. Grémaud, and D. Delande, *Chaos assisted tunnelling with cold atoms*, Phys. Rev. E **64**, 016221 (2001).

[33] B. V. Chirikov, *A universal instability of many-dimensional oscillator systems*, Phys. Rep. **52**, 263 (1979).

[34] T. Shinbrot, C. Grebogi, J. Wisdom, and J. A. Yorke, *Chaos in a double pendulum*, Am. J. Phys. **60**, 491 (1992).

[35] H. Freidrich and D. Wintgen, *The hydrogen atom in a uniform magnetic field: An example of chaos*, Phys. Rep. **183**, 37 (1989).

[36] G. Casati, B. V. Chirikov, I. Guarneri, and D. L. Shepelyansky, *Relevance of classical chaos in quantum mechanics: The hydrogen atom in a monochromatic field*, Phys. Rep. **154**, 77 (1987).

[37] A. Kudrolli, S. Sridhar, A. Pandey, and R. Ramaswamy, *Signatures of chaos in quantum billiards: Microwave experiments*, Phys. Rev. E **49**, 11 (1993).

[38] K. N. Alekseev, G. P. Berman, D. K. Campbell, E. H. Cannon, and M. C. Cargo, *Dissipative chaos in semiconductor superlattices*, Phys. Rev. B **54**, 10625 (1996).

[39] R. Graham, M. Schlautmann, and P. Zoller, *Dynamical localisation of atomic beam deflection by a modulated standing light wave*, Phys. Rev. B **45**, R19 (1992).

[40] G. Casati, *Quantum chaos*, Chaos **6**, 391 (1996).

[41] E. Eisenberg and N. Schnerb, *Suppression of chaos, quantum resonance and statistics of a non-integrable system*, Phys. Rev. E **49**, 941 (1993).

[42] G. Bowman, *Wavepackets and Bohmian mechanics in the kicked rotor*, Phys. Lett. A **298**, 7 (2002).

[43] T. Bhattacharya, S. Habib, K. Jacobs, and K. Shizume, *δ-function kicked rotor: Momentum diffusion and the quantum-classical boundary*, Phys. Rev. B **65**, 032115 (2002).

[44] F. L. Moore, J. C. Robinson, C. F. Bharucha, B. Sundarum, and M. G. Raizen, *Atom optics realization of the quantum delta-kicked rotor*, Phys. Rev. Lett. **75**, 4598 (1995).

[45] F. L. Moore, J. C. Robinson, C. F. Bharucha, P. E. Williams, and M. G. Raizen, *Observation of dynamical localization in atomic momentum transfer: A new testing ground for quantum chaos*, Phys. Rev. Lett. **73**, 2974 (1994).

[46] S. R. Wilkinson, C. F. Barucha, M. C. Fischer, K. W. Madison, P. R. Morrow, Q. Niu, B. Sundaram, and M. G. Raizen, *Experimental evidence for non-exponential decay in quantum tunnelling*, Nature **387**, 575 (1997).

[47] B. G. Klappauf, W. H. Oskay, D. A. Steck, and M. G. Raizen, *Experimental study of quantum dynamics in a regime of classical anomalous diffusion*, Phys. Rev. Lett. **81**, 4044 (1998).

[48] R. Blumel and W. P. Reinhardt, *Chaos in atomic physics* (Cambridge University Press, Cambridge, 1997).

[49] J. M. Greene, *A method for determining a stochastic transition*, Math. Phys. **20**, 1183 (1979).

[50] N. Hutchings, *Chaotic Hamiltonian ratchets with cold atoms*, Ph.D. thesis, University College London, 2004.

[51] A. B. Rechester, M. N. Rosenbluth, and R. B. White, *Fourier-space paths applied to the calculation of diffusion for the Chirikov-Taylor model*, Phys. Rev. B **23**, 2664 (1981).

[52] M. K. Oberthaler, R. M. Godun, M. B. D'Arcy, G. S. Summy, and K. Burnett, *Observation of quantum accelerator modes*, Phys. Rev. Lett. **83**, 4447 (1999).

[53] M. B. D'Arcy, R. M. Godun, M. K. Oberthaler, D. Cassettari, and G. S. Summy, *Quantum enhancement of momentum diffusion in the delta-kicked rotor*, Phys. Rev. Lett. **87**, 074102 (2001).

[54] W. H. Oskay, D. A. Steck, V. Milner, B. G. Klappauf, and M. G. Raizen, *Ballistic peaks at quantum resonance*, Opt. Commun. **179**, 137 (2000).

[55] S. Brouard and J. Plata, *Quantum δ-kicked rotor: The effect of amplitude noise on the quantum resonances*, J. Phys. A: Math. Gen. **36**, 3745 (2003).

[56] D. A. Steck, V. Milner, W. H. Oskay, and M. G. Raizen, *Quantitative study of amplitude noise effects on dynamical localisation*, Phys. Rev. E **62**, 3461 (2000).

[57] S. Fishman, D. R. Grempel, and R. E. Prange, *Chaos, Quantum Recurrences, and Anderson Localization*, Phys. Rev. Lett. **49**, 509 (1982).

[58] E. J. Galvez, B. E. Sauer, L. Moorman, P. M. Koch, and D. Richards, *Microwave ionization of H atoms: Breakdown of classical dynamics for high frequencies*, Phys. Rev. Lett. **61**, 2011 (1988).

[59] M. R. Isherwood, *Chaotic Hamiltonian ratchets in optical lattices*, Ph.D. thesis, University College London, 2004.

[60] S. Fischmann, *Quantum localisation*, in Lecture notes of the Scottish Summer School, 1994.

[61] B. G. Klappauf, W. H. Oskay, D. A. Steck, and M. G. Raizen, *Observation of noise and dissipation effects on dynamical localisation*, Phys. Rev. Lett. **81**, 1203 (1998).

[62] M. G. Raizen, *Quantum chaos with cold atoms*, Advances in atomic, molecular and optical physics **41**, 43 (1999).

[63] D. L. Shepelyansky, *Localization of quasienergy eigenfunctions in action space*, Phys. Rev. Lett. **56**, 677 (1986).

[64] B. G. Klappauf, W. H. Oskay, D. A. Steck, and M. G. Raizen, *Pushing the boundaries: Pulse shape effects in the delta-kicked rotor*, Physica D **131**, 78 (1999).

[65] S. Q. Shang, B. Sheehy, P. van der Straten, and H. Metcalf, *Velocity-selective magnetic-resonance laser cooling*, Phys. Rev. Lett. **65**, 317 (1990).

[66] S. Q. Shang, B. Sheehy, and H. Metcalf, *Velocity-selective resonances and sub-Doppler laser cooling*, Phys. Rev. Lett. **67**, 1094 (1991).

[67] P. H. Jones, M. Goonasekera, H. E. Saunders-Singer, and D. R. Meacher, *Shifting the boundaries: Pulse-shape effects in the atom-optics kicked rotor*, Europhys. Lett. **67**, 928 (2004).

[68] W. K. Hensinger, H. Haffner, N. R. H. A Browaeys, K. Helmerson, C. McKenzie, G. J. Milburn, W. D. Philips, S. L. Rolston, H. Rubinsztein-Dunlop, and B. Upcroft, *Dynamical tunnelling of ultracold atoms*, Nature **412**, 52 (2001).

[69] T. S. Monteiro, P. A. Dando, N. A. C. Hutchings, and M. R. Isherwood, *Proposal for a chaotic ratchet using cold atoms in optical lattices*, Phys. Rev. Lett. **89**, 194102 (2002).

[70] M. Goonasekera, P. H. Jones, H. E. Saunders-Singer, and D. R. Meacher, *Exploring the mixed phase space of the delta-kicked rotor with a moving optical lattice*, in preparation (unpublished).

[71] P. Reimann, *Brownian motors: Noisy transport far from equilibrium*, Phys. Rep. **361**, 57 (2001).

[72] P. Riemann, M. Grifoni, and P. Hänggi, *Quantum ratchets*, Phys. Rev. Lett. **79**, 10 (1997).

[73] J. Mateos, *Chaotic transport and current reversal in deterministic rathets*, Phys. Rev. Lett. **84**, 258 (2000).

[74] H. Linke, T. E. Humphrey, R. P. Taylor, A. P. Micolich, and R. Newbury, *Chaos in quantum ratchets*, Phys. Scrip. **T90**, 54 (2001).

[75] H. Schanz, M. Otto, R. Ketzmerick, and T. Dittrich, *Classical and quantum Hamiltonian ratchets*, Phys. Rev. Lett. **87**, 070601 (2001).

[76] T. Jonckheere, M. Isherwood, and T. S. Monteiro, *Chaotic filtering of moving atoms in pulsed optical lattices*, Phys. Rev. Lett. **91**, 253003 (2003).

[77] P. H. Jones, M. Goonasekera, H. E. Saunders-Singer, and D. R. Meacher, *Asymmetric diffusion in the delta-kicked rotor with broken time symmetry*, arxiv **quant-ph**, 0309149 (2004).

[78] P. H. Jones, M. Stocklin, G. Hur, and T. Monteiro, *Atoms in double-δ-kicked periodic potentials: Chaos with long-range correlations*, arXiv:physics **0405046**, v2 (2004), accepted for publication in Physical Review Letters.

[79] G. Hur, P. H. Jones, and T. Monteiro, *Chaotic quantum ratchets and filters with cold atoms in optical lattices: Properties of Floquet states*, to be submitted Physical Review A (unpublished).

[80] M. Stocklin, G. Hur, and T. Monteiro, *Classical diffusion in double-δ-kicked particles*, to be submitted Physical Review Letters (unpublished).

[81] K. L. Sebastian, *Molecular ratchets: Verification of the principle of detailed balance and the second law of dynamics*, Phys. Rev. E **61**, 937 (2000).

[82] T. R. Kelly, *Progress towards a rationally designed molecular motor*, ACR **34**, 514 (2001).

[83] R. D. Astumian, *Thermodynamics and kinetics of a Brownian motor*, Science **276**, 917 (1997).

[84] T. R. Kelly, J. P. Sestelo, and I. Tellitu, *New molecular devices: In search of a molecular ratchet*, J. Org. Chem. **36**, 3655 (1998).

[85] R. P. Feynman, R. B. Leighton, and M. Sands, *The Feynman Lectures on Physics*, volume I **Ch. 46**, Addison (2001).

[86] H. Linke, W. Sheng, A. Löfgren, A. Svensson, H. Xu, P. Omling, and P. E. Lindelof, *Electron quantum ratchets*, Microelec. Eng. **47**, 265 (1999).

[87] R. Bartussek, P. Hanggi, and J. G. Kissner, *Periodically rocked thermal ratchets*, Europhys. Lett. **28**, 459 (1994).

[88] P. Riemann, *Current reversal in a white noise driven flashing ratchet*, Phys. Rep. **290**, 149 (1997).

[89] J. Luczka, *Application of statistical mechanics to stochastic transport*, Physica A **274**, 200 (1999).

[90] D. G. Luchinsky, M. J. Greenall, and P. V. E. McClintock, *Resonant rectification of fluctuations in a Brownian ratchet*, Phys. Lett. A **273**, 316 (2000).

[91] V. Berdichevsky and M. Gitterman, *Stochastic resonance and ratchets - new manifestations*, Physica A **249**, 88 (1998).

[92] C. Robillard, D. Lucas, and G. Grynberg, *Modelling a ratchet with cold atoms in an optical lattice*, Appl. Phys. A. **75**, 213 (2002).

[93] D. Dan, M. C. Mahato, and A. M. Jayannavar, *Motion in a rocked ratchet with spatially periodic friction*, Physica A **296**, 375 (2001).

[94] T. Zhao, T. Cao, Y. Zhan, and Y. Zhuo, *Rocking ratchets with stochastic potentials*, Physica A **312**, 109 (2002).

[95] T. E. Humphrey, H. Linke, and R. Newbury, *Pumping heat with quantum ratchets*, Physica E **11**, 281 (2001).

[96] S. Flach, O. Yevtushenko, and Y. Zolotaryuk, *Directed current due to broken time-space symmetry*, Phys. Rev. Lett. **84**, 2358 (2000).

[97] M. Schiavoni, L. Sanchez-Palencia, F. Renzoni, and G. Grynberg, *Phase control of directed diffusion in a symmetric optical lattice*, Phys. Rev. Lett. **90**, 094101 (2003).

[98] C. Mennerat-Robilliard, D. Lucas, S. Guibal, J. Tabosa, C. Jurczak, J. Courtois, and G. Grynberg, *Ratchet for cold rubidium atoms: The asymmetric optical lattice*, Phys. Rev. Lett. **82**, 851 (1998).

[99] K. I. Petsas, A. B. Coates, and G. Grynberg, *Crystallography of optical lattices*, Phys. Rev. B **50**, 5173 (1994).

[100] G. Birkl, M. Gatzke, I. H. Deutsch, S. L. Rolston, and W. D. Phillips, *Bragg scattering from atoms in optical lattices*, Phys. Rev. Lett. **75**, 2823 (1995).

[101] O. Morsch, *Optical lattices for ultra-cold atoms*, DPhil, University of Oxford, 1999.

[102] P. H. Jones, M. Goonasekera, and F. Renzoni, *Rectifying fluctuations in an optical lattice*, Phys. Rev. Lett. **93**, 073904 (2004).